Title
Mapping multiscale relationships in soft semiconductor structure and function with multimodal characterization

Author
Tan, Jenna

Publication Date
2022

Peer reviewed|Thesis/dissertation

Mapping multiscale relationships in soft semiconductor structure and function with multimodal characterization

by

Jenna Adrienne Uy Tan

A dissertation submitted in partial satisfaction of the

requirements for the degree of

Doctor of Philosophy

in

Chemistry

in the

Graduate Division

of the

University of California, Berkeley

Committee in charge:

Professor Naomi Ginsberg, Chair
Professor Eran Rabani
Professor David Attwood

Summer 2022

Mapping multiscale relationships in soft semiconductor structure and function with multimodal characterization

Abstract

Mapping multiscale relationships in soft semiconductor structure and function with multimodal characterization

by

Jenna Adrienne Uy Tan

Doctor of Philosophy in Chemistry

University of California, Berkeley

Professor Naomi Ginsberg, Chair

Emerging semiconductors have begun to rival conventional silicon with breakthroughs in improved performance and novel and affordable processing techniques. As the applications for emerging semiconductors are explored, there is a clear need to understand the hierarchical nature of these materials to fully optimize their functionality. Consistently reproducing the assembly and electronic functionality of organic semiconductors, for example, remains difficult given their propensity for variable molecular packing and morphology due to weak bonding interactions. As another case, metal halide perovskite semiconductors demonstrate intriguing photophysics that may change when confined in nanostructure forms. One technique alone cannot comprehensively interrogate the repercussions of changes in the molecular structure to the microstructure, morphology, and ensuing electronic functionality of a semiconductor. Only a multimodal characterization approach enables an extensive multiscale insight into the structure-function dynamics of semiconducting materials and devices.

Chapter 1 first introduces organic semiconductor properties and device applications. Common thin film processing methods and modification strategies are discussed along with the formation of crystalline microstructures in thin films. Next, a suite of characterization techniques that span multiple length and time scales are shared to inform on how one may strategically combine individual techniques to characterize structure, morphology, and dynamics.

Chapter 2 describes a multimodal imaging study of organic semiconductor, rubrene, thin films. Scanning transmission X-ray microscopy reveals and quantifies the disappearance of orientational discontinuities in a hybrid crystalline microstructure, which is corroborated at higher spatial resolution with 4D-scanning transmission electron microscopy. *In situ* polarized optical microscopy during thermal annealing uncovers Arrhenius behavior for rubrene crystallization and that the finite substrate thermalization rate leads to the formation of the observed hybrid crystalline microstructure. This study emphasizes the role of temperature

in organic semiconductor crystallization, and highlights the challenges and opportunities for thin film design protocols.

Chapter 3 focuses on characterizing the anisotropic behavior of inorganic lead halide perovskite ($CsPbBr_3$) nanowires and nanowire bundles. Stroboscopic scattering interferometric microscopy shows exciton diffusion and trapping in the nanowire bundles. We use transient absorption microscopy to probe the polarization-resolved excited-state dynamics of the nanowire bundles. Coupled with polarization-resolved fluorescence, we determine that the splitting of the band-edge exciton states is driven by the shape anisotropy and a long-range exchange interaction. This study demonstrates the power of optical pump-probe microscopies to resolve charge transport and excited-state dynamics in individual structures.

This dissertation highlights the complexities of characterizing soft semiconductor thin films and nanostructures across multiple length and time scales. Despite the challenges in implementing a multimodal approach, the knowledge acquired about the semiconductors, such as defects in packing, grain boundaries, and charge carrier dynamics, is invaluable for guiding future design principles that incorporate semiconducting materials into novel technology.

To my teachers who fostered a passion for learning and exploration

Contents

List of Figures

List of Tables

Acknowledgments

I had a wonderful and supportive community throughout the PhD journey. Thank you to my advisor, Prof. Naomi Ginsberg, for your constant encouragement and support over the years. Your insights, scientific enthusiasm, and dedication spurred my growth as a scientist. I am thankful for them and for all the opportunities I had during my time with you.

I am immensely grateful for my labmates, the Ginsbergers, and their sunshine throughout my time below ground: Hannah Weaver, Leo Hamerlynck, Christian Tanner, Vivian Wall, Livia Belman-Wells, James Utterback, Rongfeng Yuan, Jonathan Raybin, Mumtaz Gababa, Trevor Roberts, Rebecca Wai, Milan Delor, Namrata Ramesh, Eniko Zsoldos, Hannah Stern, Brendan Folie, Alex-Liebman Peláez, Jonathon Kruppe, Jakhangirkhodja (Jack) Tulyagankhodjaev, and Jina Lee. Thank you for your all-around awesomeness; I learned so much from all of you. A special thanks to Brendan, Alex, Jack, Jonathan, Trevor, Leo, Christian, Jina, and Jonathon for working with me on the rubrene project. Your tremendous efforts and insights made it possible. I am also thankful for Brendan for his patience and mentorship as I started working in lab and for getting us started on the rubrene project.

I worked with many brilliant collaborators over the years who helped broaden my scientific perspective. A big thank you to Jordan Dull, Prof. Barry Rand, Steven Zeltmann, Prof. Andrew Minor, Sven Dönges, Omar Khatib, Prof. Markus Raschke, Dr. Colin Ophus, Dr. Karen Bustillo, Dr. Hendrik Ohldag, Dr. Nobumichi Tamura, Dr. Matthew Marcus, Dr. Chenhui Zhu, Jianmei Huang, Dr. Peter Sercel, Minliang Lai, Dr. John Lyons, Dr. Noam Bernstein, Dr. Alexander Efros, and Prof. Peidong Yang.

Thank you to everyone who supports the Chemistry Department, especially Joel Adlen, Ellen Levitan, Lynn Keithlin, Carl Lamey, Roy Washington, and Jessie Woodcock. Special thanks to Joel for supporting the start of CHEMentor and other student efforts. Thank you also to those who ran the STROBE NSF Center, especially Jessie, Dr. Ellen Keister, Lauren Mason, and Dr. Jorge Nicolas Hernandez Charpak.

My experience at William and Mary changed my life in the best ways possible and led me on this scientific trajectory. Thank you, Prof. William McNamara, Prof. Elizabeth Harbron, Prof. Carey Bagdassarian, Jeffrey Molloy, and Prof. Francis Tanglao-Aguas. An enormous thank you goes to Prof. Kristin Wustholz for introducing me to research, cultivating my scientific curiosity, and for being an incredible mentor.

Many thanks to Dr. Xiaoqing Guo and Dr. Nan Mei for a great research experience at NCTR and for continuing to support me afterward.

I feel incredibly lucky to have met and be surrounded by kind and amazing friends in the department. Thank you, Isabel, Dipti, Valerie, Kaydren, Paul, Collin, Josie, Chin, Zach, Bryan, Laura, and Ashley for your friendships and the cherished memories. Special thanks to friends in the Berkeley community, from undergrad, and home for the love and support.

Last but not least, thank you to my parents and sister who have provided steadfast encouragement and love as I pursue my dreams. Thank you to my partner, John, for being there with me every step of the way.

Chapter 1

Introduction

Semiconductors beyond conventional silicon offer opportunities for new technology and for advancing existing ones, such as flexible or stretchable electronics, thin film transistors, and photovoltaics. Organic semiconductors encompass a vast range of structures, which provides a rich arena for studying fundamental processes like crystallization, excited-state dynamics, and device operations. The first half of the introduction chapter covers organic semiconductor properties, device applications, and thin film processing methods and microstructures. The second half of this chapter discusses characterization approaches that can be combined for multimodal studies to probe the structure-function properties of organic semiconductors.

Semiconductors exhibit intermediate electronic conductivity relative to a conductor and insulator due to the energy band structure. A given energy band contains discrete energy levels with extremely small energy differences [1]. The semiconductor band structure is characterized by a small energy band gap (e.g. less than 2 eV) between the so-called valence and conduction bands, and excitation of sufficient energy promotes a valence electron to the conduction band [1]. The vacancy of the electron in the valence band leaves behind a net positive charge that is treated as a quasi-particle called a hole. The hole and electron have the same charge magnitude but opposite signs, and the electrostatic attraction between the electron and hole can form another type of quasi-particle called an exciton. Together, holes, electrons, and excitons are some of the key charge carriers of interest for their diffusion and mobility properties when quantifying the charge transport properties of a semiconductor. With this brief explanation of a semiconductor, we next delve more closely into concepts specific to organic semiconductors as a preface to Chapter 2. The metal halide perovskite nanostructures of Chapter 3 are introduced within that chapter [2].

1.1 Organic semiconductor properties

Organic semiconductor solids can be formed from either small molecules or polymers, where polymers are distinguished by their chain length. Typically organic semiconductors are composed of conjugated π-systems, and the overlapping of π-orbitals allows for delocalization of

the π electrons across the aligned orbitals, which can optimally achieve long-range charge transport [3]. The molecular packing of an organic semiconductor crystal governs the efficiency of charge transport, and variations in the electronic structure, molecular arrangement, and morphology all contribute to molecular packing [3]. The weak bonding interactions (e.g., van der Waals) found in organic semiconductors, lends themselves to being disrupted more easily than the covalent bonds in inorganic semiconductors, which disrupts the molecular packing and partially explain the challenges of achieving higher charge mobility in organic semiconductors.

At room temperature, the charge mobility most likely results from a hopping transport process [4, 5], where a rate of transfer probability determines the likelihood of a charge carrier (electron or hole) moving to another site [4, 6]. Two significant parameters that affect hopping transport are the electronic coupling between adjacent molecules and reorganization energy, which represents the geometry of the molecules during the charge transfer process [4, 5]. These two factors are highly dependent on the molecular arrangement within an organic semiconductor crystal, which explains why discussion of molecular packing or arrangement is often intertwined with charge transport efficiency. Charge transport is often anisotropic in organic semiconductors and occurs along the $\pi - \pi$ stacking direction between molecules.

1.2 Organic semiconductor devices

Exploration of organic semiconductors applications for existing semiconductor devices includes field-effect transistors (FETs) and photovoltaics as a couple of examples. A typical FET setup from the bottom to the top has a gate, dielectric, semiconductor, and source and drain in contact with opposite ends of the semiconductor. A voltage applied between the gate and source forms an accumulation layer of charge carriers at the semiconductor-dielectric interface. The gate voltage also controls the current that flows between the source and drain to induce or stop current flow, which is why transistors are often used for switching [4]. Some considerations in the fabrication of organic FETs include optimizing the size of the organic semiconductor crystalline domains (e.g., minimizing grain boundaries), finding a suitable substrate, and determining the order of construction of the transistor to minimize damage to the organic semiconductor layer [3]. Charge carrier mobility describes the performance of FETs, and organic FETs have demonstrated comparable mobilities to amorphous silicon-based FETs [4]. Continuing research will improve organic FETs for mass production and increased application, as highlighted by this example of a study demonstrating the growth of a organic semiconductor (triclinic rubrene) directly onto the substrate for a vertical bipolar junction transistor that exhibited improved device performance [7].

Organic photovoltaics (OPVs) offer an opportunity to decrease production costs. The general schematic of a bilayer OPV includes a transparent electrode, two organic light-absorbing layers, and another electrode [8]. One organic semiconductor layer acts as the electron donor and the other as the electron acceptor to facilitate electron and hole transport. The critical steps in OPV performance are the migration of the excitons to the donor-accepter

interface and their dissociation, so that the separated electron and hole can migrate to their respective electrodes [8]. The organic semiconductor molecular arrangement and morphology directly impacts the migration of the excitons, and the electronic structure of the organic semiconductor also drives the relevant excited-state dynamics involved upon light absorption. Thus, the future use of bilayer OPVs highly depend on consistent film processing over large areas and continuing to understand and optimize the exciton dynamics.

1.3 Processing organic semiconductor thin films

Organic semiconductors have weak van der Waals interactions between molecular building blocks which make them amenable for flexible processing. This flexibility, however, also hinders consistent fabrication reproducibility given the variety of crystal polymorphs, molecular arrangement, and morphologies that a given organic semiconductor can adopt. I discuss some of the strategies that others have developed to achieve a desired final film structure, and some crystalline microstructures encountered in thin film processing.

1.3.1 Processing methods

Conventional thin film fabrication relies on chemical or physical vapor deposition to fabricate high-quality single crystals [9]. Chemical vapor deposition (CVD) uses a chemical vapor precursor gas that breaks down under specific reaction temperatures to bond to and coat a substrate [10]. Physical vapor deposition (PVD) uses a solid or liquid precursor that sublimates or vaporizes and then condenses onto a substrate [11]. One of the advantages of PVD is the use of lower temperatures than CVD to coat a substrate [10]. Sometimes vapor deposition produces amorphous (i.e., glassy, kinetically-trapped) organic semiconductor films, which offers the opportunity for post-deposition modification to tune the film to optimize final properties or obtain the desired structure [12–15]. For example, Hiszpanski, A.M. *et al.*, accessed three different polymorphs of hexabenzocoronene thin films that each had distinct molecular orientations by alternating the sequence of thermal and solvent vapor annealing [12]. Solvent vapor annealing consisted of placing films in a covered solvent reservoir, where the correct solvent choice carefully induces molecular reorganization and crystallization by disrupting the Van der Waals forces between molecules and molecular interactions with the substrate [14]. Other methods that tune film structure include patterning the substrate, applying external fields (e.g., electric, magnetic, strain), and varying the substrate temperature [13, 14]. Post-deposition modification offers an additional knob to control crystallinity, molecular orientation, and packing that cannot be achieved by chemical design alone.

Solution processing organic semiconductors enables inexpensive and low-temperature printing on flexible substrates, unlocking new ways to incorporate semiconductor thin films in device architectures. Solution-processing methods can be divided into four categories: dropcasting, spincoating, printing, and meniscus-guided coating [16]. Dropcasting involves the evaporation of the solvent to precipitate crystals. Spincoating achieves uniform film thick-

ness by dropcasting solution onto a substrate that is spun at high velocity. Printing methods share the ability to facilitate large-area deposition with various ways of spatially depositing the material; examples of printing include spraycoating and inkject printing. Meniscus-guided coating techniques, such as the prevalent blade-coating method, center around the linear translation of a meniscus to guide crystallization alignment [16]. Overall, solution-processing methods provide facile large-area and scale production opportunities for organic semiconductors.

The modification strategies for PVD and CVD described above may also be applied for solution-processing methods. Additional modification strategies for solution-processing can be categorized based on whether they influence nucleation or crystallization. Strategies to control nucleation generally impact the barrier to nucleation or its rate, where experimental parameters such as the surface and interfacial energies, vapor pressure, or the enthalpy of sublimation contribute to nucleation dynamics [17]. Patterning substrates to define regions of preferred nucleation or using soluble additives to encourage heterogenous nucleation are a couple of methods that control nucleation [16]. Modifying crystallization of the films, however, offers more options and possibilities in controlling film structure. The substrate temperature, deposition rate or method (e.g., meniscus alignment, directed flow), and surface chemistry and roughness all influence properties such as crystalline quality, domain sizes, and film coverage [16]. A combination of solution-processing thin film methods with pre- and post-modification strategies is shown in Reference [18], where Lee, S.S. *et al.* employed an organic semiconductor additive to seed the nucleation of triethylsilylethynyl-anthradithiophene (TES-ADT) films and systematically change grain sizes as a function of the additive with spin coating or solvent vapor annealing. While processing organic semiconductor thin films can be challenging to optimize, a suite of existing and forthcoming strategies addresses these challenges while providing greater insight into the crystallization of these materials.

1.3.2 Crystalline microstructures

Organic semiconductors form a variety of microstructures and morphologies that depend on the identity (structure) of the organic molecule and on the processing conditions. The different microstructures and morphologies influence the final charge transport capabilities of the thin film. Some general considerations when characterizing these structures and morphologies include identifying the different crystal polymorphs (i.e., crystal structures) available to the organic semiconductor, whether the films have amorphous and/or crystalline regions, and considering the types of grain boundaries and grain shapes induced by the morphology [19]. Grain boundaries, for example, may impede efficient charge transport by acting as a trap site or energetic barrier [4, 20]. The ideal thin film consists of aligned, large area, single crystalline domains that minimize grain boundaries with an electronically desirable polymorph in order to achieve high charge-carrier mobilities [21]. Since the single crystalline domains are similar to a 2D plate (not necessarily circular), these type of thin films can be called a platelet film [22]. A single platelet grain consists of a single crystal with a specific orientation; however, multiple platelet grains with different crystal orientations can

share a common nucleus, creating a multiple wedge-shaped platelet pie in appearance [22]. Essentially, platelet films change in structure depending on the number of grain boundaries in the film, which dictate the size of a single grain and may influence charge transport capabilities.

Spherulites represent another polycrystalline microstructure distinct from platelet films. The individual crystallites are typically much smaller, e.g., 10s of nm rather than μm or even mm platelet grains. They are a ubiquitous polycrystalline circular structure in organic semiconductor thin films. They demonstrate poorer charge transport capabilities than their platelet counterparts due to the multiple low-angle grain boundaries [22, 23], but their charge isotropy may be advantageous for specific applications [24]. Although spherulites are polycrystalline, their grains are highly ordered and gradually sweep out a full change in 360° orientation as one follows a circular path about the spherulite nucleus, often with needle-like crystallites as seen in Figure 1.1 [25]. Spherulites share these common features despite manifesting with a variety of appearances and morphology (Figure 1.1). Although a generalized theory for spherulite crystallization across materials remains elusive, there are a few common concepts that may be helpful for understanding spherulites. The driving force for spherulite growth depends on how supercooled the initially deposited amorphous films are, which is characterized by the difference in temperature between the melting temperature (T_{m}) of the material and the growth temperature [25]. As the growth temperature decreases (i.e., increased supercooling), the morphology achieved from annealing changes from single crystals (closer to T_{m}) to spherulites [25]. Most materials follow this trend; however, spherulites can also grow near the T_{m}. Consequently, the relationship between molecular translational and rotational diffusion, which drives crystal growth, depends on the supercooling regime. Close to the glass transition temperature and at increased supercooling, translational and rotational diffusion decouple. [25].

Non-crystallographic branching has been proposed as the mechanism that underlies the space- and orientation-filling distribution of spherulites [25, 26]. Essentially, new branches at the growth front have a slight misorientation relative to the parent branch, and the accumulation of misorientations with new branches lead to the spherulite formation [26]. The cause for the slight misorientation of the new branches is still contested, where response to internal stress of the crystal is one suggestion [25]. Simulations that account for various aspects of spherulite growth such as kinetic and interfacial free energy, diffusion, and non-crystallographic branching reproduce a variety of spherulites [26], but high-resolution imaging of spherulite crystallization will corroborate the simulations and provide further insight into the cause for spherulite growth mechanisms. Brendan Folie, a previous group member, expands upon spherulite crystallization and simulations specific for rubrene spherulites in his thesis [27].

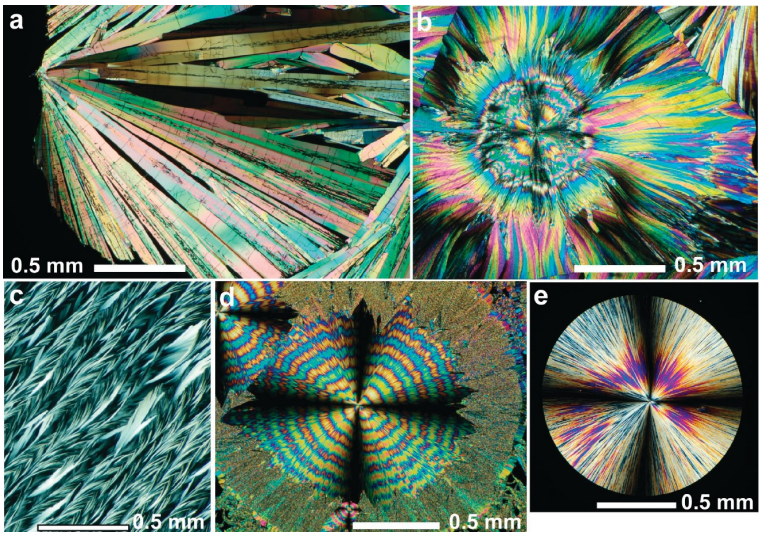

Figure 1.1: Morphologies of spherulites in thin films under polarized optical microscope. Examples of different types of fibers: straight (a,d,e), bent (b,c), twisted (d,e). Spherulites formed from (a–d) hippuric acid at 170, 80, 90, and 75–85°C, respectively, and (e) resorcinol containing 10 wt % tartaric acid at 21°C. Reprinted with permission from Reference [25] Shtukenberg, A.G., Punin, Y.O., Gunn, E. and Kahr, B., Spherulites. Chemical Reviews, 2012, 112(3), 1805-1838. Copyright 2012 American Chemical Society.

1.4 Multimodal characterization

Multimodal characterization provides an opportunity to study how the hierarchical organization of heterogeneous material impacts functionality. Combining different characterization modalities overcomes any individual technique's limitations (e.g., spatial resolution, chemical specificity, dynamics) to construct a complete understanding of structure-function properties. Multimodal characterization approaches can be classified by the degree of spatial correlation across datasets, which can help assess the benefits and challenges to address in experimental design [28]. One type to consider is the combination of imaging data and macroscopic (non-image) measurements (e.g., optical microscopy with X-ray scattering), where an established relationship between the two datasets informs on properties like the identity of the material. Here, the key challenge is to construct the relationship rather than spatially correlating two image datasets since one of the datasets is not an image. Another type of multimodal characterization is when two different imaging modalities probe different spatial regions. In this case, the datasets can be directly compared only if the sample is known to be spatially uniform, or if there is a sufficient amount of data from both modalities to inform on the average spatial features and then conduct a comparison. A third type of multimodal characterization is when different types of imaging datasets are taken of the same spatial regions so that they directly correlate with one another. Co-registration of the images is executed to correlate the data, so that for a given spot, one can extract multiple types of properties found

from the different modalities. A fourth type of multimodal characterization occurs when the different modalities are spatially incongruent, such as surface imaging and volume imaging. In this case, the main difficulty is establishing the relationships or conditions that determine whether the images can be combined (e.g., how can a 2D dataset map onto a 3D dataset?) [28]. This is a subtle distinction from the first type of multimodal characterization since the modalities involved both offer spatial resolution. Despite the challenges of synthesizing different characterization modalities and resolving dataset interpretation, the multimodal approach provides powerful insight that deciphers the intricate properties of materials.

The following sections highlight characterization techniques used in the dissertation. These techniques span the Å, nanometer, and micron length scales to probe the crystal structure and mesoscale morphology or microstructure of organic semiconductor thin films. The techniques are also capable of capturing dynamics that resolve processes as disparate as structural formation and charge transport. Together, these modalities span enormous lengths and time scales and provide a powerful perspective into the physical and energetic landscape. Many of these characterization techniques induce radiation damage in soft materials like organic semiconductors, given their weak bonding interactions, so mitigation strategies are also discussed throughout the thesis (e.g., reducing exposure time or flux, rotating the sample, cryogenic conditions), and non-invasive optical approaches serve as an important complement.

1.4.1 X-rays and electrons

To probe the molecular length scales of materials, X-rays and electrons are used since they can achieve wavelengths on the nanometer to picometer length scales. X-rays have wavelengths between 0.1 - 10 nm; electron wavelengths (λ) depend on the accelerating voltage, which can be calculated by the de Broglie equation: $\lambda = h/p$, which shows that wavelength is related to the Planck constant h and momentum p. Momentum can be expressed as $p = \sqrt{2mK}$ with the mass of the electron (m) and the kinetic energy K written in energy units electron volts using the accelerating voltage (e.g., one keV of energy for one electron accelerated by 1 kV). The relationship between K and p stems from $K = \frac{1}{2}mv^2$ and $p = mv$, where v is the electron velocity. More precise calculations of electron wavelength for high-energy electrons modify the de Broglie equation by accounting for relativistic effects [29]. X-ray and electron-based techniques unpack similar information about materials, such as crystal structure and molecular arrangement, orientation, strain, and even surface morphology. However, differences in their interactions with matter and experimental conditions often determine the choice of the technique. For example, the strong interaction of incident electrons with the sample's atoms and electrons leads to sample damage for soft materials, and the multiple signals that arise from the interaction may obscure the signal (e.g., inelastic phonon scattering background) [30, 31]. X-rays do not directly provide information on phase, unlike electron-based techniques (although high-resolution microscopy is needed), and require additional analysis to retrieve the phase [32]. Transmission electron microscopy (TEM) requires very thin samples on electron-transparent substrates, while sample param-

eters for X-ray measurements are not as restrictive but depend on the technique. TEM can, however, provide both real-space images and diffraction information simultaneously. These are but a few examples of considerations for choosing electron or X-ray measurements, and further discussion can be found in references [30] and [33] as a starting point.

I now briefly describe the X-ray and electron characterization techniques used for work in this dissertation, although this description is not meant to be exhaustive in breadth and scope of the world of X-ray and electron characterization and their underlying principles. Reference [34] was invaluable for an overview of X-ray techniques and their relationships with one another, and Reference [35] describes in more detail the underlying fundamental principles of X-ray techniques.

X-ray scattering and microscopy

Grazing incidence wide-angle X-ray scattering (GIWAXS) helps determine the crystallinity (or order) of a film and its crystal structure, measure the lattice spacing in the crystal structure, and estimate the crystalline grain size or coherence length [34]. In grazing incidence geometry, the incident X-ray scatters close to below the critical angle (α) of the substrate, which is the angle below which the X-ray exhibits total external reflection, to probe the film surface (Figure 1.2) [34, 36]. Adjusting the incident angle so that it is slightly higher or lower relative to the film surface, while staying below the critical angle, changes the penetration depth of the X-ray such that it scatters either into the bulk or along the surface [34]. The critical angle can be calculated from the X-ray refractive index contrast between the film and air or scattering length density [36], but an online calculator such as the one available from The Center for X-ray Optics [37] computes the angle for elemental substances and is often used as a starting point.

The magnitude of the scattering vector is $q = (4\pi/\lambda)\sin(\theta)$, where λ is the X-ray wavelength, and the scattering angle is 2θ. The X-rays must scatter off of the lattice and meet the Bragg condition to constructively interfere: $q = 2\pi/d_{hkl}$ where d_{hkl} represents the distance between adjacent planes designated by Miller indices h, k, l [34]. A detector (typically 2D) captures the constructively interfered X-rays as a strong intensity peak that represents the position of the lattice in reciprocal space from which the real-space unit cell is reconstructed [34]. The shape of the peaks qualitatively describe the crystalline orientation of a film. Random orientations of crystallites yield an arc, while highly ordered films produce diffraction spots (Figure 1.3a-b, respectively) [34, 38]. When there is a distribution of preferred orientation (e.g., prefer out-of-plane but isotropic in-plane), the diffraction spot appears smeared with a smaller arc shape (Figure 1.3c).

Understanding the effect of processing conditions on crystallinity and ordering is a routine question in GIWAXS measurements. For example, in a comparative study before and after thermal annealing at 140°C for semiconducting polymers PQT-12 and PTTT, post-annealing diffraction patterns suggested increased crystallinity in the polymers as exhibited by the additional higher-order and mixed peaks including some from the polymer backbone [39]. In another study, the polymer backbone orientation changed based on the substrate

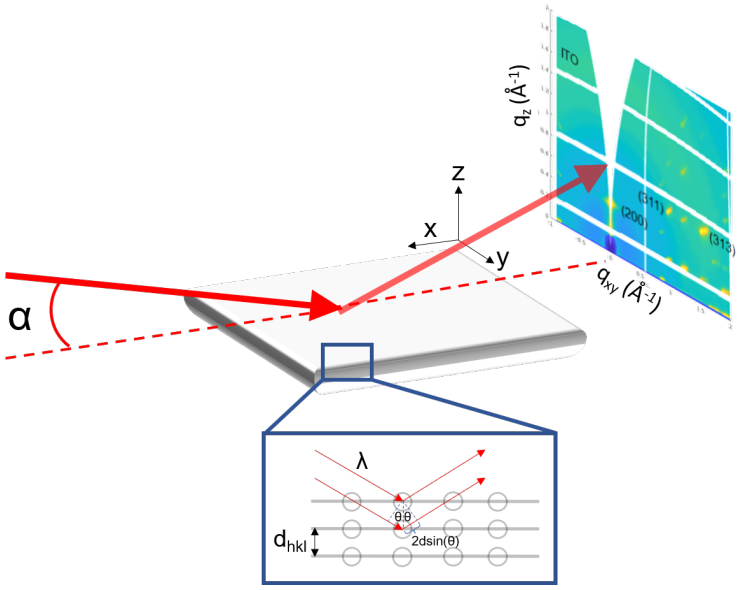

Figure 1.2: GIWAXS setup and Bragg's law illustration. The incident X-ray scatters off the sample at an angle α and onto a 2D detector to generate a reciprocal-space plot of q_z and q_{xy}. The Bragg condition for constructive interference is illustrated with example lattice planes below the sample in the GIWAXS setup. The distance between the detector and sample determines wide-angle scattering mode, which probes smaller real-space length scales than small-angle scattering mode (detector-to-sample distance is larger).

temperature during the friction-transfer process, where the backbone exhibited π-stacking out-of-plane at lower substrate temperatures and π-stacking parallel to the substrate at higher temperatures [14]. GIWAXS also provided evidence of isomer mixtures inhibiting crystallization to maintain a glassy condition for organic semiconductors [40], and in a dynamic measurement, diffraction snapshots of a polymer solution blend drying after dropcast revealed the crystallization stages of the different polymers [41]. Dynamic measurements offer powerful insight into the crystallization dynamics on time scales as short as seconds, which increase understanding of structural formation. GIWAXS offers essential insight for tuning molecular structure to control resulting function.

Although conventional X-ray scattering typically averages over the sample, the X-ray beam can be focused to sizes smaller than 10 μm to better probe heterogeneous or polycrystalline samples. Microdiffraction relies on focused X-rays to obtain diffraction patterns with high spatial resolution by raster scanning the sample on a stage and collects the scattering with an area detector [42, 43]. To achieve a focused X-ray, reflection, diffractive, or refractive X-ray focusing optics must be used [35, 43]. A common reflection geometry to focus the X-ray beam relies on Kirkpatrick-Baez mirror pairs, which are two curved mirrors set at right angles relative to each other to focus the beam in both horizontal and vertical directions [35, 43]. An advantage of using reflective X-ray optics is their achromaticity, which is valuable

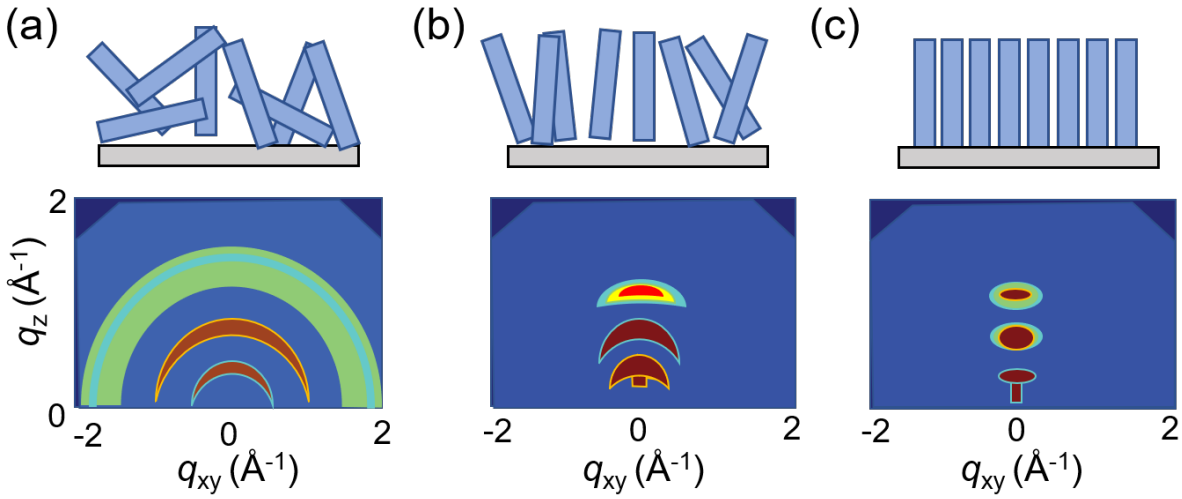

Figure 1.3: Illustration of relationship between crystallite orientation and diffraction peak shape. (a) Random crystallite orientation yields smeared arc-like diffraction peaks. (b) Semi-oriented distribution of crystallites with preferential direction, such as out of plane, have less pronounced arc shapes. (c) Highly oriented crystallites produce spots. Colors correspond with peak intensity with red being more intense than green and blue. Cartoon adapted from Figure 11 in Reference [34].

for microdiffraction since data can be collected with both mono- and polychromatic X-rays [43].

Choosing between monochromatic and polychromatic microdiffraction measurements depends on the sample properties. If the polycrystalline sample's grain size is smaller than the beam (i.e., nanocrystalline), a monochromatic X-ray is typically used and provides a powder-like diffraction pattern of rings, where the rings appear continuous for randomly oriented crystallites [43]. The crystal structure, phase, stress, and strain can be obtained from a monochromatic microdiffraction measurement [43]. If the sample's grain size is larger than the beam, a polychromatic X-ray can be used and yields a Laue diffraction pattern that is a result of overlapping diffraction patterns from all crystallites in the X-ray path [43]. A significant advantage of polychromatic Laue diffraction is that the Bragg condition is met for different reflections simultaneously, which obviates the need for sample rotation [42]. Crystallite orientation, deformations or defects, and strain are found from polychromatic Laue diffraction patterns [43]. Both polychromatic and monochromatic X-rays can be used for a given sample, where a polychromatic measurement can help determine specific X-ray wavelengths of interest to further probe. Ultimately, microdiffraction provides the opportunity to spatially map information about crystallization, orientation, or deformation in a material which greatly augments other characterization methods.

X-rays not only measure the crystal structure in reciprocal space but can also be used to generate real-space images. Scanning transmission X-ray microscopy (STXM) employs a

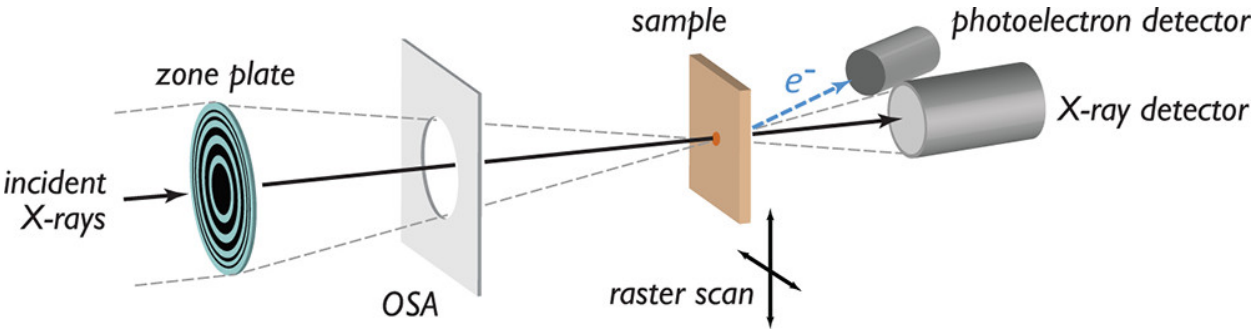

Figure 1.4: General STXM setup. Incident X-rays are focused by a zone plate and first-order X-rays pass through the order sorting aperture onto the sample as it is raster scanned. The X-ray detector records the transmission intensity, and a photoelectron detector may also be considered to simultaneously collect emitted electrons from the surface. Reprinted with permission from [34] Rivnay, J., Mannsfeld, S.C., Miller, C.E., Salleo, A. and Toney, M.F. Quantitative determination of organic semiconductor microstructure from the molecular to device scale. Chemical Reviews, 2012, 112(10), 5488-5519. Copyright 2012 American Chemical Society.

focused X-ray beam tuned to the desired X-ray wavelength that generates an elemental composition map based on differential absorption. Effectively, STXM combines microscopy and spectroscopy together. We can understand the principles of X-ray absorption through near-edge X-ray absorption fine structure (NEXAFS) spectroscopy. In NEXAFS spectroscopy, the absorption intensity of excited core electrons near the photoionization threshold is recorded as a function of soft X-ray energy, typically 100 - 1000 eV (the hard X-ray counterpart is known as X-ray absorption near-edge structure, XANES) [34, 44]. The resulting absorption spectra features the elemental absorption edges found in the sample and contain fine structure information that encodes local bonding and chemical bonding environments and molecular orientations [44]. For organic semiconductors, the transition from the carbon 1s edge to the π^* resonance is a significant reporter on molecular orientation given the strong resonance due to the highly conjugated system [34]. Using a linearly polarized X-ray will uncover the orientation, where orientations parallel to the X-ray polarization manifest as peaks in the NEXAFS spectrum (e.g., out-of-plane X-ray polarization will be resonant with out-of-plane π orbitals) [44]. In a STXM experiment, the NEXAFS spectrum is often collected first to determine X-ray energies of interest for mapping purposes.

In a typical STXM setup, the linearly polarizable and tunable X-ray is focused by the zone plate, which is a key diffractive X-ray optic so that STXM images achieve spatial resolution as small as 25 nm (Figure 1.4) [45]. The zone plate has alternating transparent and opaque rings or zones, where the outer width dictates the resolution [35]. The polarized X-rays that pass through the transparent zones constructively interfere, and only the first-order X-rays pass through the order sorting aperture so that contrast is maximized when the polarized X-ray is focused onto the sample. The sample is raster scanned, and absorption as a function of position is collected at the detector. Other detection modes in a STXM geometry

include fluorescence (the emission of radiation) to generate another type of elemental map, or photoelectron emission, which informs on surface composition and chemistry [35]. The composition maps obtained from STXM characterize heterogeneity in samples like organic semiconductor films such as determining the extent of phase segregation in blends [34]. Studies that use multiple X-ray polarizations for a given sample can yield maps describing grain and domain orientation [34]. STXM is a powerful tool that provides a nanoscale view into the chemical landscape of a given material.

4D-scanning transmission electron microscopy

Transmission electron microscopy (TEM) routinely characterizes samples on the nanometer-to-subnanometer length scales [38]. Electrons scatter, absorb, or diffract off of the sample, which produce real-space morphological images (however, only 2D information), information on elemental compositions, or diffraction patterns [38]. TEM has been instrumental in clarifying organic molecular film properties such as grain size, connectivity, and crystalline order [34]. A general TEM setup has an electron gun producing monochromatic electrons that are focused by two condenser lenses that control the size of the beam incident on the sample [46]. An aperture filters out unwanted high-angle electrons to minimize unwanted scattering in the image formation. The beam transmits through the sample and is enlarged with lenses before it strikes the image screen.

In conventional TEM, a parallel electron beam transmits perpendicularly through the sample. A recent and expanding variation of TEM is 4D-scanning TEM (4D-STEM), where the electron beam is focused at high angles to converge at a focal point with spot sizes as small as 0.5 - 50 nm in diameter [47, 48]. The probe is rastered across the sample, and a 2D-diffraction pattern from scattered electrons is collected at each point in the 2D grid - hence the 4D designation (example shown in Figure 1.5) [49]. 4D-STEM is often used to generate crystalline orientation and strain maps and can measure phase contrast [49].

Advances in electron detector technology facilitated the implementation of this powerful technique. In particular, detectors for 4D-STEM measurements need to match the scanning rate of the probe, which only dwells on a given spot on the order of μs to ms, and measure both high and low intensity signals simultaneously [49]. Hybrid-pixel array detectors are typically used in 4D-STEM experiments for their single electron sensitivity, fast acquisition and readout speeds, and dynamic range [49, 50]. Additionally, aberration-corrected TEMs supported the growth of 4D-STEM to achieve higher spatial resolutions, but this is not necessarily a requirement [49, 51]. As the next-generation electron detectors become more accessible, 4D-STEM is likely to grow in accessibility, too, but some of the subsequent challenges to address for 4D-STEM experiments focus on large data management acquisition and developing computational infrastructure for data processing and analysis [49, 52].

Conventional TEM has limited application for organic molecule samples due to electron beam damage and low contrast [34]. Sample preparation is also challenging because organic semiconductor film processing conditions may need adjustment in order to fabricate films thin enough for electron transmission. 4D-STEM demonstrates strong potential for imaging

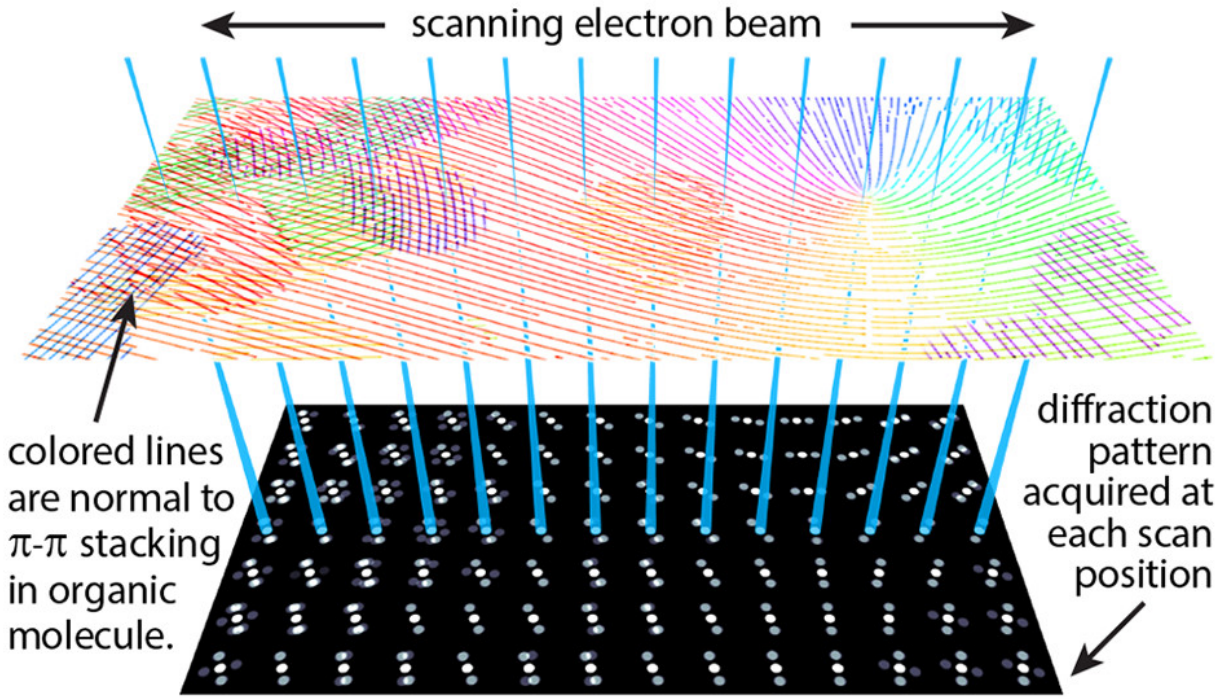

Figure 1.5: Representation of 4D-STEM measurement with orientation map. In 4D-STEM, a scanning electron probe collects a 2D-diffraction pattern at each spatial point. The diffraction pattern can inform on properties such as crystal orientation and be translated into an orientation map shown by flowline colors. Reprinted with permission from [48] Bustillo, K.C., Zeltmann, S.E., Chen, M., Donohue, J., Ciston, J., Ophus, C. and Minor, A.M. 4D-STEM of beam-sensitive materials. Accounts of Chemical Research, 2021, 54(11), 2543-2551. Copyright 2021 American Chemical Society.

organic molecule samples with the growing curation of experimental parameters that can be controlled to mitigate damage and enhance contrast. Examples include cooling the samples only during electron irradiation, optimizing the probe convergence angle to boost the signal, controlled electron fluence, and the use of an electron camera [48]. Advances in data analysis treatment of 4D-STEM data, such as more robust calculation methods to determine the orientation of diffraction patterns [53, 54], also greatly improve the opportunities to study sensitive and more complicated polycrystalline samples. 4D-STEM will mature as an effective characterization technique with very high spatial resolution for organic semiconductor films.

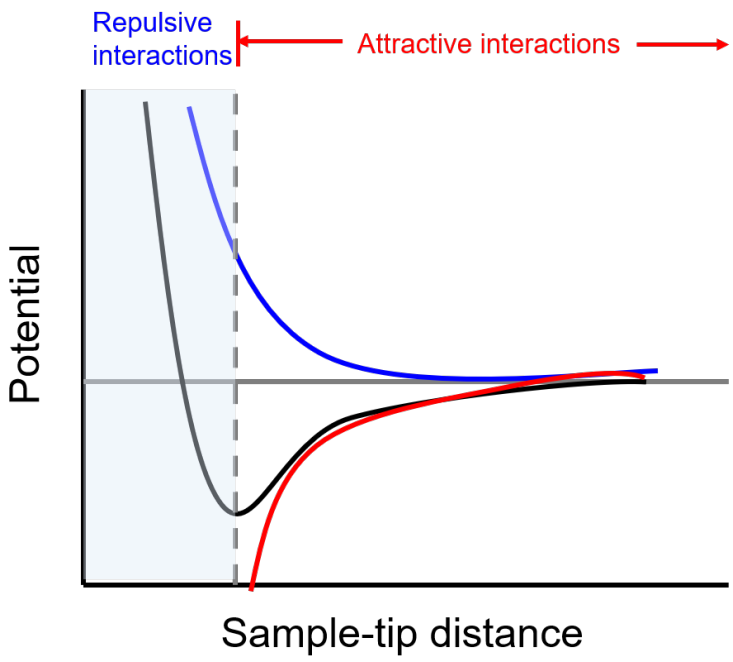

Figure 1.6: Leonard-Jones potential for AFM tip-sample interaction. The Leonard-Jones potential, $U_r = 4U_0[(\frac{R_a}{r}^{12} - \frac{R_a}{r}^{6})]$, (black) approximates the repulsive (blue) and attractive (red) interactions that describe sample-tip interactions in AFM. U is the potential, U_0 is the minimum potential, R_a is the distance at which U is 0, and r is the distance between atoms. Repulsive interactions are proportional to $1/r^{12}$, while attractive interactions are proportional to $1/r^6$. U_0, or also when the force gradient is zero, delineates the regimes for attractive or negative interactions (forces). Figure adapted from Reference [55].

1.4.2 Scanning probe microscopies

Atomic force microscopy

Basic atomic force microscopy (AFM) maps the surface topography on the nanoscale (i.e., 10 - 100 nm) based on the surface-tip interaction. The Lennard-Jones potential, generally describes the forces involved in these surface-tip interactions that produce AFM images as shown in Figure 1.6 [55]. When the tip is close to the surface and the distance is comparable or smaller than a chemical bond, repulsive forces due to electrostatic repulsion and Pauli exclusion occur between the atoms of the tip and sample. As the r separation increases to be longer ranged, van der Waals forces describe the fluctuating dipole attraction between the sample and tip. At and beyond a certain large sample-tip distance, there is no force between the sample and tip. Consequently, these changes in force that bend the cantilever attached to the tip and can be mapped to the surface topography.

The beam deflection method is a common way of capturing the deflection of the cantilever.

In this AFM configuration, a laser reflects off of the back of the cantilever onto a detector. To illustrate the mechanics, we start with contact mode operation. This mode of AFM maintains a constant force between the surface and tip, which requires a constant deflection of the cantilever (that can be described by Hooke's law) [55]. As the tip scans over the surface and encounters variations in topography, the sample-tip force changes, which alters the cantilever deflection, too. In order to maintain the original deflection and force, the electronics adjust the sample-to-tip distance accordingly. Simultaneously, the laser position on the detector changes as the cantilever shifts, which translates into AFM data. In contact mode the tip is in contact with the sample (thus operating in the repulsive regime), which means that sample damage is more likely if a soft tip is not used [55].

Now that we have discussed the beam deflection method using contact mode to demonstrate its operation, we continue with the most common choice for AFM under ambient conditions – tapping mode. The tip only intermittently contacts the surface as the cantilever oscillates close to its resonance frequency [55] with a large amplitude. The detection feedback loop relies on changes in the amplitude of the oscillation as the sample-tip interaction changes. A harmonic oscillator model approximates the dynamics involved, where we can relate the important quantities of frequency (ω), amplitude (A), phase (ϕ), and distance (d) as $z = A\cos(\omega t + \phi)$. Phase change can be mapped as a free signal (not used for feedback) when energy losses (in air or liquid) dampen or cause a delay in oscillation [55]. Tapping mode avoids sample damage issues due to the tip's intermittent contact, yet, also provides high resolution of a variety of landscapes including those of soft materials like organic semiconductors.

We have barely scratched the surface of AFM's capabilities and suggest reference [55] for a comprehensive review. Although AFM can only probe the surface of a material, it is an extremely versatile technique that can also report on the chemical, mechanical, and electrical properties of materials on the nanoscale [56–59]. For example, conductive AFM on 2,8- difluoro-5,11-bis(triethylsilylethynyl) anthradithiophene (diF-TES ADT) and poly(triarylamine) (PTAA) blend films demonstrated that a 50% blend of diF-TES ADT:-PTAA achieved similar charge transport efficiency at low temperatures as pristine diF-TES ADT, yet, also achieved increased carrier mobility [57]. When AFM is combined with other characterization or imaging techniques, such as mapping the transient absorption spectra of TIPS-pentacene microcrystals with their topography [59], we gain unparalleled insight into how surface morphology impacts structure-function properties.

Infrared scattering-scanning near-field optical microscopy

Infrared scattering scanning near-field optical microscopy (IR *s*-SNOM) leverages the nanoscale resolution afforded by AFM and adds chemical specificity. In addition to the laser that reflects off the back of the cantilever, a broadband and wavelength-tunable laser scatters off of the AFM tip itself, which generates a localized near-field enhancement around the tip and the sample [60]. In the simplest form of IR *s*-SNOM, elastic scattering is the optical contrast mechanism measured interferometrically so that changes in amplitude and phase

of the scattered light are tracked [60–62]. Other properties encoded in the optical response of the sample that influences the elastic scattering include the absorption coefficient and optical refractive index [61]. These properties are encoded in the IR spectra, which can lead to information about chemical identity, local ordering, or intra- and inter-molecular coupling as a function of space on the nanoscale [63].

1.4.3 Optical microscopy

Optical microscopy non-destructively visualizes materials on the micron-to-sub-micron length scale with a large field of view. This quickly helps to assess general features such as shape and domain sizes. Optical microscopy also provides indirect orientation information through color contrast when crossed-polarizers are used to study optically anisotropic crystalline materials. First, unpolarized light passes through the first polarizer and becomes linearly polarized; then it transmits through the crystalline sample. Anisotropic materials have a range of refractive indices that varies with orientation [64]. If the linearly polarized light is parallel to the fast or slow axis of the (birefringent) material, the incident light's optical properties remain the same as it transmits the sample. The second polarizer (i.e., analyzer), however, is oriented orthogonal to the first polarizer. Subsequently, the transmitted polarized light that passes through the sample will not pass through the analyzer, which leads to a dark field by eye. Now, if the linearly polarized light is not parallel to the fast or slow axis, then the light is split into two wave components that are perpendicular to one another with different velocities. They become out of phase with respect to one another but recombine through constructive and destructive interference through the analyzer. The final result is that the sample appears bright by eye with some color if using incident white light [64]. Since maximum brightness occurs when the slow axis of the crystal is either 45° or 135°, we cannot distinguish orientation without an additional retardation plate, compensator, or Normarski prism that sandwiches the sample [65]. Hattori, Y. and Kitamura, M. proposed finding crystal orientation of organic monolayer islands without additional components by recording the contrast as a function sample stage rotation under crossed-polarizers [66]. The authors determined the optimal angle at which the pre-sample polarizer should be set relative to the fixed post-sample polarizer and the wavelength that maximized the contrast between $\theta = 45°$ and 135°. This required the statistics of many islands, however, and may prove to be a little more challenging for more polycrystalline samples.

1.4.4 Absorption and fluorescence

Bulk absorption and fluorescence measurements provide key information on the electronic structure of a material. We often use them to identify electronic transitions to excite or probe with other pump-probe techniques, and they also help with experimental design choices such as sample concentration or impact of solvent. Of course these techniques can be modified such that the measured information contains polarization dependence, time resolution, and even spatial resolution. For example, time-resolved fluorescence (or photoluminescence, PL)

tracks the PL decay of a sample. The PL lifetime informs on the kinetics of a molecule and related dynamics such as energy transfer. Probing the sample with polarized light augments absorption and fluorescent data to learn about the transition dipoles of a molecule and properties like rotational mobility. When a microscope images absorption and fluorescent information in materials, electronic properties can now be spatially mapped and resolved. Confocal fluorescence microscopy is one of the most significant techniques to unlock this information, where only emission that is confocal to the detector pinhole generates the final image with reduced background emission (Olympus citation). As an example of the rich information that can be discovered through absorption and fluorescence spectroscopy, Irkhin, P. *et al.* identified the vibrational modes responsible for a vibronic progression observed in the absorption and emission spectra of rubrene single crystals [67]. They also found that absorption and emission occurred most strongly in the out-of-plane crystal axis.

1.4.5 Pump-probe microscopies

Transient Absorption Microscopy

Transient absorption microscopy (TAM) combines ultrafast pump-probe spectroscopy with an optical microscope to spatially resolve excited-state dynamics of materials. The pump pulse is set to a specific wavelength to induce a specific absorptive transition, and the response is measured by the change in absorption or transmission of a white light (or single-color) probe pulse [68]. Conventional TA spectroscopy beam spot sizes are typically on the order of hundreds of microns, which spatially averages the signal. By focusing the pump through an objective in TAM, the spot size decreases by an order of magnitude to several microns or even nanometers in diameter instead.

Figure 1.7 provides a simplified schematic of our TAM setup to further explain some key aspects of TAM (Appendix A of Brendan Folie's thesis [27] contains a complete explanation of the TAM setup). The chopper wheel in the pump beam path rotates at a frequency to alternatively block and allow passage of the pump pulse so that the final measured signal is the change in probe intensity (or optical density, OD) with the pump "on" and "off": $\Delta OD = -\frac{\Delta T}{T} = \frac{T_{\text{pump-on}} - T_{\text{pump-off}}}{T_{\text{pump-off}}}$, where T is the transmitted probe intensity. The polarization-dependence of the signal can be obtained by changing the polarization of the pump or probe with a polarizer. A half-wave plate could be used to control the beam power, and the second half-wave plate in Figure 1.7 in the probe line after the polarizer ensures that the probe polarization can be changed without changing the power. Both the pump and probe reflect off of retroreflectors to eliminate dispersion or chromatic aberrations. The pump retroreflector is set on a delay stage to change the delay between the pump and probe, which is how the change in probe intensity can be measured as a function of time on the ps - ns timescales. The pump and probe respectively reflect and transmit through a beamsplitter so that they are collinear through the first objective as it focuses them onto the sample. The pump and probe pass through a second objective for recollimation after the sample, and the pump is filtered out. The probe is then dispersed by a diffraction grating and imaged onto

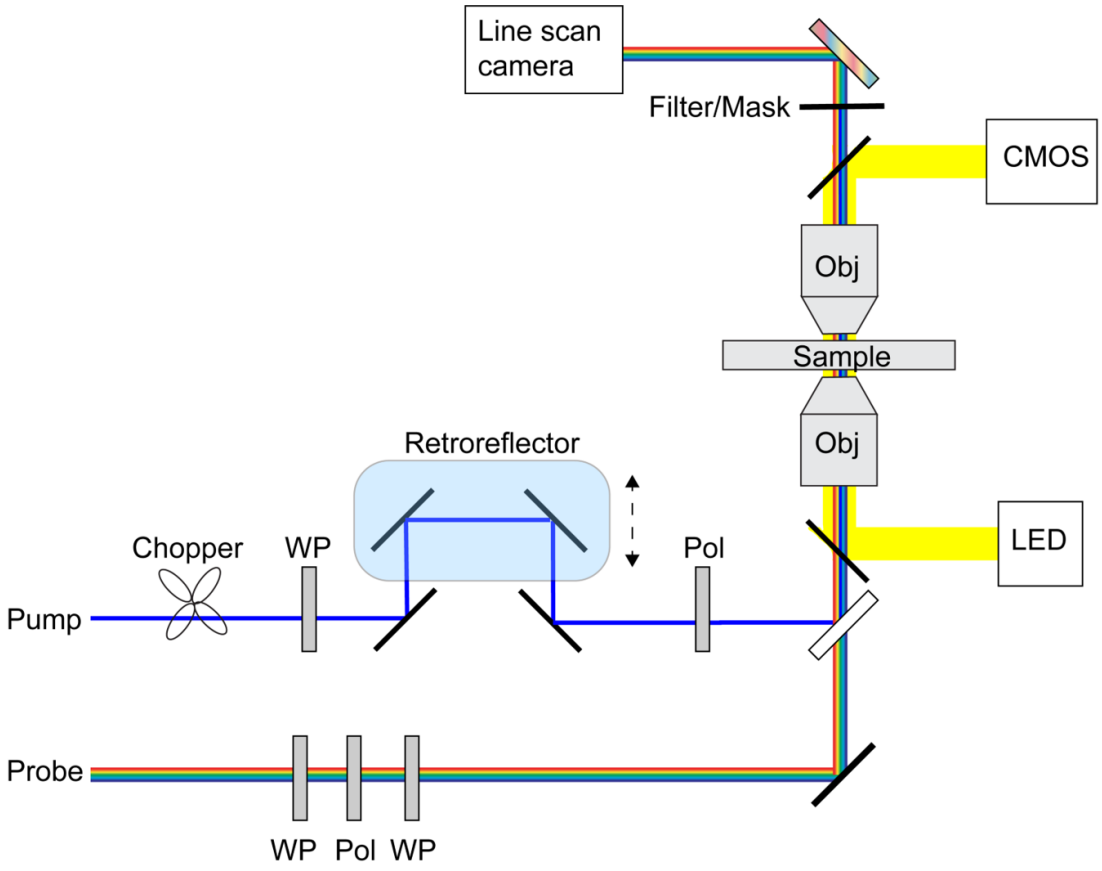

Figure 1.7: Simplified depiction of Ginsberg group TAM setup. The white light probe is generated by a Ca_2 crystal. Beamsplitter is shown as diagonal white rectangle. Optics abbreviations: WP = half-wave plate, Pol = polarizer, Obj = objective, LED = LED light, CMOS = complimentary metal oxide semiconductor camera. The light source is not shown; an oscillator and regenerative amplifier produce an 800 nm pulse that is used for both the pump and probe pulses. The wavelength of the pump pulse can be tuned by an optical parametric amplifier or BBO crystal in the visible wavelength regime. The pump pulse achieves ∼100 fs resolution.

a line scan camera. An optical image of the sample can be captured by an LED light and CMOS camera with mirrors on flip mounts.

There are three processes that lead to the most common TA spectral features after pump excitation (Figure 1.8). First we consider when the probe interacts with molecules that have been excited by the pump. One probe interaction induces further excitation of a molecule to a higher lying energetic state, which manifests as a positive optical density feature called an excited-state absorption (ESA) feature, which is a type of photoinduced absorption (PIA). Second, the probe could induce relaxation of the molecule in the form of stimulated emission (SE), which manifests as a negative optical density feature. Finally, we

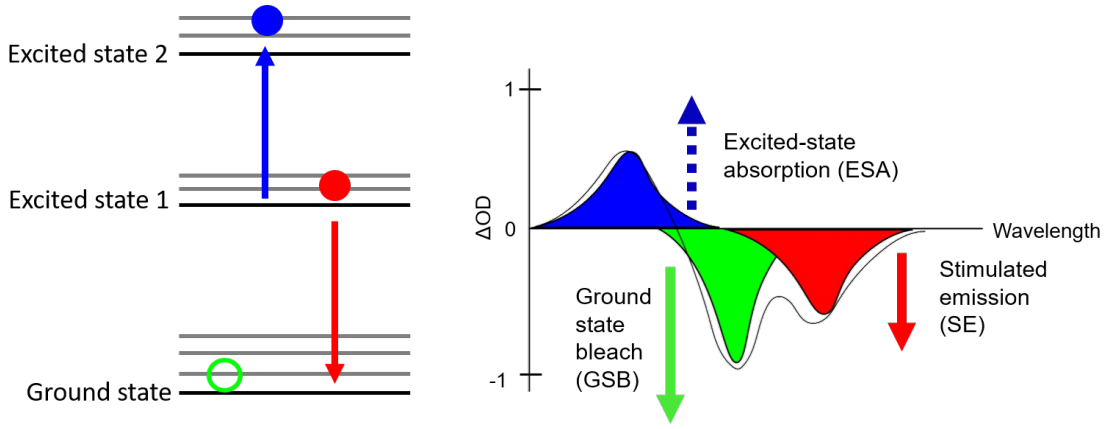

Figure 1.8: Illustration of TAM signal and spectral features. On the left, the energy diagram illustrates probe interactions with state populations after pump excitation. Empty circles represent a depleted state, and filled circles represent that the state has a population. On the right is a cartoon of the corresponding spectral features that emerge after pump excitation.

consider the transmission of the probe through a depleted ground state, which results in a negative optical density feature called the ground state bleach (GSB). Data can be plotted as a 2D color plot with multiple time delays (time on the vertical-axis and wavelength on the horizontal-axis), and we can take slices of this plot to look at specific time delays for comparison. The evolution of spectral features over time and their kinetic information are of interest to understand the dynamics at hand.

TAM probes spatial heterogeneity in order to understand how material morphology influences the charge carrier and exciton dynamics in a material [69]. For example, Wong, C.Y. *et al.* demonstrated that solution-cast films of 2,8-difluoro-5,11-bis(triethylsilylethynyl)anthradithiophene (diF-TES-ADT) exhibited a wide range of heterogeneity in the crystalline orientation of domains based on the distribution of time constants from polarized TAM [70]. Another example from Yuan, L. *et al.* found that better interlayer coupling and contact between WS_2 and graphene led to faster charge transfer, where better coupling exhibited a single-exponential decay with a time constant of $\sim$3 ps [69, 71]. TAM will remain an invaluable technique for spatially-resolving excited-state dynamics on ultrafast time scales, and further improvements, such as higher spatial resolution, or coupling the electronic information with vibrational probes, will expand its capabilities [69].

Stroboscopic scattering microscopy

Stroboscopic scattering microscopy (stroboSCAT) relies on changes in the index of refraction as the imaging contrast instead of absorption as in TAM. A confocal visible-light pump photoexcites a spot on the sample, which generates energy carriers, and a time-delayed wide-field probe that is spectrally shifted away from the band edge (to only track changes in

the index of refraction) illuminates this spot [6, 72]. The probe interacts with the locations of the energy carriers, and this scattered light interferes with the backscattered probe reflection from the sample-substrate interface [6, 72]. A CMOS camera captures this probe interference to generate a varying contrast profile mimicking the carrier density profile. Recording an image at a series of time delays provides the evolution of carriers, which often includes both expansion of the distribution (transport) and decay. The data can also be spectrally resolved to further inform on the spectral changes that accompany the excitation population dynamics [72]. Since the imaging contrast mechanism is the change in index of refraction, stroboSCAT probes any type of energetic carriers regardless of optical properties in a wide variety of materials and in three dimensions [72]. For example, the mechanism of energetic carriers diffusing across crystalline domains was captured by stroboSCAT, where the image contrast changed depending on whether the carriers approaching a grain boundary were close to the surface or below the surface in polycrystalline methylammonium lead iodide films [72] Essentially, stroboSCAT can be used as a universal spectroscopic imaging modality capable of mapping *in situ* dynamics in heterogeneous landscapes on the nanometer-to-micron scale.

1.5 Remaining chapters overview

Chapter 2 describes the synthesis of polarized X-ray, electron, and polarized optical microscopies to quantify the observation of a hybrid crystalline microstructure in rubrene thin films. We ascribe the existence of the hybrid microstructure to a finite rate of substrate temperature rise. Supporting measurements using scanning probe microscopy and X-ray scattering are also discussed along with future directions for experiments such as charge transport and comparative studies.

Chapter 3 explores the anisotropic behavior of inorganic lead halide perovskite nanowires with stroboSCAT, TAM, absorption microscopy, and polarized fluorescence. The exciton diffusion dynamics were mapped and observed the anisotropic band-edge electronic structure, which are consistent with the shape anisotropy and long-range exchange interaction.

These chapters together demonstrate the strength of multimodal characterization in offering remarkable insight on multiple length and time scales on the structure-function properties of semiconductors.

Chapter 2

Multimodal characterization of crystal structure and formation in rubrene thin films reveals erasure of orientational discontinuities

2.1 Introduction

Organic semiconductor films form a variety of microstructures that facilitate or inhibit electronic device functionality. For example, disordered grain boundaries in polycrystalline films and high-angle molecular orientation mismatch at such boundaries often correlate to poorer charge transport in thin film transistor geometries [23, 73, 74]. Processing-structure studies [17] provide guidelines for tuning structural order such as molecular orientation and crystalline grain size [75]. These studies are most effective at achieving a desired microstructure when both control of processing conditions and an understanding of the microstructure formation process can be developed.

Rubrene has one of the highest charge carrier mobilities of organic semiconductors at 20 $cm^2/(V{\cdot}s)$ in single crystal form and has been extensively studied for thin film applications [76, 77]. Depending on annealing conditions of an initially deposited amorphous film, rubrene can crystallize into different morphologies. At lower temperatures rubrene forms platelets, a collection of larger single-crystalline domains characterized by their wedge shapes that share a common nucleus, as shown in Figure 2.1a. At higher temperatures rubrene crystallizes into spherulites, polycrystalline macrostructures (Figure 2.1b), whose many nanoscale crystallites are ordered with their orthorhombic b-axes pointing outward from a single nucleus, so that the crystal orientation gradually rotates about the nucleus. The electronic functionality of rubrene and other thin film organic semiconductors depends strongly on the structure at multiple length scales. Deterministically relating bulk outcomes like charge transport to microstructures such as platelets and spherulites ultimately requires structural characterization

at multiple scales and proper correlation of the obtained characteristics.

Unfortunately, fully characterizing organic thin film microstructure and its formation is challenging precisely because it involves multiple characteristic scales, which would invoke multiple different techniques that need to be referenced to one another. Microstructural characterization of complex polycrystalline structures can involve techniques that span infrared to X-ray photons or employ scanning probe or electron capabilities [78, 79]. For example, polarized optical microscopy (POM), as shown in Figure 2.1a-b, offers qualitative visualization of crystalline films on the tens to hundreds of micron length scales. Viewing films through crossed polarizers provides indirect orientation information through variations in intensity hues and is an accessible and non-destructive characterization technique. In addition to capturing static images of films, POM can also record the evolution of structure in films at the macroscopic level, for example, *in situ* during film processing.

Polarized scanning transmission X-ray microscopy (STXM) generates elemental composition maps based on the transmission of the focused polarized X-ray beam through a rastered sample. Generally, STXM offers sub-micron to tens of nanometer resolution, where the X-ray probe size is on average 50-100 nm but can achieve down to 25 nm resolution depending on the zone plate used [45]. By imaging the same region in a crystalline film with different X-ray polarizations, it is possible to also acquire a local crystal orientation map with polarized STXM. Polarized STXM provides nanoscale morphological characterization that is also sensitive to the electronic and chemical structure of the material [80–82].

Conventional transmission electron microscopy (TEM) produces an image on a pixelated detector with an electron beam that passes through the sample with potentially higher resolution than optical microscopy and STXM. An electron diffraction pattern acquired from a region within the sample elucidates crystal structure [83]. Four-dimensional scanning TEM (4D-STEM) builds upon standard TEM by measuring a full diffraction pattern at each point in a sample using a scanning electron probe that is 0.5 - 50 nm in diameter. By comparing each diffraction pattern to a library of templates, the orientation of a crystalline grain can be calculated and mapped onto its respective field of view [54]. 4D-STEM quantitatively uncovers defects or anomalies in crystal structure packing and orientation [48, 84].

Despite the complementary scales and value of accessing information from each of these forms of imaging, combining the information self-consistently has remained challenging. The most significant barriers revolve around correlating sample measurements across modalities and developing the resultant data analysis workflow, which includes co-registering measurements, relating different spatial regions across measurements, and processing data across different dimensions [28]. Organic films, as relatively soft materials, are particularly susceptible to damage or irreversible chemical change and require a non-trivial investment in optimizing acquisition parameters to avoid sample destruction, especially with X-ray and electron microscopies. Furthermore, each technique typically requires different substrates or film thicknesses that must be accommodated self-consistently in order to correlate each form of image acquired to the others.

In spite of these challenges, we use multimodal characterization spanning micron and nanometer length scales to identify a hybrid microstructure in rubrene thin films, where large

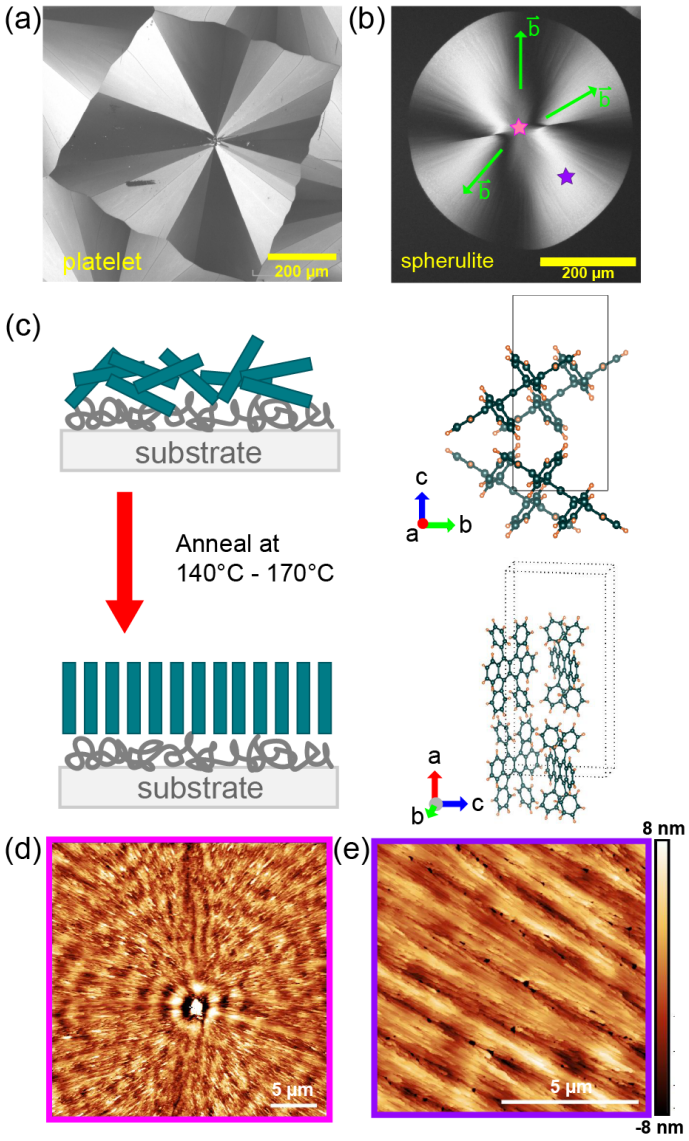

Figure 2.1: Crystallized rubrene thin film characterization. Polarized optical microscope images of a representative crystalline rubrene (a) platelet and (b) spherulite on glass/ITO substrates. (c) Illustration of the annealing process for rubrene thin films. A 40 nm film of amorphous rubrene (represented by blue rectangles) on top of 5 nm of TPTPA (gray underlayer atop substrate) is annealed with setpoints in the 140°C 170°C range to yield crystalline rubrene, as depicted by the upright blue rectangles. The orthorhombic crystal structure is shown from the in-plane perspective (c- and b-axes) and out-of-plane perspective (a-axis normal to the film). The green arrows shown in (b) represent the crystalline growth direction of orthorhombic rubrene. Representative AFM images for the surface morphology around (d) the center of a spherulite indicated by the pink star in (b) and (e) the body of a spherulite indicated by the purple star in (b).

crystalline platelet domains radially transition into a spherulite morphology. In Sections 2.3 and 2.4, we use X-ray and electron microscopies to image and quantify the disappearance of orientational discontinuities between platelet domains as the microstructure transitions into a spherulite morphology at two different scales. We also use polarized optical microscopy to capture the in situ crystallization process, and extract the associated kinetics, which enables us to estimate the temperature at which this transition occurs (Sections 2.5-2.5.1). Our multimodal imaging approach relies on a robust thin film processing protocol, using POM for initial characterization, and optimal, minimally destructive electron and X-ray acquisition parameters. For example, recent efforts to determine such parameters has made it possible to characterize organic films in detail with 4D-STEM through sample cooling and minimizing beam dose [48, 84]. Multimodal characterization enables us to attribute the observed hybrid microstructure to sufficiently slow substrate thermalization that allows for crystallization to proceed through multiple morphologies. Our observations suggest that finely controlling microstructure also calls for advanced temperature control protocols.

2.2 Preparation and initial characterization of rubrene thin films

2.2.1 Materials and Fabrication

Before discussing our correlative multimodal imaging of crystallized rubrene thin films via polarized STXM, 4D-STEM, and POM, we describe their preparation and pre-characterization. The materials studied in this work include rubrene and tris(4-(5-phenylthiophen-2-yl)phenyl)-amine (TPTPA), both of which were sourced from Lumtec. Rubrene was purified via thermal gradient sublimation prior to use. All glass/ITO substrates were cleaned successively by sonication in deionized water with Extran soap in a 6:1 ratio, deionized water, acetone, and isopropanol followed by an oxygen plasma treatment. The silicon nitride (SiN) free-standing membrane substrates were cleaned only by an oxygen plasma treatment before use. Samples were deposited using thermal evaporation with a base pressure of $\sim 10^{-7}$ Torr. To form rubrene films 40 nm of rubrene was deposited after depositing 5 nm of TPTPA. Amorphous samples are kept in a nitrogen-filled glovebox where they are also annealed on a pre-heated hotplate to crystallize rubrene as shown in Figure 2.1c (with the exception of the in situ optical experiments described below). To target spherulite growth, films on glass substrates coated with indium tin oxide (ITO) were annealed at 170°C for 10 s - 2 min, depending on the extent of crystallization desired, while those deposited on SiN windows on 200 μm Si frames (Norcada) were annealed at 170°C for 5 s - 1 min, depending on the extent of crystallization desired and on the thickness of the SiN. Control films annealed to form predominantly platelets were annealed at 140°C for 1 min on glass/ITO or 45 s - 5 min on the SiN substrates. We use SiN substrates for electron and X-ray transparency in polarized STXM and 4D-STEM measurements, while glass substrates coated with indium tin oxide (ITO) are used in the in situ optical experiments for ease of encapsulation in order

to anneal outside of the glovebox. This robust rubrene thin film processing protocol enables consistent crystallization across a variety of substrates, and previous research has determined that substrate choice does not impact rubrene crystallization on account of the TPTPA underlayer [22, 85]. Crystallizing rubrene directly atop of SiN substrates is especially helpful for TEM measurements since it bypasses the need to transfer the crystalline film between unlike substrates.

2.2.2 Optical, Scanning Probe, and X-ray Scattering Characterization

For pre-characterization, we use POM to confirm crystallization of thin films and map out areas of interest for STXM and 4D-STEM measurements. Its hundreds-of-micron-scale field-of-view enables quick identification of various regions of the spherulites and their locations relative to one another for the nano- and sub-nanoscale measurements. Under optical linear crossed-polarizers, spherulites exhibit smoothly varying azimuthal changes in contrast and a signature Maltese cross pattern (Figure 2.1b), representative of the correlation between the nanocrystallite b-axis and the spherulite radial vector. In comparison, platelets exhibit uniform optical contrast under crossed-polarizers with stark grain boundaries, denoting single-crystalline domains.

Grazing incidence wide-angle X-ray scattering (Figure 2.2) confirms an orthorhombic crystal structure (Figure 2.1c), which is the electronically relevant crystal structure for device applications, given that the π-stacking along the b-axis facilitates charge transport. Scattering data is shown as a function of q_r and q_z, where $\sqrt{q_\mathrm{y}^2 + q_\mathrm{x}^2} = q_\mathrm{r}$. After correction for instrumental and geometric broadening, we find the values of the corresponding lattice parameters: $a = 28$ Å, $b = 7.1$ Å, $c = 15$ Å. A Scherrer analysis suggests the grains are elongated along the b-axis (Table 2.1).

To find the crystalline coherence length (L_c) of the crystalline rubrene films, we use the Scherrer equation:

$$L_\mathrm{c} = \frac{2\pi K}{\Delta q}, \tag{2.1}$$

where L_c is the crystalline coherence length, K is a dimensionless numerical factor that we set as 0.9, and Δq is the full width at half maximum (FWHM) of the peak. To find Δq that is intrinsic to the sample and not convoluted with instrumental (Δq_exp) and geometric (substrate, Δq_geo) broadening effects, we approximate that

$$\Delta q = \sqrt{\Delta q_\mathrm{exp}^2 - \Delta q_\mathrm{geo}^2}. \tag{2.2}$$

Δq_exp is found by taking a linecut of the peak of scattering intensity I as a function of q and fitting it to the following Gaussian form:

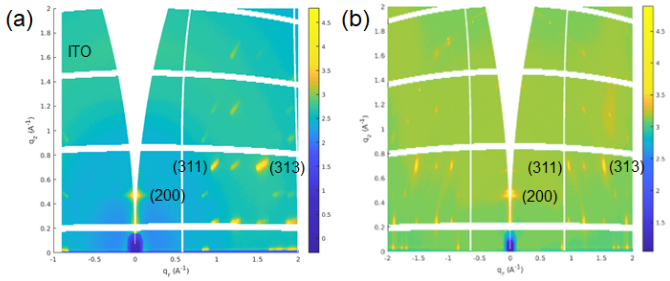

Figure 2.2: GIWAXS patterns of crystalline rubrene thin films. We observed diffraction patterns consistent with an orthorhombic crystal structure [85, 86] for rubrene thin films annealed at 170°C onto both a (a) glass/ITO substrate and (b) 10 nm-thick SiN substrate. All grazing incidence wide-angle X-ray scattering measurements were performed at the 7.3.3 beamline at the Advanced Light Source at the Lawrence Berkeley National Laboratory, California at 10 keV and grazing incidence angles of 0.14°, 0.15°, and 2.5°. Data collected with Brendan Folie and Alex Liebman-Peléz and analysis completed by Alex.

Crystal Axes	a	b	c
L_c Coherence Length (nm)	44.0	74.9	48.5

Table 2.1: Calculated coherence lengths for the crystal axes of orthorhombic rubrene.

$$I(q) = ae\left(\frac{-(x-x_0)^2}{c^2}\right) \tag{2.3}$$

where $c^2 = 2\sigma^2$, which corresponds with the FWHM of the peak. Finally, $\Delta q_{\text{exp}} = 2\sqrt{\ln(2)}c$, which follows from the definition of the Gaussian FWHM: $2\sqrt{2\ln(2)}\sigma$. The expected geometrical broadening effect on the peak is found as

$$\Delta 2\theta_{\text{B}} = \frac{w\sin(2\theta_{\text{B}})}{\text{sample-to-detector distance}} \tag{2.4}$$

where the Bragg peak θ_{B} can be converted into reciprocal space to find Δq_{geo} by the relationship: $\theta_{\text{B}} = \sin^{-1}\frac{q_{\text{geo}}\lambda}{4\pi}$. w is the beam footprint that comes from the length of the substrate in the beam path and is approximated as 3 mm for all peak calculations. Using this workflow, we are able to calculate the coherence lengths for the three orthorhombic crystal axes in rubrene shown in Table 2.1. As described in the introduction and Figure 2.1, the b-axis corresponds with the higher crystallization rate and also the crystal growth front [22, 85], resulting in the anisotropic crystalline grains.

AFM imaging was performed in tapping mode with an Asylum MFP-3D with TAP 150 Al silicon AFM probes (Ted Pella, Inc.). The scans were collected with a 583 mV setpoint and a 2.5-2.6 V amplitude. Figure 2.1d has a 29.2 nm per pixel resolution with a 0.75 Hz

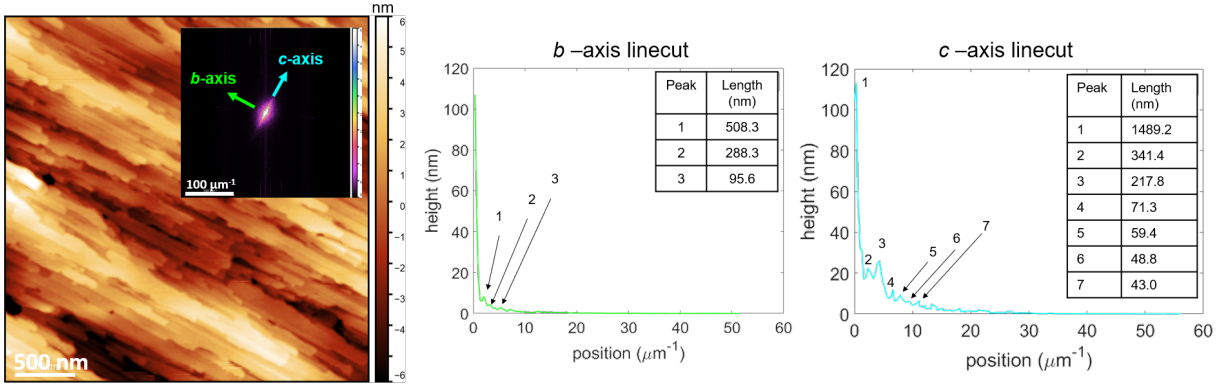

Figure 2.3: FFT analysis of rubrene spherulite AFM image. AFM image for the surface morphology of the body of a spherulite and the corresponding FFT of the AFM image as the inset. Linecuts along the c-axis and b-axis are plotted in blue and green, respectively, with labeled peaks accompanied by their real-space length.

scan rate, and Figure 2.1e has a 19.6 nm per pixel resolution with a 0.5 Hz scan rate. The sample imaged by AFM was annealed for 5 s at 170°C on 10 nm of SiN (NT050Z). Atomic force microscopy (AFM) images show nanoscale crystalline rods that have grown radially outward from the nucleus (Figure 2.1d) at the location indicated by the pink star in Figure 2.1b. The rod-like shape is consistent with the higher crystallization rate along the b-axis and the Scherrer analysis [85]. Figure 2.1e shows similarly aligned rods further away from the nucleus at the location of the purple star in Figure 2.1b.

Given the periodicity of the crystalline rods in a spherulite, their sizes and orientation can also be estimated from AFM images with a 2D-Fast Fourier Transform (FFT) process using Gwyddion. A higher-resolution scan of the spherulite body is shown in Figure 2.3, and the FFT of the image is shown in the inset. Linecuts were taken along the longitudinal and transverse axes of the 2D-FFT, which correspond to the c-axis and b-axis, respectively. By fitting the linecuts to a Lorentzian, the reciprocal-space positions of the peaks were identified and used to calculate the lengths in real space by taking the spatial difference between two peaks and calculating the inverse of the difference. The resulting real space values observed in the linecuts are listed in the tables in Figure 2.3. Along the c-axis, we see that there are large periodic structures ("spokes") composed of crystalline rods that consist of crystallites ∼43-48 nm. A transverse cut of the 2D-FFT suggests that the crystallite size along the b-axis (∼96 nm) is also visible. Both of these estimates are similar to the crystallite sizes calculated from the Scherrer analysis, which may indicate that crystalline grains can be observed via AFM. Fourier transforms of AFM images may corroborate X-ray scattering analyses of crystalline grain sizes, but the information is highly dependent on the heterogeneity of the periodic features and scan area which impact the FFT analysis.

Brendan Folie, a previous group member, commented on the appearance of the spherulite growth front in his thesis [27] as a wave-like pattern that culminated in a tall edge and trough

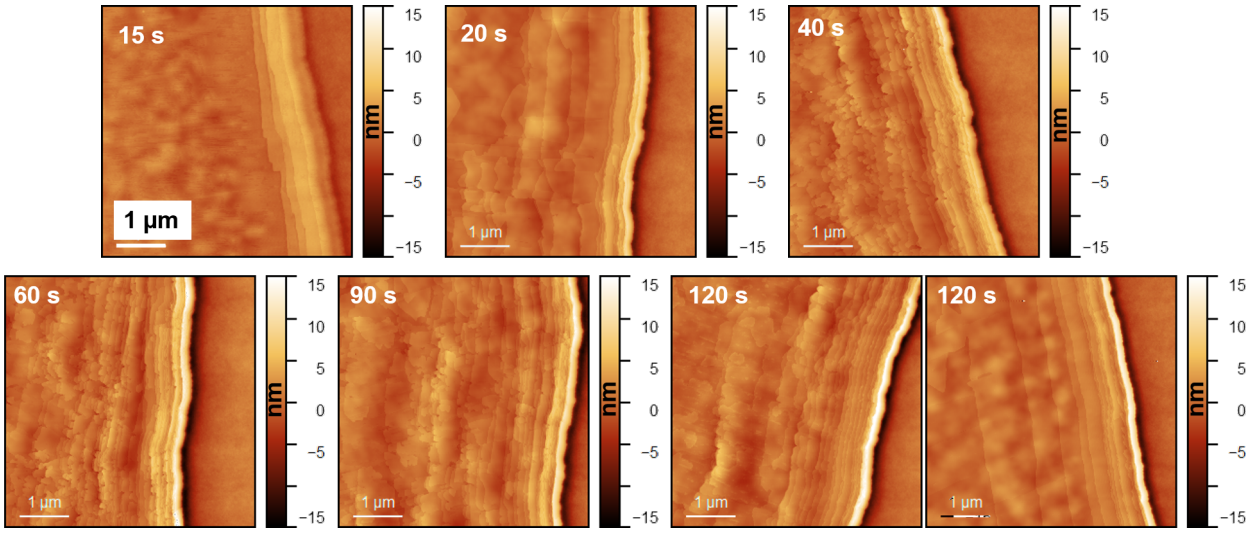

Figure 2.4: AFM images of spherulite growth fronts at various annealing times. Different films of 40 nm rubrene on glass/ITO substrates were annealed at 170° for time durations ranging from 15 s - 120 s. Scale bar for all AFM images is 1 μm.

that increased in height and depth, respectively, with annealing time. In Figure 2.4, we observe this description in a series of close-up AFM images of the growth front as a function of annealing time. With longer annealing times, the waves or layers of crystalline rubrene that accumulate at the growth front increase, and the edge of the growth front builds up in height as well. The tall edge at the growth front appears reminiscent of a surface transport model of molecules, where the surface molecules are more mobile and lead to the upward growth of the crystal, which also circumvents slow growth in the bulk [87]. To confirm the mechanism of rubrene crystallization and learn more about spherulite growth, however, more sophisticated *in situ* crystallization measurements will be needed.

We present other AFM image observations on rubrene spherulite growth fronts in Figure 2.5. We observe that the growth front perimeter can adopt a "scallop" pattern as shown in two different spherulite growth fronts (Figure 2.5a-b)). Closeups of the growth front (Figure 2.5c-d) also illustrate that the formation of the nanocrystalline rods that we characterize by Scherrer analysis (Figure 2.1) in the body of a spherulite do not form immediately at the growth front.

To expand on the nanoscale information that AFM provides us, we also use infrared scattering scanning nearfield optical microscopy (IR *s*-SNOM) to probe the growth front to determine whether a signal could be distinguished between amorphous and crystalline rubrene [88]. Four weak vibrational modes were identified at 780 cm^{-1} and 1026 cm^{-1}, which correspond to the out-of-plane C-H stretching mode, and at 1392 cm^{-1} and 1490 cm^{-1} which correspond to the skeletal vibration of the tetracene backbone [62] (Figure 2.6). Between crystalline and amorphous rubrene, the skeletal ring vibrations decreased in strength to the detection limit of the IR *s*-SNOM set-up over a distance of 700 nm (Figure 2.7). This

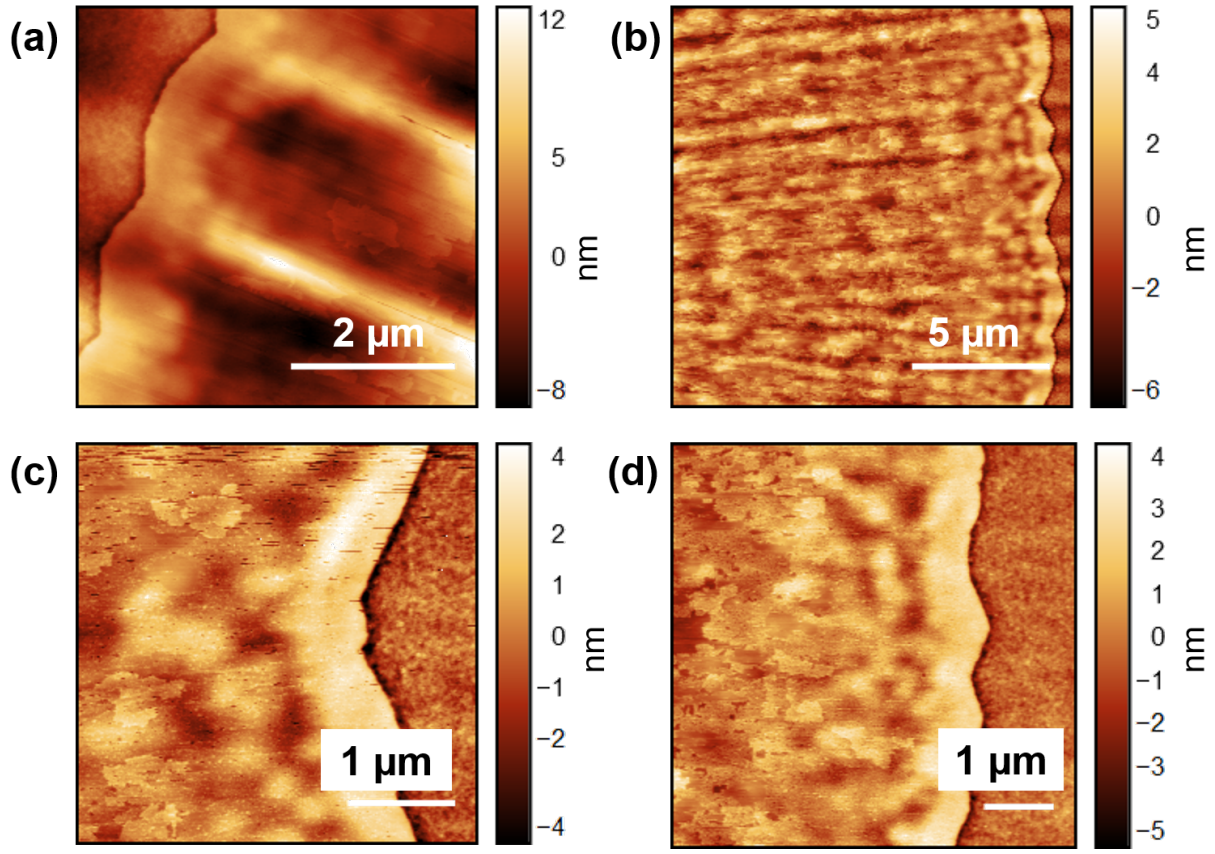

Figure 2.5: AFM images of different spherulite growth fronts on SiN substrate. (a) Close-up for one rubrene spherulite growth front exhibiting scalloped growth front pattern. (b) Large field-of-view of second spherulite growth front where (c) and (d) are close-ups of this growth front.

suggests a change in ordering or orientation across this transition. In the same region the gradual disorder associated with this transition, as concluded from the increased spread in vibrational frequencies (Figure 2.7e), also increased. This suggests a lower limit of 700 nm for the width of crystalline growth front.

2.3 Polarized STXM measurements reveal a hybrid microstructure

We begin describing our multimodal imaging of annealed rubrene thin films by focusing on polarized STXM with varying resolution and field-of-view. All X-ray microscopy measurements were performed at the 11.0.2.2 beamline at the Advanced Light Source at the Lawrence Berkeley National Laboratory, California. Figure 2.9a-b were annealed at 170°C for 1 min on a SiN window with an area of 1.5 × 1.5 mm^2 and 200 nm in thickness that is

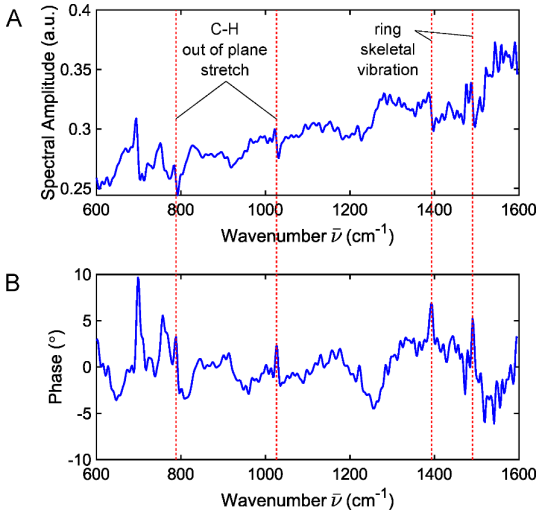

Figure 2.6: Far-infrared synchrotron infrared nanospectroscopy (FIR-SINS) [89] amplitude and phase spectrum of rubrene thin film on glass/ITO substrate. FIR-SINS measurements were conducted at the 2.4 beamline at the Advanced Light Source at the Lawrence Berkeley National Laboratory, California. Data collection and analysis conducted by Dr. Omar Khatib at CU Boulder.

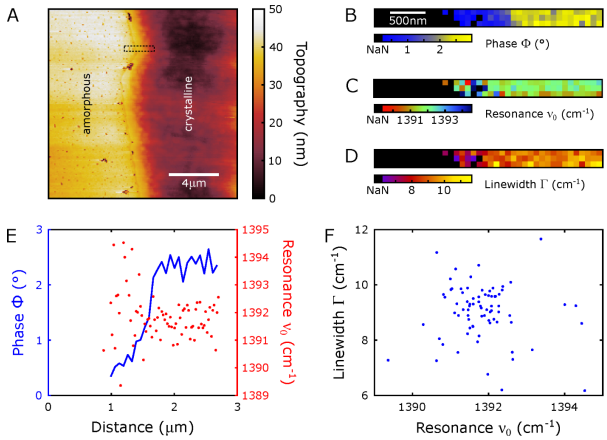

Figure 2.7: IR *s*-SNOM measurements for the growth front of crystalline rubrene thin films annealed at 170°C on 10 nm SiN membranes on Si frames back-coated with gold. Measurements were conducted with a scattering scanning near-field optical microscope (nanoIR2-s prototype, Anasys Instruments/ Bruker) using a broadband infrared laser (FLINT, Light Conversion; Levante, APE GmbH; HarmoniXX, APE GmbH). Hyperspectral images (b)-(d) of the growth front location highlighted in the AFM image (a) accompanied by the vibrational frequencies (e). Data collection and analysis conducted by Sven Dönges at CU Boulder.

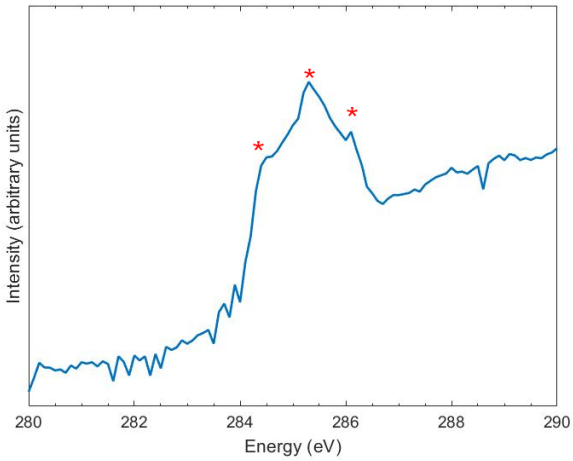

Figure 2.8: STXM NEXAFS spectrum. We center the NEXAFS spectrum of a spherulite rubrene film around 285 eV to resolve the energies that most strongly correspond with linear dichroism. We identify the relevant energies as 284.5, 285.3, and 286.1 eV (red stars). Due to time constraints, we only used 284.5 eV to image samples.

mounted on a 5 × 5 mm^2 Si frame with 200 μm thickness (NX5150D). Control films were annealed at 140°C for 5 min on a SiN window with an area of 1 × 1 mm^2 and a 100 nm thickness (NX5100C). The film used to generate the NEXAFS spectrum (Figure 2.8) was annealed at 170°C for 5 s on a SiN window with an area of 2 × 2 mm^2 and 200 nm thickness (NX5200D). Samples were mounted onto an aluminum plate inside of the sample chamber that is evacuated to about 30 mTorr and refilled with 200 Torr of helium. We collected a NEXAFS spectrum (Figure 2.8) and identified energies close to the carbon K-edge with linear dichroic contrast at 284.5, 285.3, and 286.1 eV. Each image was collected at both vertical and horizontal polarizations at 284.5 eV because of its strong dichroic contrast. Figure 2.9a shows a 300 μm × 300 μm polarized STXM image of the center of an apparent spherulite. Image viewing and analysis was facilitated by the IDL program aXis2000 from the Hitchcock Group at McMaster University and the STXM Data Analysis Matlab script collection from T.R. Henn (Physikalisches Institut, Germany) and R.C. Moffet (Lawrence Berkeley National Laboratory, USA). The image shown is a ratio of the images collected with vertical and horizontal polarizations to enhance the intensity contrast. The greyscale pixel intensity is a proxy for crystal orientation, where white pixels correspond to crystallites oriented parallel to the X-ray polarization, and black pixels correspond with crystallites oriented orthogonal to it.

We focus on a recurring motif characterized by an abrupt azimuthal change in transmission contrast observed next to the nucleus that gradually smooths out at larger radii. In a perfect spherulite the local crystal b-axis orientation would match that of a radial vector originating at the nucleus to generate a smoothly varying orientation distribution, as is apparent in Figure 2.1b. In polarized STXM, this would translate into smooth az-

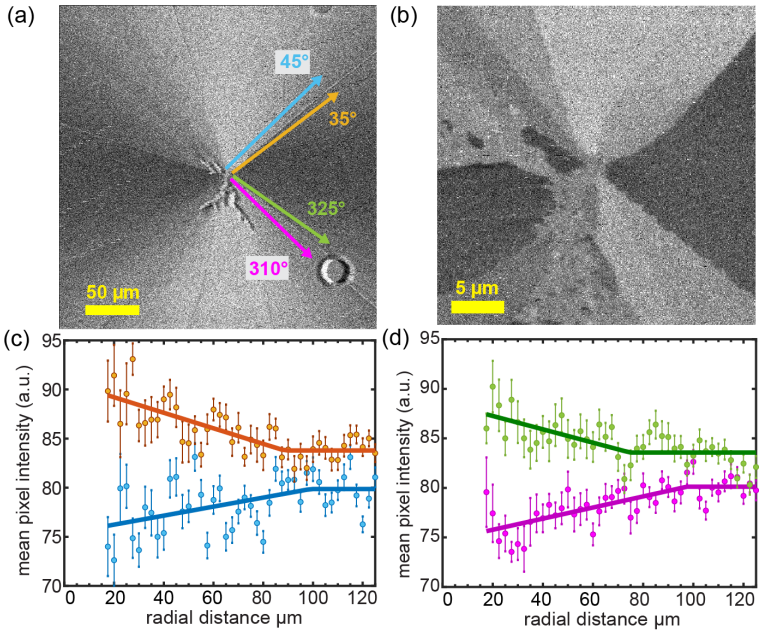

Figure 2.9: STXM imaging and analysis. (a) Grayscale ratiometric STXM image of a spherulite annealed on a 200 nm SiN window at 170°C for 1 min at a large field-of-view with 450 nm pixel resolution. (b) A separate ratiometric STXM image of the same spherulite with 60 nm pixel resolution focused on the nucleus and emanating single-crystalline domains. (c) and (d) Profiles of mean pixel intensity as a function of distance from the nucleus following two pairs of radial vectors, each surrounding a given orientational discontinuity. Colors of the intensity profiles correspond to the colored radial vectors in (a). Mean pixel intensities are shown as circles with their corresponding standard deviations shown as error bars, and the piecewise fit to the profiles are shown as solid lines. The fitting parameters are shared in Table 2.2.

imuthal changes in the greyscale pixel intensity. Instead, near the nucleus we observe sharp azimuthal changes in X-ray transmission between more uniform patches of transmission. Another higher-resolution ratiometric image centered at the same spherulite nucleus (Figure 2.9b) clearly demonstrates the sharp change in greyscale surrounding a nucleus, also suggesting platelet-like domains. With the larger field of view in Figure 2.9a, we observe these sharp changes disappear at larger radii. Consider for example the behavior as a function of distance from the nucleus at ∼40°. Tracing the orange and blue pair of radial vectors on each side (35° and 45°, respectively), the greyscale values gradually converge to those expected for a spherulite. Another example of this observation is highlighted by the pink and green pair of radial vectors at 310° and 325°.

To quantify this behavior, we analyze in Figure 2.9c-d the radial transmission profiles of horizontally polarized images by considering the X-ray transmission as a function of radial distance from the nucleus at the azimuthal angles on opposite sides of the two sharp changes in polarized X-ray transmission shown in Figure 2.9a. We first identify the pixel coordinates

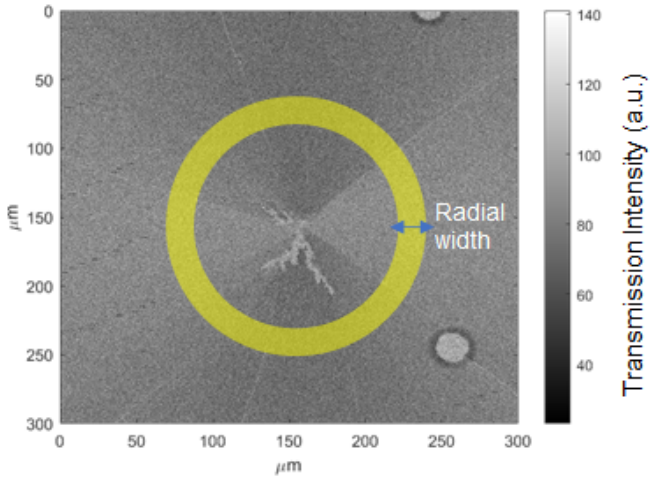

Figure 2.10: Example of radial width for STXM image radial profile analysis. A horizontally polarized STXM image is shown with a yellow circle overlaid as an example of the user-defined radial width which dictates the grayscale pixels that will be involved in the calculation of the average pixel intensity.

of $r = 0$ μm corresponding with the nucleus with Fiji [90]. To calculate the average pixel intensity at a given radius, we collect pixel intensities that fall within a user-defined radial width (Figure 2.10) and bin them in increments of 1° from 1° to 360°. Data shown in Figures 2.9c-d use a radial width of 4.5 μm which corresponds with ∼10 pixels per bin. The average pixel intensity and corresponding standard deviation are calculated for each bin and represent one average intensity datapoint at a single radius. This protocol is repeated to plot average pixel intensity as a function of radius from the center of the spherulite and outward from it. Due to poor signal-to-noise close to the nucleus, we start plotting the average pixel intensity at 20 μm. Code is provided in Appendix A.

In both cases on both sides of the respective abrupt changes, we observe that the transmission evolves gradually from its greyscale value near the nucleus at small radii to a value beyond which it stabilizes within a certain radial range away from the nucleus. Next, we fit these radial profiles to a piecewise function to capture the approximate distance (X_1) from the nucleus at which the greyscale value stabilizes (Y_1):

$$\text{Intensity}(Y) = \begin{cases} \frac{Y_1 - Y_0}{X_1} x + \left(Y_1 - \frac{Y_1 - Y_0}{X_1} X_1 \right), & x < X_1 \\ Y_1, & x \geq X_1 \end{cases} \tag{2.5}$$

where Y_0 is the initial greyscale value. For example, in Figure 2.9c, the greyscale values that correspond to the 35° radial vector (orange) begin at ∼90 at 20 μm from the nucleus and drop to ∼84 about 80 μm from the nucleus, remaining at that value thereafter. To provide more physical context for this observation, we convert the greyscale value of transmission to

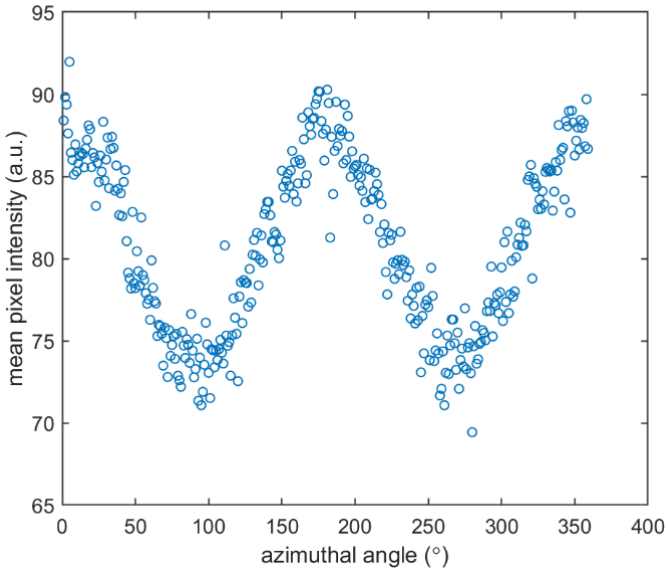

Figure 2.11: Representative azimuthal transmission intensity radial profile of spherulite at 100 μm away from the nucleus. The maximum ($I_{\max}$) and minimum ($I_{\min}$) intensities are identified in this profile to use in the sinusoidal expression discussed in the main text: $I = (I_{\max} - I_{\min}\sin^2(\theta_{\text{crystal}} + \phi) + I_{\min}$. For the final calculation of crystal orientation in Table 2.2, we use an azimuthal transmission intensity radial profile 100 μm from the nucleus.

crystal b-axis orientation through the sinusoidal relationship expected for smoothly varying intensity over 360°: $I = (I_{\max} - I_{\min})\sin^2(\theta_{\text{crystal}} + \phi) + I_{\min}$ (Figure 2.11).

Therefore, in terms of local crystal b-axis orientation, in this example following the 35° radial vector, we find that beginning at the nucleus, the local b-axis orientation gradually and continually changes until it stabilizes at 31° ± 4° at 80 μm. A similar behavior is observed at the 45° radial vector (blue) on the opposite side of the abrupt change in transmission: the initial b-axis orientation is most disparate at smaller radii (∼75° at 20 μm) and gradually changes to achieve a value of ∼48° ± 6° around 100 μm, which is consistent with a smaller difference in orientation relative to the value at 45°. Related trends about 317.5° are plotted in green and magenta in Figure 2.9d, and all of the data are summarized in Table 2.2.

The plots of crystallite orientation versus distance from the nucleus obtained on opposite sides of the sharp change in transmission contrast suggest that abrupt transmission changes over small angular ranges correspond to an orientational discontinuity. The crystallites on either side of the discontinuity have uniform transmission contrast over a larger azimuthal range and orient independently of the direction of the radial vector. The onset radius at which the local crystallite orientation near a discontinuity begins to align with the radial vector ranges between 75 - 99 μm (Table 2.2). Although an improved signal-to-noise ratio in the image might enhance visualization of additional discontinuities possibly present in the spherulite, the two identified in Figure 2.9a and additional examples in Figure 2.12 suggest

$\theta_{azimuthal}$	Onset radius of final $\theta_{crystal}$	Final crystal orientation θ	Corresponding T with upper and lower bound (°C)
35°	80 ± 16	31 ± 4	134 (125, 138)
45°	99 ± 49	48 ± 6	136 (122, 146)
310°	98 ± 24	313 ± 4	136 (127, 142)
325°	75 ± 22	327 ± 33	133 (123, 138)

Table 2.2: Determination of the onset radius for the final crystal orientation of the platelet-to-spherulite transition and the corresponding temperature.

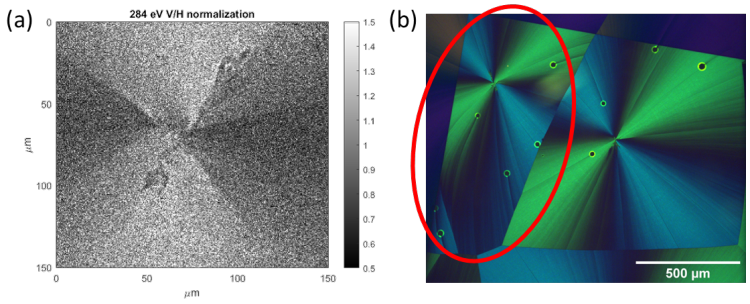

Figure 2.12: Polarized STXM image and corresponding POM image of another spherulite. (a) A ratiometric image of a spherulite annealed on a 200 nm SiN window at 170°C for 1 minute at a large field-of-view with 500 nm pixel resolution. This crystalline structure borders the spherulite discussed in Figure 2.9 as shown in the (b) POM image with the red circle of the second spherulite.

a consistent and reproducible trend. Similar to Figure 2.9b, we observe sharp azimuthal changes in X-ray transmission surrounding the nucleus suggesting the start of an orientational discontinuity even though the azimuthal changes at larger distance from the nucleus are smooth and continuous in POM. Although lower signal-to-noise ratio and coarser spatial resolution in Figure 2.12(a) make it impractical to perform a similar analysis to that in Figure 2.9c-d, we anticipate that a similar trend would follow.

2.4 4D-STEM confirms erasure of an orientational discontinuity

We use 4D-scanning transmission electron microscopy (4D-STEM) to obtain higher resolution orientation maps at the disappearance of an orientational discontinuity. 4D-STEM data were acquired using a ThermoFisher Scientific ThemIS transmission electron microscope operated at 300 kV accelerating voltage. During imaging, the samples on 10 nm thick SiN windows were cooled to approximately 90 K by a Gatan 636 cryo holder. The 4D-STEM

datasets were acquired with a probe semiconvergence angle of 0.59 mrad across a grid of 512 $\times$ 512 pixels, with a step size of 15.5 nm between probe positions. For rapid acquisition of large-area maps with minimal sample drift, the microscope was fitted with an IDES Relativity electrostatic subframing system. This system divides the detector frame into multiple subframes and rapidly deflects the diffraction pattern into each frame as the beam steps to different probe positions, allowing multiple diffraction patterns to be acquired per readout of the detector. We acquired datasets with a probe dwell time of 2.24 ms, a 4 $\times$ 4 grid of subframes, and a detector exposure time of 36 ms.

Given that spherulites are hundreds of micrometers in size and 4D-STEM has a limited field-of-view of less than 10 μm $\times$ 10 μm preparatory identification of the apparent spherulites formed on the SiN window was essential. Polarized optical images of the films allow us to identify and characterize regions that represent the general feature of a spherulite, such as the nucleus, the main part of the spherulite body, and the growth front where crystallization was arrested.

We present the POM image of a crystallized rubrene film studied via 4D-STEM with the representative scan area indicated by a red box in Figure 2.13a. The area explored corresponds to a region a distance away from the nucleus of an apparent spherulite. All analysis of the 4D-STEM datasets was performed using py4DSTEM, an open-source Python package [53, 54]. In order to produce the orientation maps (Figure 2.13b), we first use the template cross correlation method to locate the positions of each of the diffraction disks in each diffraction pattern. These Bragg disk locations are then calibrated to remove any elliptical distortion caused by the microscope, artifacts caused by translations of the diffraction pattern, and to correct the pixel size. Using the Automated Crystal Orientation Matching (ACOM) submodule of py4DSTEM, a library of simulated rubrene diffraction peaks was generated using the known orthorhombic crystal structure. As we know the films are primarily oriented with the c-axis normal to the substrate, we only simulate patterns with up to 5° mistilt from this orientation. The ACOM matching algorithm compares each experimental list of Bragg disk locations to the simulations and finds the best match zone axis, along with the in-plane orientation of the crystal.

The abrupt change in greyscale from light to dark observed across two grains at the top of Figure 2.13b marked by the arrow and box corresponds to an abrupt change in crystallite orientation of approximately 45°. This orientational discontinuity gives way at greater distances from the nucleus to more gradual azimuthal changes in local crystal orientation, moving smoothly from light to dark, indicated by the lower red arrow. This indicates that the b-axis crystal orientation continuously adjusts over at least 45° to maintain its orientation along the radial vector of the crystallized structure. We also visualize the relative degrees of misorientation described in the orientation map by compiling the diffraction patterns acquired from each point in the scan into a Bragg vector map (Figure 2.13b red boxes, Figure 2.14). The Bragg vector map associated with the upper box in Figure 2.13b shows an offset of $\sim$45° in two distinct orthorhombic diffraction patterns, reflecting the orientational discontinuity. Further away from the discontinuity (lower box in Figure 2.13b) the Bragg vector map shows a smearing of diffraction patterns, indicating in-plane rotation of

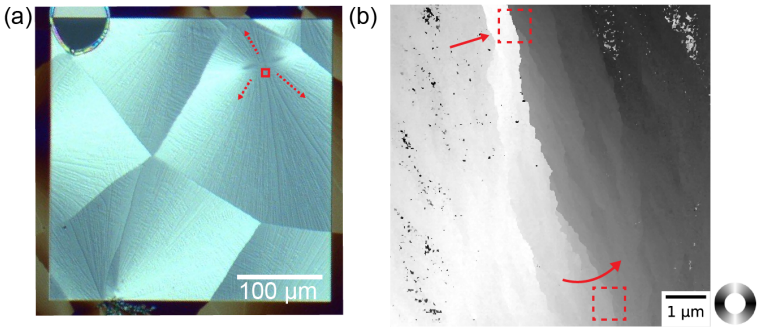

Figure 2.13: Orientational mapping by 4D-STEM. (a) POM image of spherulites within the window region studied with 4D-STEM. The red box (8 x 8 μm) indicates a representative field of view shown in (b), and the red arrows pointing outward from the spherulite nucleus correspond to the local in-plane orthorhombic *b*-axis. (b) In-plane *b*-axis orientation map where the greyscale indicates the orthorhombic *b*-axis orientation, and white corresponds to a vertical *b*-axis orientation. The abrupt change in orientation observed at the top of the map (top arrow and box) is erased at greater distances from the nucleus, seen as a smooth change in orientation along the bottom of the map. The red boxes indicate areas visualized with Bragg vector maps in Figure 2.14. 4D-STEM data collection and analysis conducted by Steven Zeltmann at UC Berkeley.

the *b*-axis crystal orientation even over this small azimuthal range.

2.5 Dynamic polarized optical microscopy measurements to inform on heating and crystallization kinetics

To investigate the formation of the hybrid platelet-spherulite structure observed in STXM and 4D-STEM, we use POM to record a movie of the crystallization by thermally annealing amorphous rubrene films *in situ*. This process also allows us to extract the macroscopic crystallization kinetics of rubrene thin films. Static and dynamic POM measurements were performed with a Nikon Eclipse LV100ND in EPI mode. Images and videos were taken with an Infinity 2 Lumenera camera and Infinity Analyze and Infinity Capture software. For *in situ* annealing measurements, we marked a fiducial on the amorphous rubrene films on glass/ITO substrates to assist in quickly finding the appropriate focal plane. Then the amorphous rubrene films were encapsulated in a nitrogen-filled glovebox, to avoid photo-oxidation, with UV-curing epoxy from EPO-TEK (OG116-31) and using a coverslip (Fisher 12-541-B) cleaned in acetone, 2-propanol, and Millipore water. After encapsulation the sample were removed from the glovebox.

A Thorlabs HT24S metal ceramic heater was placed underneath the Nikon Tu Plan Fluor 10x objective in the microscope and layered with thermally conductive materials to facilitate annealing (Figure 2.15). The ceramic heater temperature was regulated by a Thorlabs

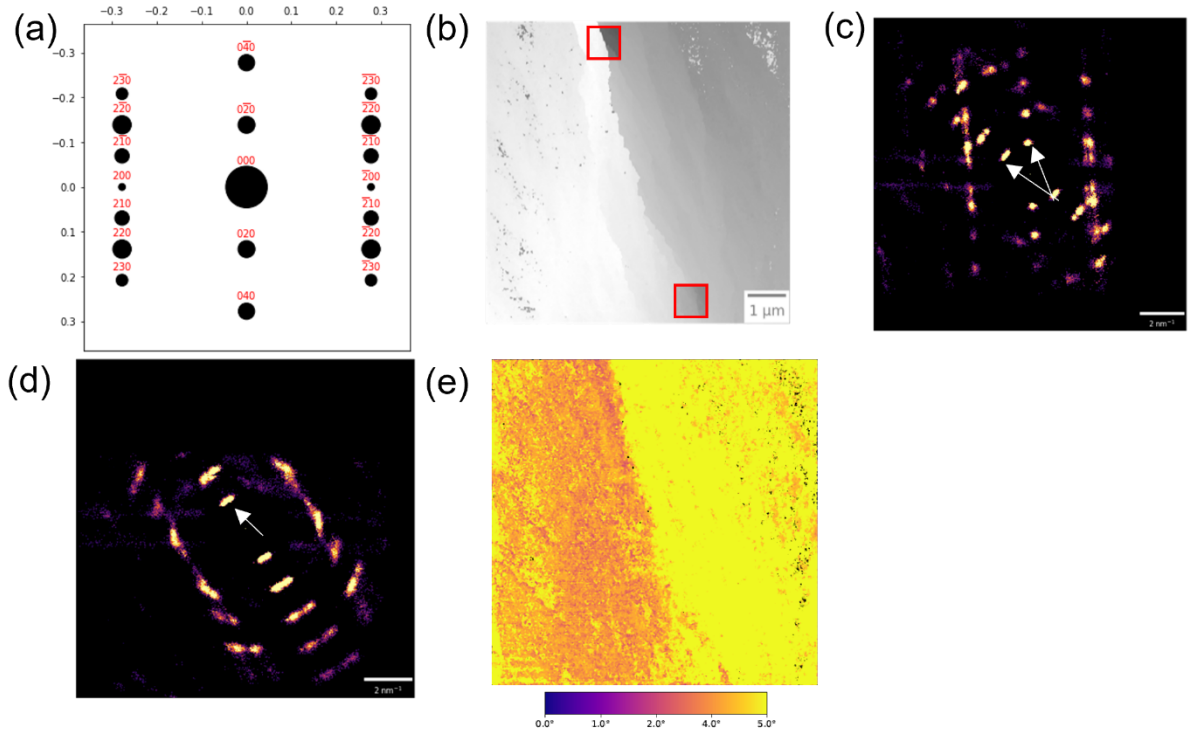

Figure 2.14: 4D-STEM Bragg diffraction patterns. (a) A simulated diffraction pattern for rubrene in the [001] orientation. For a single-crystalline grain, we expect that the diffraction pattern at each point within the scan would be identical and result in a Bragg vector map with no azimuthal smearing. (b) The orientation map from Figure 2.13b indicating the 775 nm x 775 nm areas for which we generate the Bragg vector maps in (c) and (d). (c) This Bragg vector map corresponding to the top region in (b) shows a ∼45° offset of the in-plane orientation between two sharp orthorhombic patterns, as indicated by the arrows. In contrast, the map of the bottom region in (b), depicted in (d), shows an aggregation of patterns whose in-plane orientations are azimuthally smeared, indicating in-plane rotation for the crystal orientation further away from the orientational discontinuity in Figure 2.13b and the crystallization nucleus. (e) The ACOM analysis over the field of view also indicates that the crystallites tilt slightly out of plane around a particular in-plane axis within the same field of view as (b) and Figure 2.13b. 4D-STEM data collection and analysis conducted by Steven Zeltmann at UC Berkeley.

TC200 temperature controller and the auxiliary port was connected to a Thorlabs TH100PT thermistor that monitored the surface temperature of the thermal pad atop of the annealing configuration shown in Figure 2.15. We recorded the microscope settings for this focal plane. The Thorlabs TC200 was set to the desired temperature setpoint. We set the ceramic heater temperature to 190°C to target spherulite growth upon annealing. This temperature ensured the highest fidelity of optical microscope data collection to the glovebox protocol used to fabricate the films used in X-ray and electron microscopies. We allowed the ceramic heater temperature to stabilize for a minimum of two minutes before beginning to record video. The sample was quickly placed onto the annealing setup, and minor adjustments to the focus were made using the fiducial, which had been used to focus the imaging system prior to heating. The crystallization process was imaged at a rate of 11 frames per second, and the sample was removed once the field of view captured in the video was completely crystalline.

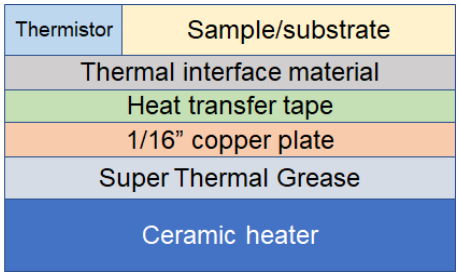

Figure 2.15: Schematic (not drawn to scale) of the thermally conductive materials used to optimize contact between the ceramic heater and rubrene sample for annealing in the *in situ* POM measurements. The materials used were super thermal grease (MG Chemicals Super thermal grease III, 8617), heat transfer tape (McMaster-Carr 1" heat-transfer tape, 7171A22), and a thermal interface material (3M thermal pad).

Movie frames representative of different stages of crystallization are shown in Figure 2.16a. The range of green shades corresponds to crystallized rubrene at different orientations. Most nuclei are too small to observe in optical microscopy, although the spherulite marked by a white arrow at $t = 0$ in Figure 2.16a has a sufficiently large nucleus that it is visible. This larger nucleus is visually consistent with rubrene's triclinic structure due to its distinct visual roughness in optical microscopy. Rubrene's triclinic structure forms at lower temperatures but orthorhombic rubrene can nucleate and crystallize from these triclinic structures [85]. We record crystallization until the spherulites impinge on each other, first seen around 9 s and seen even more prominently at 12 s (Figure 2.16a). In this measurement, the gradual change in color intensity we typically observe under crossed-polarizers is not sufficiently clear to directly discern platelet-like vs. spherulite-like morphology, emphasizing the need for multimodal studies. Signs that indicate spherulite growth rather than platelet growth are the presence of a faint Maltese cross for all observable radii and the lack of any sharp azimuthal changes in green shades that would correspond to an intra-platelet grain boundary.

The primary value of the ability to non-invasively image film crystallization however is that it allows us to track the value of the crystallized radius as a function of time, $R(T, t)$

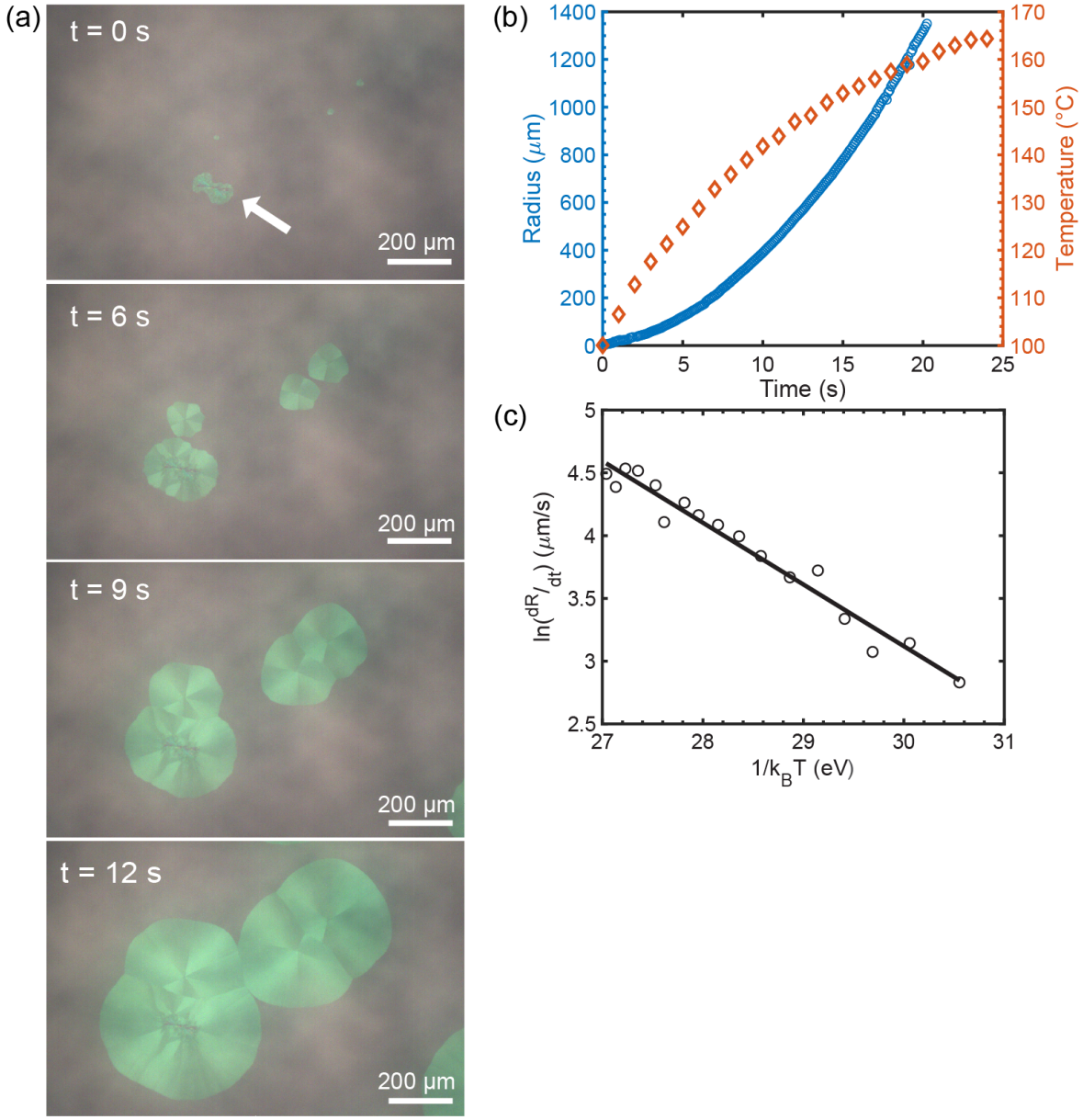

Figure 2.16: *In situ* rubrene crystallization. (a) POM of in situ rubrene crystallization at 0, 6, 9, and 12 s on a glass/ITO substrate. (b) The average radial growth of spherulites observed in POM shown in blue, and the glass/ITO substrate temperature rise to the ceramic heater plate setpoint in orange. (c) The natural log of the spherulite growth rate as a function of the inverse temperature. A line with slope of -0.49 ± 0.02 eV fits the data, indicating Arrhenius behavior for crystallization. Data collection and analysis accomplished with help of Jakhangirkhodja Tulyagankhodjaev.

(Figure 2.16b, blue) and to calculate the growth rate by taking its first derivative $dR/dt(T,t)$ (Figure 2.17). Because it takes a finite time for the substrate to reach the heater plate set

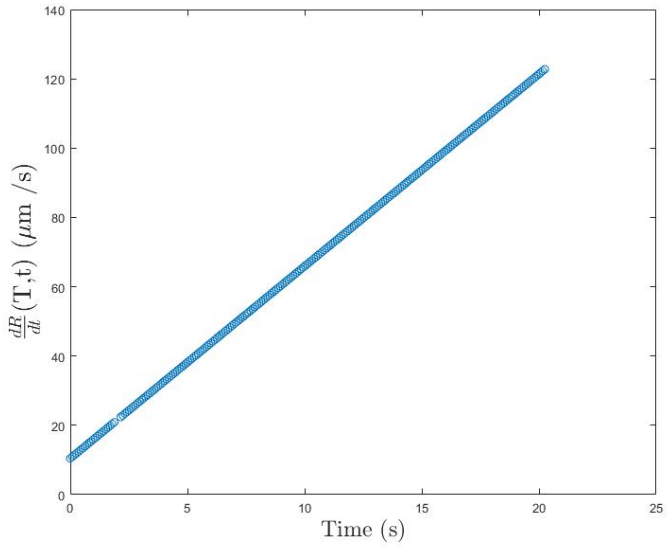

Figure 2.17: Growth rate of spherulites on glass/ITO substrates observed via POM. The spherulite growth rate as a function of time is shown in the figure above and is calculated by taking the derivative of the spherulite radius over time (Figure 2.16a, blue).

point, we are also able to calculate the activation energy for rubrene crystallization.

Tracking the radial growth of spherulites in POM videos was done in Fiji with a custom macro applied to the video in the form of an image stack (Appendix B). The images were binarized based on crystalline and amorphous rubrene distinction with the centroid, perimeter, and area recorded for each circular feature in a given image (Appendix B.1). Then the images were background subtracted for processing in a custom Jupyter notebook to calculate the average radius of the circular features in each frame (Appendix B.2).

We separately measure the glass substrate temperature increase toward the heater set-point (Figure 2.16b, orange) so that it can be combined with dR/dt to obtain the growth rate vs. temperature. Based on the glass substrate temperature measurement, we also infer that crystallization begins at 106°C. By measuring the glass substrate temperature rise, $T(t)$ (Figure 2.16b, orange), each $T(t)$ data point can be related back to the spherulite radius and corresponding growth rate at that same time point. Finally, we plot the natural log of growth rate $\ln(dR/dt)$ against inverse temperature and fit the data to a straight line (Figure 2.16c) to obtain an Arrhenius activation energy of -0.49 $\pm$ 0.02 eV. The straight line indicates that we are observing Arrhenius kinetics. Data for three spherulites captured in the movie are averaged to produce the Arrhenius plot shown in Figure 2.16c.

Although we calculate an activation energy from a different rubrene film thickness of 40 nm, we note our value of 0.49 eV is about three times smaller than previous measurement on glass/ITO substrates [85] and about 40% smaller than that measured on hexamethyldisilazane -functionalized SiO_2 substrates [91]. Thus, despite the challenge of comparing

measurements in different configurations, we hypothesize that the inclusion of the underlayer drives a smaller activation energy for crystallization by acting as a mobile surface that facilitates exploration of the energetic landscape by rubrene molecules to crystallize [22]. The underlayer may also serve as a buffer against additional influence from the underlying substrate. Since we use the same 5 nm TPTPA underlayer for all rubrene films grown on glass/ITO or SiN substrates, we expect that the activation energy is likely similar for the glass and SiN substrates in this work.

Another formalism that is often used to describe spherulite crystallization kinetics, and more broadly phase transition kinetics, is the Avrami equation: $\chi = 1 - \exp(-bt^n)$ where χ is the crystalline volume fraction, n is the Avrami exponent, and b is the temperature-dependent crystallization rate constant with dimensions $(\text{time})^{-n}$ [91, 92]. The Avrami exponent, n, informs on the nucleation mechanism (homogeneous or heterogeneous) and rate, and even the dimensionality of growth. For example, if $n = 4$ then the model reflects homogeneous nucleation and growth in three dimensions, whereas $n = 3$ can represent homogeneous nucleation with growth in 2D, as in a film. Nevertheless, $n = 3$ can also indicate predetermined heterogeneous nucleation and three-dimensional growth [91, 92]. While the Avrami equation could provide further information on the crystallization dynamics of rubrene, it assumes isothermal conditions, which does not hold true in our measurements, given the finite substrate heating time. We carry out the Avrami analysis, however, to illustrate the procedure and results for our situation. Using ImageJ, the movie frames were filtered and adjusted to binarize the images between amorphous and crystalline areas, which appeared as pink and green in the optical microscope, respectively. The area fraction was then calculated in the binarized frames, which served as the measured crystalline area fraction (χ) and is shown in Figure 2.18a as a function of time. The initial fitting of the data to the Avrami equation yields an Avrami exponent of approximately 4, which suggests homogeneous nucleation and 3D growth for this rubrene crystallization protocol. To double check whether the data actually follows Avrami behavior, however, the Avrami exponent is typically found by plotting on a log-log scale and fitting to a straight line. This can be found through a rearrangement of the Avrami equation:

$$\begin{aligned} \chi &= 1 - \exp(-bt^n) \\ 1 - \chi &= \exp -bt^n \\ \ln(1-\chi) &= -bt^n \\ \ln(-\ln(1-\chi)) &= \ln(b) + n\ln(t). \end{aligned}$$

We see that the Avrami exponent is equivalent to the slope of a straight line when plotting $\ln(-\ln(1-\chi))$ as a function of $\ln(t)$, and the crystallization rate constant is the y-intercept. Applying this convention to our *in situ* data, we see that our data does not fall on a straight line on the log-log scale (Figure 2.18b). This is not surprising given the non-isothermal conditions of our measurements and demonstrates that the Avrami equation does not best describe the crystallization behavior for our conditions unless one considers only the later

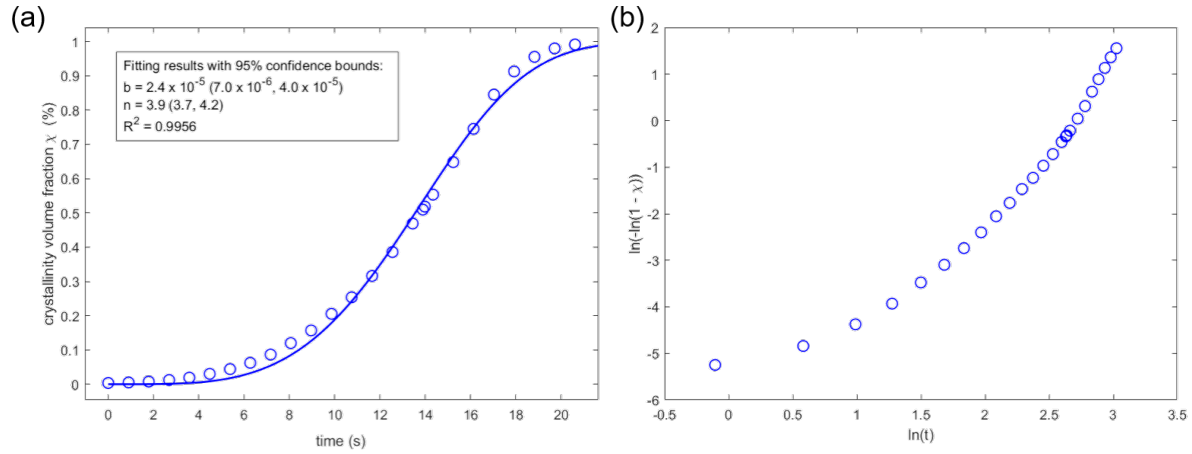

Figure 2.18: Avrami analysis of *in situ* rubrene crystallization. (a) The plot of rubrene crystalline fraction growing as a function of time showing a sigmoidal shape (blue circles) with the Avrami fit (blue curve) overlaid. (b) Plotting the crystalline volume fraction and time on a log-log scale.

times when the temperature has mostly stabilized (e.g., after 14s). For further discussion on quantifying spherulite crystallization, or amorphous-to-crystalline phase transitions, using the Avrami equation, references [92, 93] provide detailed insight into how to carry out measurements and analysis. Consequently, we proceeded to use the Arrhenius behavior information to help us learn more about *in situ* crystallization on SiN substrates.

Estimating *in situ* growth dynamics on SiN windows

Although the temperature of a SiN window is difficult to measure *in situ* while a rubrene film is being annealed for X-ray or electron imaging, we developed a strategy to estimate the temperature at which the larger platelet-like regions transition into a spherulite morphology observed in the polarized STXM and 4D-STEM images. To do so, we combine the Arrhenius kinetics information obtained from the *in situ* POM measurements with an estimate of the SiN substrate thermalization as a function of time. To obtain this thermalization estimate, we measure the temperature rise as a function of time of a 200 μm Si chip after being placed on a 170°C hotplate (Figure 2.19, orange). We expect the temperature rise of the SiN to be similar since spherulites are found to nucleate both on and off the SiN window region (Figures 2.13a, 2.20), and this evidence of uniform SiN heating suggests it is faster than the time required for the heat to propagate through the Si frame. We substitute this substrate temperature data, $T(t)$ into the Arrhenius expression for the crystallization rate on Si, $k_{\mathrm{Si}}[T_{\mathrm{Si}}(t)] = k_0 \exp(-E_{\mathrm{A}}/k_{\mathrm{B}}T(t))$: Here, k_{B} is Boltzmann's constant, and we use the Arrhenius pre-factor k_0 and Arrhenius activation energy (E_{A}) obtained from the fit in Figure 2.16c since these constants should be independent of the substrate on account of the presence of the TPTPA underlayer between the rubrene and either SiN or glass.

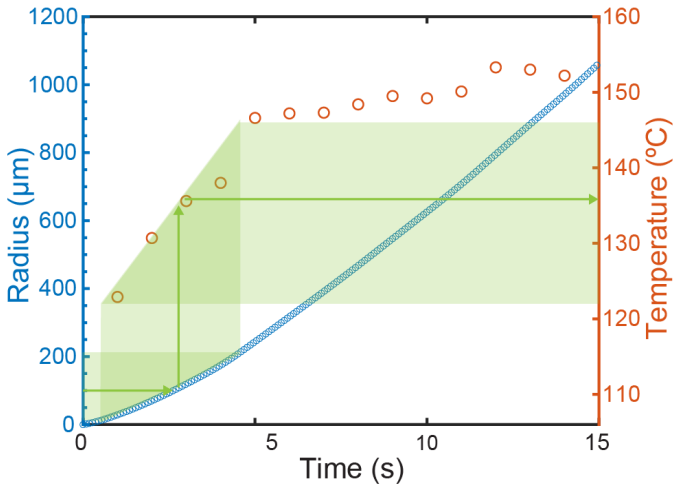

Figure 2.19: Predicted radial growth on a SiN window. The temperature vs. time of a 200 μm Si chip after being placed on a hotplate with a setpoint of 170°C (orange), and the expected spherulite radius on a SiN-on-Si substrate (blue) calculated using the Arrhenius parameters from the *in situ* POM experiment performed on glass/ITO. An example of mapping between radius and temperature is shown for the 45° radial vector from Figure 2.9d where the green bands map out a range of plausible values for the transition temperature.

Next, we integrate the growth rate as a function of time ($k_{\mathrm{Si}}[T_{\mathrm{Si}}(t)]$) to yield the expected crystallization radius as a function of time ($R_{\mathrm{Si}}(t)$) on SiN (Figure 2.19, blue)

$$R_{\mathrm{Si}}(t) = \int dt' \frac{dR_{\mathrm{Si}}(t')}{dt'} = \int dt' k_{\mathrm{Si}}[T_{\mathrm{Si}}(t')]. \tag{2.6}$$

2.5.1 Synthesizing results to understand hybrid microstructure

Finally, we estimate the temperature range over which the platelet-to-spherulite transition occurs. To do so, we relate the onset radii obtained from STXM analysis (Table 2.2) to a corresponding SiN substrate temperature by matching the time window (as shown by guide arrows in Figure 2.19) at which films annealed on SiN are estimated to have the same range of crystallized radii (also Table 2.2). Despite the variation in the onset radius at which the platelet-to-spherulite transition occurs, the corresponding temperature is consistently around 135°C, where due to uncertainty in the onset radius and the timing of the Si chip measurement, this temperature can be specified no more than beyond the range from 122 to 146°C. This estimate seems reasonable based on additional corroboration with the crystallized radii of films annealed on SiN windows for shorter durations (Figure 2.20).

A commonly observed microstructure in our multimodal observations is the presence of a platelet-to-spherulite transition that our analysis suggests is due to finite substrate thermalization time. Hotplate annealing conditions are typically 140°C to crystallize platelet films,

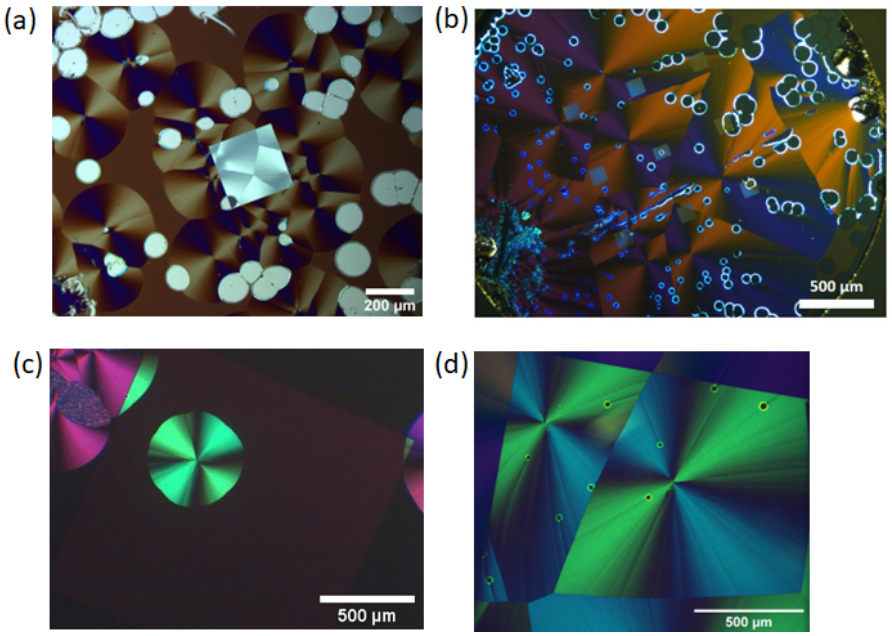

Figure 2.20: Polarized optical microscopy images of 40 nm of rubrene crystallized at 170°C on SiN membranes on Si frames. (a) rubrene annealed for 5 s on 10 nm SiN membrane, (b) rubrene annealed for 15 s on 10 nm SiN membrane, (c) rubrene annealed for 5 s on 200 nm SiN membrane, and (d) rubrene annealed for 1 minute on SiN membrane.

where rubrene molecules locally find their energetic single-crystal minimum through rotation, or 170°C to crystallize spherulites where molecules are not able to rotationally probe a sufficient number of configurations, which leads to polycrystalline branching [22, 25, 26]. Note that these temperatures are lower than the bulk crystallization temperature of 173°C, on account of decreased film thickness and finite surface effects [22, 94, 95]. Due to the finite substrate thermalization time of the film with the hotplate we hypothesize that a sufficient amount of time is first spent at platelet-forming temperatures before spherulite-forming temperatures are attained. The hybrid microstructure is seen in both polarized STXM and 4D-STEM at different scales and in different spherulites annealed for different amounts of time. Notably, the rubrene thin films measured in 4D-STEM were annealed for approximately five seconds due to the extreme 10-nm thinness of the SiN membrane used (Figure 2.20). Thicker SiN membranes such as those used in the STXM measurements (100-200 nm), required longer annealing times, e.g., 1 min., to obtain complete crystalline coverage, though the greater thickness likely serves to delay the onset of crystallization after which the dynamics proceed similarly to those of the thinner membranes. We suspect that the different thicknesses of SiN membranes both spend ∼3 - 4.5 s in the platelet-forming temperature regime based on the Si temperature rise (Figure 2.19, orange). Although as little as 5 s are spent annealing on the hotplate, we propose that when the SiN membrane is taken off it, the substrate is effectively insulated by the surrounding air, so that crystallization may continue

for some time afterward and lead to continuing growth of the spherulite microstructure for films annealed for less than a minute. Based on our observations and calculations, a hybrid microstructure likely occurs somewhat universally despite different annealing times and substrate parameters due to the finite substrate equilibration time taken to achieve the desired annealing temperature.

More broadly, since organic semiconductor molecules are susceptible to polymorphism and multiple morphologies, it is important to both employ and understand the specific processing parameters that produce the desired crystal structure and morphology for optimal device performance. For example, previous research has shown that a high heating rate can bypass the triclinic phase of rubrene to preferentially crystallize orthorhombic platelet domains [94]. Here, we find a hybrid microstructure that is completely orthorhombic but that initially has a high-angle orientational discontinuity that disappears with elevated temperatures. While one might propose that a faster heating rate would circumvent the hybrid microstructure of a platelet transitioning into a spherulite, our observations remind us that achieving a uniform organic film is quite challenging, and a spectrum of morphologies or crystal structures often manifest. The organic molecule identity itself strongly determines the ease of uniformly producing a microstructure. If it is capable of forming both single-crystalline and polycrystalline structures, ideally the single-crystalline domains would form at lower temperatures to avoid complex processing or even modification strategies. Given that organic semiconductors easily form multiple morphologies that impact their resulting functionality in devices, characterizing organic thin films on multiple length scales provides a more complete understanding of heterogeneity in films.

Returning to a main theme of this work, multimodal imaging enables our observation of the hybrid microstructure in annealed rubrene thin films and the probable cause of its formation. As the macroscopic characterization technique, POM underpins our multimodal approach to quickly inspect whether we crystallized platelets or spherulites and to serve as a cross-reference for areas of interest before studying the films with other techniques. We learn about the rich nanoscale surface morphology of the films with AFM. Neither POM nor AFM, however, provides direct quantitative crystallite orientation of the thin films. The quantitative orientation information is instead obtained with polarized STXM and 4D-STEM in complementary ways. Polarized STXM provides micron-to-nanoscale features with variable sizes for fields-of-view from hundreds of microns to nanometers. The variable field-of-view sizes facilitated our ability to capture the disappearance of the orientational discontinuity. We use 4D-STEM to corroborate the polarized STXM images of the orientational discontinuity in the crystalline rubrene structure at high resolution and signal-to-noise ratio. To image these rubrene films using a focused scanning electron beam with 4D-STEM requires cryogenic conditions and recent advances in the TEM community [48]. Optimizing image acquisition parameters in X-ray and electron microscopies is clearly essential since organic films are often susceptible to damage from these radiation sources [34]. Finally, we connected these high-spatial resolution static images with *in situ* dynamic recordings of rubrene crystallization via POM, which is fully non-invasive and allows for in situ dynamical measurements of the annealing process beyond what is possible by examining the final product

of the process. It is only through a multimodal imaging approach that allowed us to probe rubrene thin films on multiple length and time scales, that we were able to learn about how the finite substrate thermalization time leads to a platelet-spherulite hybrid microstructure. Furthermore, relating all observations requires not only cross-referencing across multiple scales but also across different substrates. The underlayer ensures that rubrene crystallization is consistent irrespective of whether we anneal on glass/ITO or SiN, since it ends up being the effective substrate for rubrene in both cases. This processing strategy also eliminates the need to transfer the film between substrates for different measurements. By incorporating a multimodal imaging approach that allowed us to probe rubrene thin films on multiple length scales, we learn about how the finite substrate thermalization time leads to a platelet-spherulite hybrid microstructure.

2.6 Conclusion

In sum, we combined optical, polarized X-ray, and electron microscopies to discover and characterize a hybrid microstructure in organic semiconductor thin films that emerges during thermal annealing. Polarized X-ray and 4D-scanning transmission electron microscopies of the annealed structures both demonstrate an orientational discontinuity emanating from a central nucleus and gradually disappearing toward its circular growth front. *In situ* polarized optical microscopy of the crystallization process reveals Arrhenius crystallization behavior and measurement of substrate thermalization time allows us to map between time, temperature, and crystallization radius to determine the temperature at which the spherulite morphology develops. By combining POM, polarized STXM, and 4D-STEM, we determine that the finite substrate thermalization produces a hybrid microstructure because a non-negligible amount of annealing time is spent at a platelet-forming temperature before proceeding to spherulite crystallization temperatures.

2.6.1 Future directions

In the future, hybrid structures could be designed deliberately to perform multiple functions, balancing high charge transport in platelet regions [22] with good charge transport isotropy in spherulite regions [24]. For example, if processing protocols were developed to maximize platelet domain area and introduce spherulite morphology at the growth front, one could overcome high-angle grain boundaries between separate platelet structures and still leverage the majority-platelet film charge carrier mobility while avoiding trapping. This protocol could be varied to optimize the overall needs of the film. A similar strategy could be used to enhance heterostructures between organic films and halide perovskite of transition metal dichalcogenides to overcome transport deficiencies in each [96–98] or to investigate thermoelectric applications [99].

More generally as multimodal imaging opportunities continue to expand for organic materials such approaches may be used to capture *in situ* crystallization of additional films to

elucidate understanding of spherulite formation or other crystalline microstructures. Multimodal imaging will surely advance to capture atomic and nanoscale *in situ* growth of crystals, which would be especially useful to elucidate spherulite formation. Specifically, for rubrene, the multimodal approach could be further leveraged to understand rubrene's inverted thermal spherulite growth behavior whereby spherulites occur at higher temperatures closer to the melting point.

Incorporating measurements of function, such as transport and electronic dynamics [6, 100], with ultrafast microscopies will yield even further insight into structure-function properties for this hybrid microstructure. We conducted preliminary measurements of rubrene spherulites on glass/ITO substrates with TAM (Figure 2.21) and observed a strong excited state absorption (ESA) feature ∼516 nm and a weaker one at ∼480 nm. The ESA feature at 516 nm appears consistent with the absorption by a lower-lying triplet state to populate a higher-lying triplet state (triplet-triplet absorption), and the ESA feature at 480 nm may correspond to a similar absorption event where a photon is absorbed to promote the occupation of a lower-lying excited singlet state to a higher-lying singlet state (singlet-singlet absorption) based on other TA studies of rubrene single crystals [101, 102]. The observation of triplets in rubrene has been attributed to singlet fission, and understanding the singlet fission properties and pathways in rubrene (e.g. thermal activation [102], triplet separation [103]) continues to be a intriguing area of exploration. We have explored using different pump polarizations to determine any polarization-dependence of signals in samples annealed on glass/ITO, and we have probed at different locations within a spherulite. Unfortunately, the used white light probe signal fluctuated greatly and required further troubleshooting. To continue TAM studies on our rubrene thin film samples, in addition to fixing the white light stability, we recommend conducting a pump power-dependence test, evaluating considerations for measurements on SiN substrates, and determining how different pump excitations [101, 102] may yield different insights for a spatially-resolved evaluation of excitation dynamics in rubrene hybrid microstructures and spherulites.

We also performed exploratory measurements on rubrene spherulites and single crystals with steady-state interferometric scattering (iSCAT) and stroboscopic scattering (stroboSCAT) microscopies. Given the higher spatial resolution and ability to probe a variety of energetic carriers ranging from excitons to phonons [6], iSCAT and stroboSCAT complement TAM measurements. Even though height variations of spherulite crystalline grains are only on the order of ∼3-5 nm, iSCAT can distinguish the characteristic patterns of individual nanocrystalline rods that grow anisotropically outward (Figure 2.22a). stroboSCAT of rubrene single crystals clearly shows anisotropic diffusion along the π-stacking direction of the crystal (Figure 2.22b), and the mean squared displacement (MSD) plot (Figure 2.22c) shows that diffusion occurs up to five times faster along the π-stacking direction than it does orthogonal to that direction. In the future, stroboSCAT could be used to study rubrene spherulite thin films to understand how the morphology and changes in crystalline orientation impact energy transport.

X-ray scattering and microscopy techniques continue to be an important and growing avenue for quantitative structural characterization of organic semiconductors on multiple

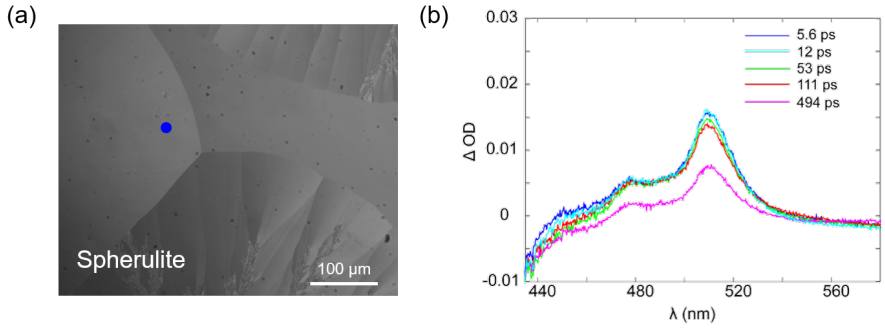

Figure 2.21: Transient absorption (TA) spectra of rubrene spherulite at different time delays. (a) POM image (using TAM setup) of rubrene spherulite on glass/ITO substrate with blue circle as reference for area of investigation with pump excitation at 400 nm. (b) TA spectra at time delays from 5 - 500 ps.

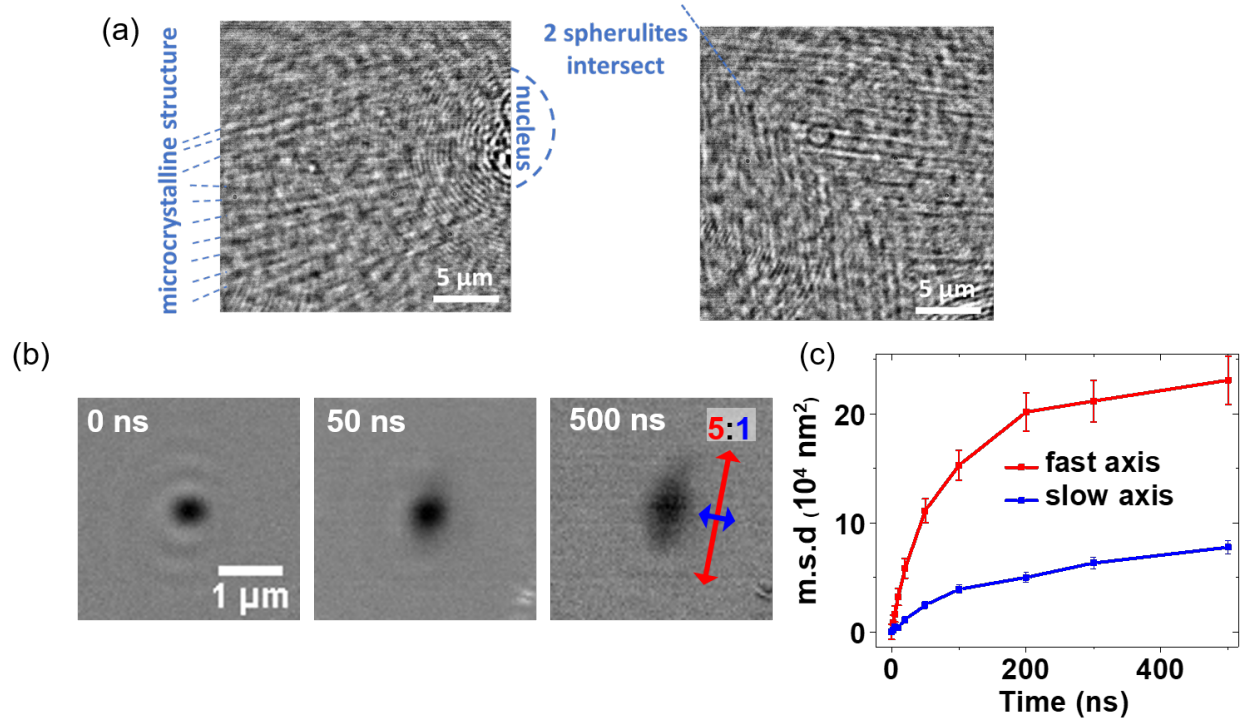

Figure 2.22: iSCAT and stroboSCAT measurements on rubrene spherulites and single crystals. (a) iSCAT images of rubrene spherulites. (b) stroboSCAT measurements with images at different time delays and (c) diffusion plot. Measurements and data analysis performed by Dr. Milan Delor.

length scales [34]. Future GIWAXS analysis efforts could explore the origin of the non-perfect orthorhombic unit cell observed on SiN substrates with Rietveld refinement, or could determine whether lattice compression or strain can be extracted from X-ray diffraction patterns after accounting for geometric broadening. Repeating *in situ* GIWAXS crystallization measurements with an adjusted annealing protocol based on the heater and substrate's temperature rise will ensure similar crystalline structures measured across imaging modalities. Additionally, using substrates that have pre-fabricated fiducials will facilitate precise identification of sampling locations of interest. In the future, STXM measurements at three different polarizations should ensure a fully quantitative orientation map; however, that could require some compromise between dwell time and scan sizes (where hundreds of μm^2 is not typical due to time and stage motor constraints).

While multimodal characterizations often focus on one material at a time, comparative multimodal studies are also possible. For example, we also used microdiffraction to probe and compare rubrene, 2,4,5,6-tetra(9H-carbazol-9-yl) isophthalonitrile (4CzIPN), and rac-BINAP (BDP) (Figure 2.23). Based on our collaborator's extensive comparative crystallization study on thin film organic semiconductors [104], we identified rubrene, 4CzIPN, and BDP as molecules of comparative interest since they are all capable of forming both platelets and spherulites at different temperatures and with different resulting crystal structures (e.g., orthorhombic and triclinic). Thus, it would be an opportunity to compare diffraction patterns across the different molecules in crystalline and polycrystalline structures and to learn about any differences in strain or stress. We acquired preliminary microdiffraction measurements of platelet and spherulite thin films of these three molecules at spatially varying locations. Performing X-ray energy scans helped ensure that we collected as many diffraction peaks for a given sample as possible. Although indexing of the peaks needs to be completed, a consistent trend that was observed amongst all samples was that spherulite films exhibited fewer diffraction peaks relative to their platelet forms. This was not surprising given the increased polycrystallinity in spherulite films. Further discussion on these measurements are given in Appendix C. This microdiffraction comparative study is an example of expanding multimodal characterization studies to include several molecules for comparison to enrich our understanding of structure-function properties in organic semiconductor thin films.

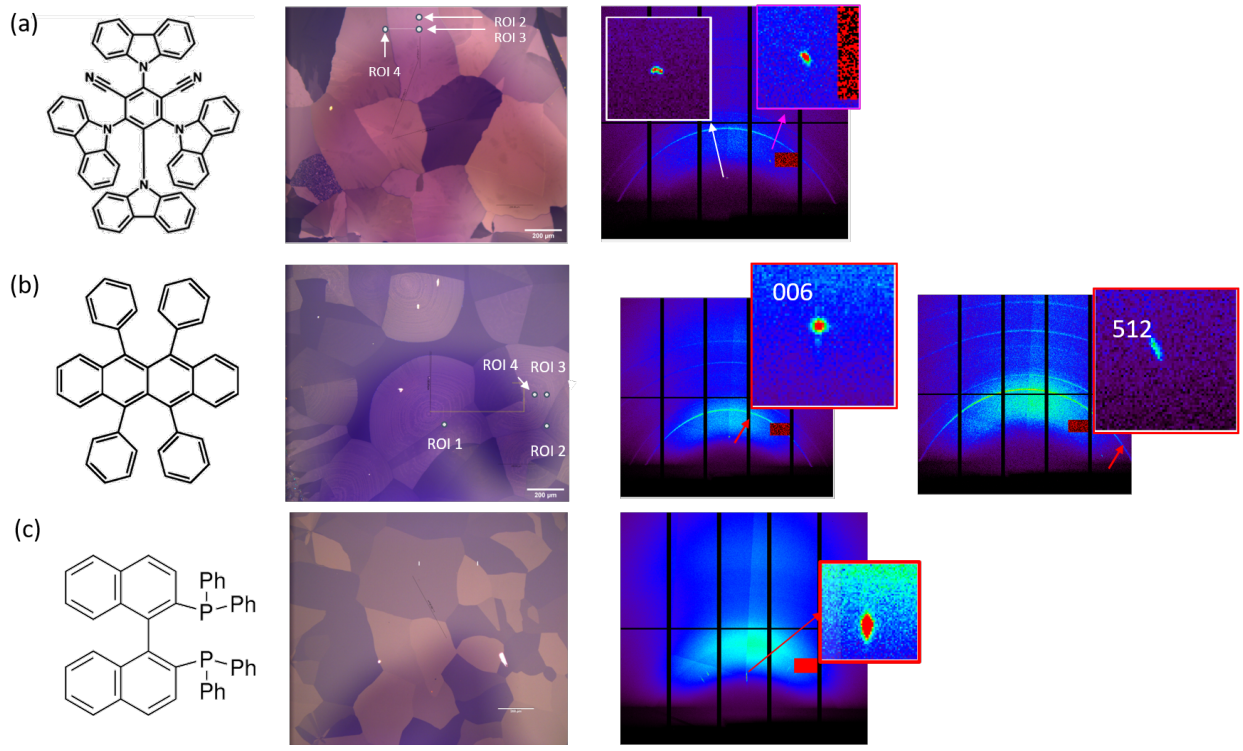

Figure 2.23: X-ray microdiffraction measurements of rubrene, 4CzIPN, and BDP. (a) 4CzIPN molecule with corresponding polarized optical image of platelet film and representative microdiffraction pattern with inset of peaks. (b) Rubrene molecule with corresponding polarized optical image of platelet film and representative microdiffraction pattern with inset of peaks. (c) BDP molecule with corresponding polarized optical image of platelet film and representative microdiffraction pattern with inset of peaks. Data collection and analysis conducted with Jordan Dull and Dr. Nobumichi Tamura (staff scientist) at the Advanced Light Source, Lawrence Berkeley National Laboratory, at beamline 12.3.2.

Chapter 3

Effect of Anisotropic Confinement on Electronic Structure and Dynamics of Band-Edge Excitons in Inorganic Perovskite Nanowires

3.1 Introduction

Perovskites have garnered immense attention for their outstanding optical and electronic properties that hold much potential in applications such as optoelectronic devices or photovoltaics. Their properties can be tuned in many ways including size- and dimension-engineering. Here we investigate the anisotropic transport properties of and polarization-dependent optical interactions with $CsPbBr_3$ nanowires with lateral widths of 10 nm [2]. We do so by producing nanowire bundles — many monodisperse nanowires aligned parallel to one another. The individual wires are found to be essentially noninteracting, allowing us to measure their properties when oriented in a well-defined direction while achieving sensitivities far beyond what could be achieved with single-nanowire spectroscopy.

We image carrier diffusion within a single bundle using a pump-probe elastic scattering microscopy, stroboscopic interferometric scattering microscopy (stroboSCAT) [6, 72]. We find rapid diffusion along the axis of the nanowires through an environment with extremely low trap densities. Separately, we measure the polarization-resolved ultrafast electronic dynamics with transient absorption microscopy (TAM). We find that the dynamics are similar to those of bulk $CsPbBr_3$ but that the band-edge transition energy depends on the polarization of the incident light relative to the nanowire axis. Finally, we use fluorescence anisotropy

measurements in solution to infer a corresponding anisotropy in the transition dipole moment strengths. The polarization-dependent splitting of the band edge exciton is consistent with splitting due to long-range exchange in conjunction with the shape anisotropy of the nanowire [105, 106] while density functional theory (DFT) calculations indicate that crystal field effects cannot explain the observed polarization dependent splitting. The magnitude of the observed splitting suggests that two-dimensional confinement of the exciton in nanowires, in conjunction with dielectric confinement effects associated with the difference in the dielectric constant of the nanowire and the surrounding medium, [107] causes enhancement of the exciton binding energy relative to bulk excitons, with a concomitant increase in the long-range exchange splitting energy.

3.1.1 Inorganic perovskites

Inorganic lead halide perovskites share the chemical formula of $APbX_3$, where A is a monovalent inorganic cation, Pb is the bivalent metal cation, and X is a halogen or combination of halogens [108]. The chemical structure greatly impacts the resulting properties and capabilities of these semiconducting materials. For example, relative to an organic cation, the inorganic cation provides more stability in the presence of light, oxygen, and water, which can be further enhanced through encapsulation [109–113]. More generally, perovskites exhibit high charge carrier mobilities, strong optical absorption, and efficient photoluminescence (PL), which have led to applications in devices such as photovoltaics, where perovskite-based photovoltaics achieve performances with efficiencies above 12% [109, 114]. These same properties have been used to produce lasers with low lasing thresholds and high quality factors, [110, 115] as well as sensitive photodetectors [116, 117] and scintillators [118].

Many of the above applications involve nanostructures, in part because size offers a route to tune properties, [119–122] and also because novel behaviors can emerge when the material dimensions become comparable to the exciton Bohr radius, which is typically a few nanometers [116]. A common route for producing perovskite nanostructures is through hot injection, which is a liquid phase synthesis method that separates the nucleation and growth stages. This separation ensures that new nuclei are not forming as nanocrystals begin to grow, which aids the formation of uniformly sized nanocrystals in a given batch. Several key parameters control the size, size-distribution, and shape of the nanocrystals: injection temperature of the cation or anion precursor, concentration of precursors, the ratio of ligands to precursors, and reaction time [123].

This method works well to produce prototypical inorganic halide perovskite, $CsPbBr_3$, which has been extensively studied in nanocube form. For example, it has been found that optical emission occurs with subnanosecond lifetimes with high quantum efficiency in nanocubes of $CsPbBr_3$, [119] which has been ascribed to an inversion of the order of the bright and dark fine structure levels caused by the Rashba effect. Geometry also plays an important role, as confinement makes biexciton interactions more prevalent [124, 125] and the presence of surface states can affect carrier trapping [126].

Tuning the ligand combinations and ratios in colloidal perovskite synthesis can generate other shapes such as nanoplatelets and nanowires, in which confinement is limited to one or two dimensions. While nanocubes typically dominate structure-function studies, nanoplatelets and nanowires have garnered attention as well for their ability to produce novel assemblies, [121, 127] modify the electronic states in unique ways, [128] change the primary exciton decay mechanism, [129] and lead to new behaviors such as exciton dissociation at edge states [130] or polarization-dependent optical interactions [117, 131].

3.1.2 Motivation for pump-probe microscopy studies for perovskites

Perovskites exhibit long carrier lifetimes and long diffusion lengths that make them amenable for photovoltaics and other optoelectronic devices [132]. To understand the origins of these desirable properties, a comprehensive framework of their photophysics requires mapping the charge carrier dynamics and transport on the sub-micron to nanoscale [132]. Pump-probe microscopies based on transient absorption and scattering, such as TAM and stroboSCAT as introduced in Chapter 1, locally track the photogeneration of excited species within the energetic landscape of a material [6, 133]. This approach enables discovery of how heterogeneity directly impacts charge carrier dynamics and transport, such as the roles of morphology and grain boundaries in perovskite thin films [6, 68, 132, 133].

While pump-probe microscopies have been extensively applied to thin films, they can also be used to probe nanowires. Nanowires serve as a model system to learn about how chemical structure and quantum confinement affect the resulting photophysics [134]. For example, TAM directly visualized carrier motion in a single Si nanowire with a p-type/intrinsic/n-type junction [135]. Grumstrup, E.M. *et al.* observed that after initial diffusion of charge carriers generated in the intrinsic region, electron-hole recombination decreases the charge carrier density which leads to charge separation induced by the junction potential. This study demonstrates that rich dynamics can be found in a single nanostructure, rather than the bulk, which further informs on nanostructure design. Acquiring a baseline understanding of the fundamental photophysics in a perovskite nanowire is necessary so that as chemical structure changes or they are combined with other quantum confined materials into heterostructures [136], structure-function properties may be systematically optimized for a given device geometry.

3.2 Characterization of $CsPbBr_3$ nanowire bundles

3.2.1 Nanowire synthesis and deposition

To investigate the effect of two-dimensional confinement on $CsPbBr_3$, we synthesize monodisperse nanowires (NWs) with widths of 10 nm [137, 138]. First, 5 mL of 1-octadecene and 0.2 mmol of $PbBr_2$ were loaded into a 3-neck flask and degassed under vacuum for 30 min

at 120°C. Then, 0.8 mL of dried octylamine and 0.8 mL of dried oleylamine were injected at 120°C under N_2. The temperature was raised to 135°C, and the solution was stirred for 20 min; 0.7 mL of as-prepared Cs-oleate solution was swiftly injected into the opaque white solution. After 50 min, the reaction mixture was cooled by an ice–water bath. The NWs were isolated by centrifugation at 6000 rpm for 5 min and washed once with toluene. The obtained precipitated NWs were redispersed in toluene or cyclohexane for further use. Dispersing in toluene results in nanowire bundles, whereas cyclohexane helps to obtain isolated nanowires.

Large (hundreds of nanometers thick) $CsPbBr_3$ nanowires were prepared following Eaton *et al.* [115]. First, 460 mg of PbI_2 was dissolved in 1 mL of anhydrous dimethylformamide and stirred at 70°C overnight before further use. The PbI_2 solution was spun onto a poly(3,4-ethylenedioxythiophene) polystyrene sulfonate (PEDOT:PSS)-coated glass substrates (Solarmer) at 1000–3000 rpm for 120 s and then annealed at 100°C for 15 min. The PbI_2 film was carefully submerged into a glass vial containing a solution of 8 mg/mL CsBr in methanol, with the PbI_2 side facing up. The capped reaction vial was heated at 50°C for 12 h, and the substrate was removed after cooling for some time. Then the substrate was washed twice in 2-propanol (each time for 30 s). The sample was then dried by heating to 50°C for 5 min.

Nanowire solutions were diluted and deposited by drop casting onto glass coverslips cleaned by sonication in acetone, 2-propanol, and Millipore water. In order to speed evaporation of the droplet, the coverslip was placed in a Petri dish on a hot plate heated to 60°C. The Petri dish was regularly picked up and tilted in order to spread the nanowires around on the coverslip. Individual bundles were located by inspection.

3.2.2 Optical and electron characterization

Nanostructures of $CsPbBr_3$ typically adopt an orthorhombic structure [126, 138–140] as shown in Figure 3.1a or tetragonal structure [141], and are capped with ligands for stability. In toluene the nanowires self-assemble into bundles, illustrated in Figure 3.1b. Transmission electron microscopy (TEM) images of nanowires were taken on a Hitachi H7650 at an accelerating voltage of 120 kV. A TEM image of a 10 nm nanowire bundle is shown in Figure 3.1c. The nanowires are well-aligned with each other and have low size dispersion—examining dozens of nanowires in TEM, we observed that all have diameters between 9 and 11 nm. Optical images of drop cast bundles are shown in Figure 3.1d. Note that individual bundles can be located and that the bundles can be up to several micrometers in width and tens of micrometers in length—larger than the optical spots used in transient absorption microscopy (indicated in Figure 3.1d by the blue focal spot).

Absorption measurements were done in an Agilent Cary 100 UV–vis spectrophotometer, and PL measurements for samples in solution were collected with a PicoQuant FluoTime 300 fluorimeter, using PicoQuant pulsed diode lasers and a PDL 820 driver. The absorption and PL spectra of nanowire bundles in solution are shown in Figure 3.1e. PL measurements of three individual bundles are found to have identical fluorescence spectra using an Olympus IX83 microscope as shown in Figure 3.2a and 3.2b. The identical fluorescence spectra imply

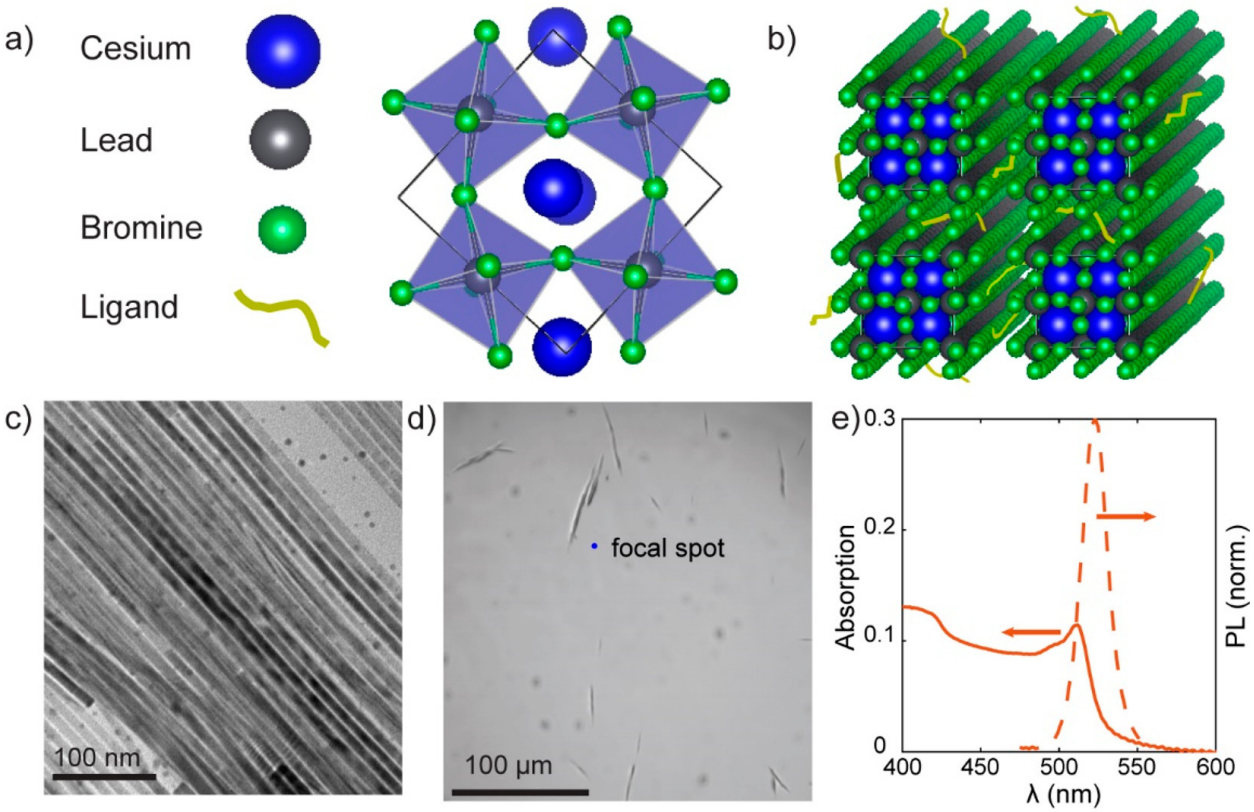

Figure 3.1: Structure and properties of $CsPbBr_3$ nanowire bundles. (a) Unit cell of orthorhombic $CsPbBr_3$, oriented with the $\langle 110 \rangle$ axis pointing up and the $\langle 001 \rangle$ axis pointing out of the page. (b) Cartoon nanowire bundle, with only a few ligands depicted for clarity. (c) TEM image of 10 nm diameter nanowire bundles, showing alignment, length, and monodispersity of nanowires. (d) Optical image of 10 nm diameter nanowire bundles, showing their size compared to a typical pump laser focal spot used in transient absorption microscopy (blue dot). (e) Absorption (solid curve) and photoluminescence (dashed curve) of 10 nm nanowires.

interbundle consistency. The time-resolved PL of nanowire bundles in solution exhibit a multiexponential decay in Figure 3.2c. The exciton Bohr diameter of bulk $CsPbBr_3$ is roughly 7 nm, [142, 143] meaning that 10 nm nanowires are in the weak confinement regime. As has been known for the weak confinement regime in quantum dots for many years, a size-dependent transition energy, along with discrete transition energies, is expected [144]. In our samples, this manifests as a slightly larger bandgap and bluer absorption, as can be seen by comparing against bulk $CsPbBr_3$ (see discussion of Figure 3.3b, below). We conclude that bundled nanowires still experience the effects of quantum confinement.

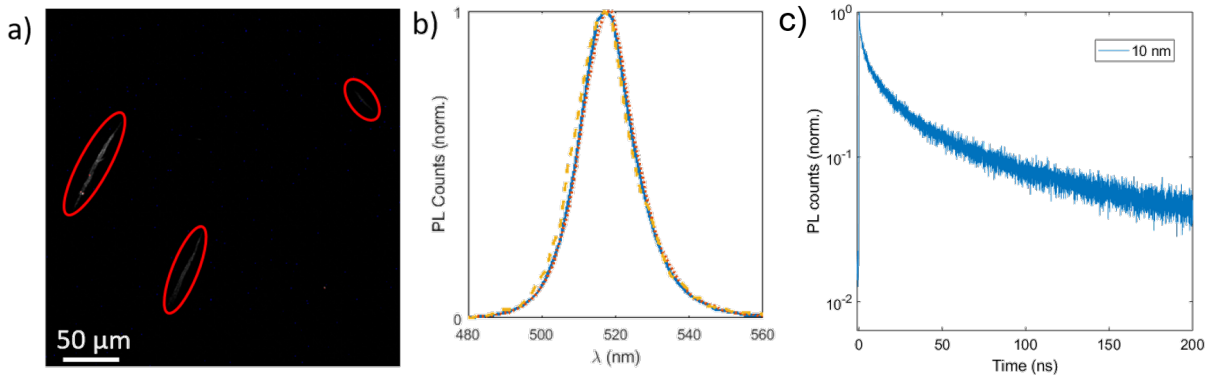

Figure 3.2: Additional PL characterization of $CsPbBr_3$ nanowire bundles. (a) Confocal microscopy PL image of 10 nm nanowire bundles (circled in red), excited at 473 nm. (b) Normalized PL spectra of the bundles in (a). (c) Normalized time-resolved PL (TRPL) of bundles of 10 nm nanowires in solution.

3.3 Insights on diffusion and traps with stroboSCAT

We use stroboSCAT to image exciton diffusion along both the longitudinal and transverse axes of the nanowire bundles, which enables us to characterize the barriers to exciton transport. stroboSCAT employs interferometric scattering (iSCAT) as a probe (PicoQuant 640 nm diode), which uses the interference between light scattered off of the sample and its substrate from the back focal plane of the objective in order to achieve exquisitely sensitive images. In stroboSCAT, a separate pump pulse (PicoQuant 440 nm diode) is first focused onto the sample with an objective, and the resulting excited species appear in the iSCAT image due to their perturbation to the local polarizability. Controlling the time delay between the pump and the iSCAT pulse with a PDL 828 "Sepia II" driver in our home-built reflection-mode microscope allows us to track energy migration [72]. The scattered probe light was interfered with a reflection off of the sample–substrate interface and imaged with a Pixelink PL-D752Mu-T camera.

An iSCAT image of a nanowire bundle is shown in Figure 3.3a, and stroboSCAT snapshots at time delays of 0.0, 0.4, and 1.0 ns are shown in Figure 3.3b–d. The dark patch indicates increased polarizability due to the presence of excited species, and it can be seen to expand along the bundle as time advances. To quantify the extent of diffusion we plot profiles along the red dashed lines drawn in Figure 3.3b–d. These profiles, which show longitudinal diffusion, are shown in Figure 3.3e. The tails of the distribution broaden with time, indicating that exciton diffusion occurs.

In order to track transverse diffusion we also excite along the side of a bundle and plot transverse profiles, shown in Figure 3.4. The profile expands from a standard deviation of approximately 90 nm initially (yellow curve) to 145 nm after 0.4 ns (red curve), for a diffusivity of approximately 0.2 cm^2/s, substantially smaller than the longitudinal diffusivity

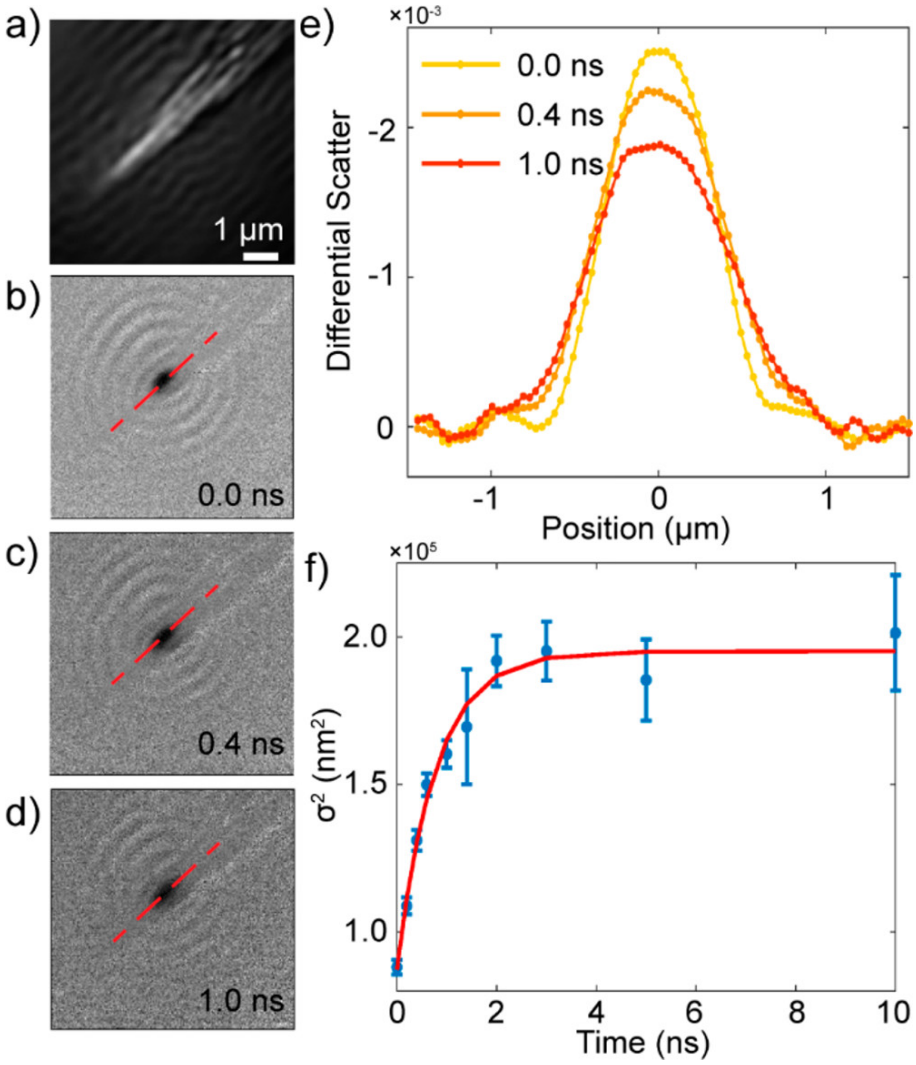

Figure 3.3: Observing diffusion of energy through nanowires with stroboSCAT. (a) Interferometric scattering image of 10 nm diameter nanowire bundle. (b–d) Differential scattering images at time delays of 0.0, 0.4, and 1.0 ns after pump excitation, showing longitudinal diffusion. (e) Profiles along the paths indicated by red lines in parts b–d, showing diffusion along the longitudinal axis of the nanowires. (f) Mean squared displacement of the Gaussian fits to scattering profiles such as those shown in panel e. The data are fit to an exponentially decaying diffusivity (red line), yielding an initial diffusivity of 0.69 ± 0.05 cm^2/s and a time constant of 0.78 ± 0.08 ns.

in Figure 3.3e. After 0.4 ns the excitations reach the far sidewall, and the profiles no longer provide useful information. Although transverse diffusion occurs, which is indicative of internanowire energy transfer, it is much slower than longitudinal diffusion.

By fitting the above stroboSCAT data to a model we are able to extract the intrinsic longitudinal diffusivity of $CsPbBr_3$ nanowires, as well as the internanowire transverse diffu-

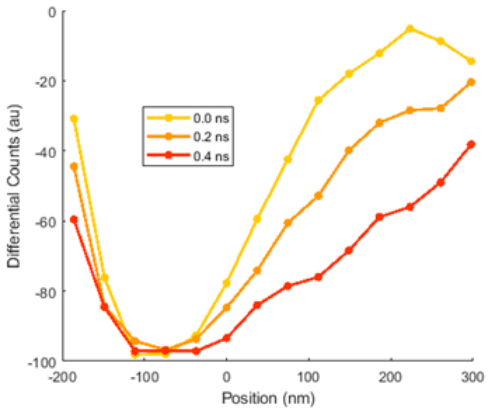

Figure 3.4: Transverse stroboSCAT profiles of 10 nm nanowire bundle after excitation near a sidewall of a nanowire bundle. Note that the colors correspond to different delay times and the horizontal axis scale is different than in Figure 3.3e.

sivity. The profiles in Figure 3.3e are fit to Gaussian functions in order to extract the mean squared displacement (MSD) of the excitons σ^2, where σ is the standard deviation of the Gaussian fit. The MSD as a function of pump-probe delay time is shown in Figure 3.3f. Ordinary diffusion would present a straight line from which we could extract the diffusivity, but that is clearly not the case here. We find that the data in Figure 3.3f fit well to an exponentially decaying effective diffusivity, $D(t) = D_0 e^{-t/\tau_d}$, where D_0 is the initial diffusivity and τ_d is the diffusion decay time. This leads to an exciton distribution that broadens as

$$\sigma(t)^2 = \sigma_0^2 + 2D_0\tau_d(1 - e^{-t/\tau_d}) \tag{3.1}$$

which is the red curve of best fit plotted in Figure 3.3f. This is an unusual result. We first consider that the excitons diffuse through an energetically disordered landscape, which could lead to subdiffusive behavior. However, that behavior would manifest as a power law, [145] $D(t) = D_0(t)^{\alpha-1}$, and that functional form provides a poor fit to the data as shown in Figure 3.6.

In some works, an exponentially decaying diffusivity has been attributed to hot carrier cooling, [100] but that process occurs over a picosecond time scale [146] and cannot explain the nanosecond-scale decay that we observe. We also consider that our observations could be an artifact of nonlinear annihilation, which would cause the center of the distribution to decrease faster than the tails, providing the illusion of initially rapid diffusion. Varying the pump fluence, however, has no noticeable effect on τ_d, as shown in Figure 3.6, indicating that nonlinear exciton–exciton interactions cannot be responsible for the observed behavior.

3.3.1 Model of nanowire exciton diffusion with trapping

Having ruled out several potential causes of the exponentially decaying diffusivity, we hypothesize that exciton traps limit exciton diffusion. These could be surface traps due to

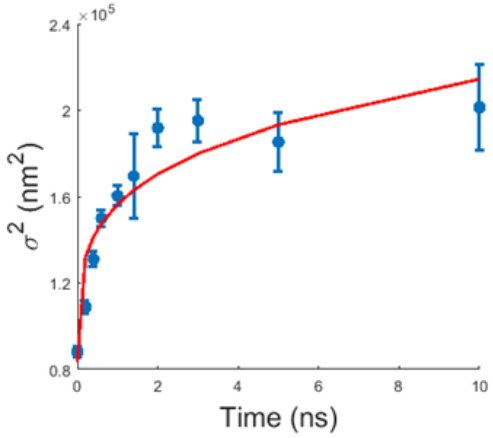

Figure 3.5: Longitudinal stroboSCAT diffusion fit to a power law. stroboSCAT diffusion data (blue) from Figure 3.3f, with an attempted fit to a power law (red), $D(t) = D_0 t^{\alpha-1}$.

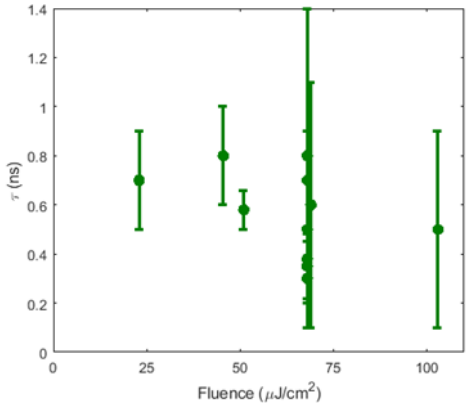

Figure 3.6: Measured diffusion decay time as a function of pump laser fluence. If the initial rapid diffusion were an artifact of annihilation, we would expect the decay time to depend on fluence, but that is not seen to be the case.

atomic defects or incomplete ligand coverage. We construct a model and use it to extract the intrinsic exciton diffusivity and the trap density. The model consists of a population of mobile excitons, $p_{\mathrm{m}}(x,t)$ and trapped excitons $p_{\mathrm{tr}}r(x,t)$. The mobile excitons diffuse in one dimension with diffusivity D, while the trapped excitons are stationary. We use a spatially uniform trapping rate, k_{tr}, and both populations decay with rate k_{fl}. The equations for this model are

$$\frac{\partial p_{\mathrm{m}}}{\partial t} = D\frac{\partial^2 p_{\mathrm{m}}}{\partial x^2} - k_{\mathrm{tr}}p_{\mathrm{m}} - k_{\mathrm{fl}}p_{\mathrm{m}} \tag{3.2}$$

$$\frac{\partial p_{\mathrm{tr}}}{\partial t} = k_{\mathrm{tr}}p_{\mathrm{m}} - k_{\mathrm{fl}}p_{\mathrm{tr}} \tag{3.3}$$

We initialize the model with the following conditions:

- The pump pulse imparts a Gaussian distribution with variance σ_0^2 to the mobile carriers.
- There are no trapped carriers.
- The value of σ_0 is measured in the initial distribution.
- The fluorescence lifetime τ_{fl} is 2.1 ns as found from the fastest component of the time-resolved photoluminescence lifetime (TRPL) measurement from 10 nm nanowires (Figure 3.2c).

We make the equations dimensionless by defining σ_0 as the unit of length and $\frac{1}{k_{\text{fl}}}$ as the unit of time. We let $k \equiv k_{\text{tr}}/k_{\text{fl}}$ be the dimensionless trapping rate, and D be the dimensionless diffusivity, and now we have the following equations:

$$\frac{\partial p_{\text{m}}}{\partial t} = D\frac{\partial^2 p_{\text{m}}}{\partial x^2} - p_{\text{m}} - kp_{\text{m}} \tag{3.4}$$

$$\frac{\partial p_{\text{tr}}}{\partial t} = kp_{\text{m}} - p_{\text{tr}} \tag{3.5}$$

with initial conditions

$$p_{\text{m}}(x, t = 0) = \frac{1}{\sqrt{2\pi}} e^{\frac{-x^2}{2}} \tag{3.6}$$

$$p_{\text{tr}}(x, t = 0) = 0. \tag{3.7}$$

Equations 3.6 and 3.7 can be solved exactly. For mobile carriers, the solution is an expression for ordinary diffusion times a decaying exponential with rate *1 + k*:

$$p_{\text{m}}(x, t) = \frac{e^{\frac{-x^2}{2(1+2Dt)}}}{\sqrt{2\pi(1 + 2Dt)}} e^{-(1+k)t}\theta(t), \tag{3.8}$$

where $\theta(t)$ is the Heaviside step function. The equation for trapped carriers can be solved by taking the Fourier transform, re-arranging, and taking the inverse Fourier transform. We find that the result is a convolution between a decaying exponential of rate 1 and the expression $kp_{\text{m}}(x,t)$:

$$p_{\text{tr}}(x, t) = \int_{-\infty}^{\infty} kp_{\text{m}}(x, \tau)e^{\tau - t}\theta(t - \tau)d\tau. \tag{3.9}$$

Using Equation 3.8 for $p_{\text{m}}(x, t)$ we see that Equation 3.9 can be solved but not in a closed form. Here,

$$
\begin{aligned}
p_{\mathrm{tr}}(x,t) =& \frac{\sqrt{k}}{4\sqrt{D}} e^{-t+k/2D} \\
& \left[e^{-|x|\sqrt{\frac{k}{D}}} \left(\mathrm{Erf}\left(\frac{\sqrt{\frac{k}{D}}(1+2Dt) - |x|}{\sqrt{2(1+2Dt}} \right) - Erf\left(\frac{\sqrt{\frac{k}{D}} - |x|}{\sqrt{(2)}} \right) \right) \right. \\
& \left. + e^{+|x|\sqrt{\frac{k}{D}}} \left(\mathrm{Erf}\left(\frac{\sqrt{\frac{k}{D}}(1+2Dt) + |x|}{\sqrt{2(1+2Dt}} \right) - \mathrm{Erf}\left(\frac{\sqrt{\frac{k}{D}} + |x|}{\sqrt{(2)}} \right) \right) \right] ,
\end{aligned}
\tag{3.10}
$$

where Erf() is the error function. This allows us to plot the total population, $p(x,t) = p_{\mathrm{m}}(x,t) + p_{\mathrm{tr}}(x,t)$ and fit it to a Gaussian as shown in Figure 3.7a for parameters $D = 5$ and $k = 1$ at time $t = 1$. We find that a Gaussian fit is appropriate, even for these parameters, which were chosen to accentuate the way in which the model can deviate from a Gaussian. For lower values of the ratio D/k, the result is even more Gaussian-like. The profile can be fit to a Gaussian to extract the variance σ^2. Plotted as a function of time, we see it fits well to a decaying exponential (Figure 3.7b).

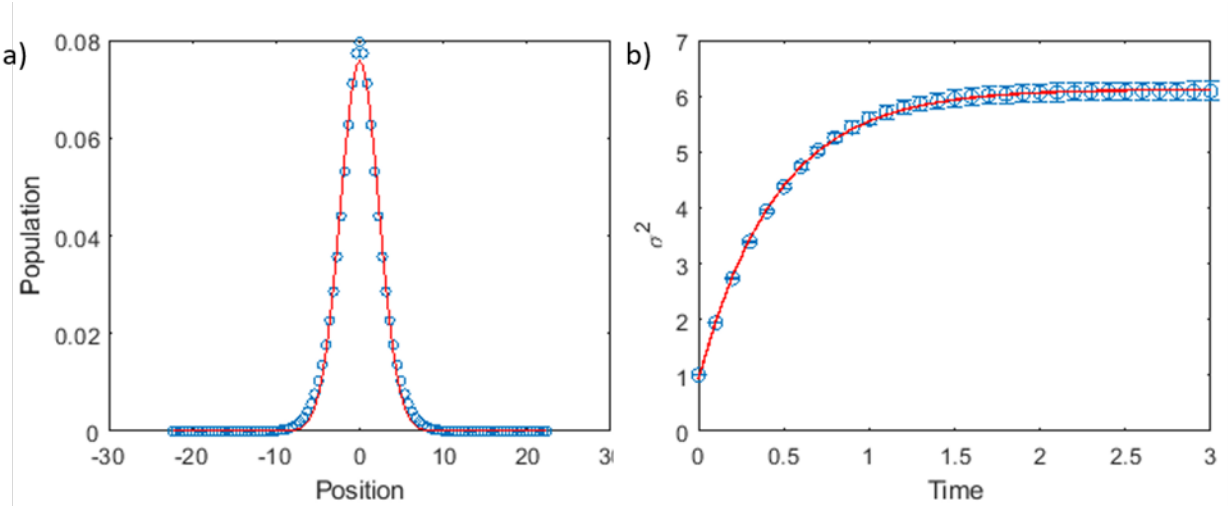

Figure 3.7: Results of the diffusion trapping model. (a) Total exciton profile at time $t = 1$ for parameters $D = 5$ and $k = 1$. Profiles are fit to a Gaussian to extract the variance, which is plotted as a function of time and (b) fit to an exponentially decaying diffusivity (Equation 3.1).

The model clearly predicts results that look like our observations. Next, we use the fitting results to extract the values of various parameters in the model. The fits shown in Figure 3.7 return $\sigma_0 = 0.96$ (close to the real value of 1), $D = 5.7$ (slightly higher than real value of 5), and $\tau_d = 0.45$ (significantly different from 1). We fit the diffusion trapping model using Equations 3.2-3.10 for many values of D and k in order to create a map between those

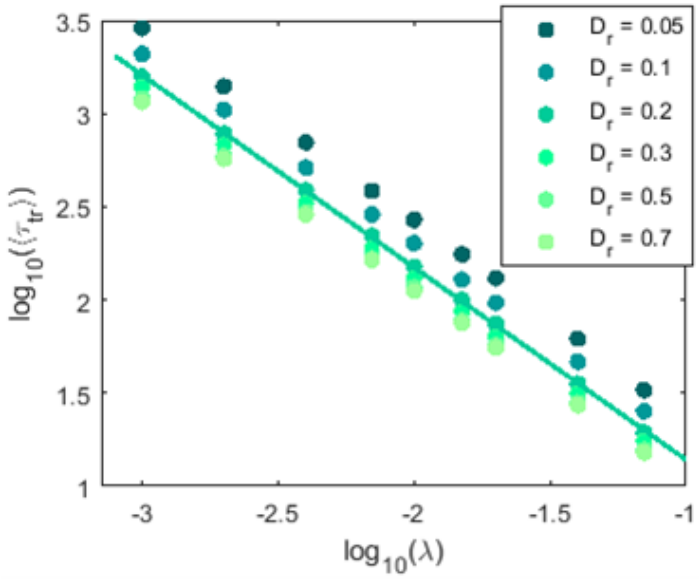

Figure 3.8: Results of diffusion simulation to relate mean trapping time to linear trap density. Mean trapping time is plotted vs. linear trap density on a log-log plot, for several values of D_r.

variables and the measured values, D_0 and τ_d. Dimensionless numbers were converted to real numbers by measuring the initial distribution to get σ_0 and using the lifetime as measured with TRPL to get k_{fl}.

Model for trap density

While the intrinsic diffusivity, D, is of interest, the trapping rate, k_{tr}, is not so physically meaningful. We convert the trapping rate to a trap density with a second model, described here. We consider a square bundle of n by n nanowires, each of length l. The linear trap density is fixed to be some λ. For each nanowire, the number of traps on that nanowire is drawn from a Poisson distribution of mean $l\lambda$, and the traps are placed randomly along that nanowire. An exciton is initialized at an arbitrary position, and at each time step hops either left or right along its nanowire. With some probability D_r, it may hop in each of the orthogonal directions. This number is ratio of the transverse to the longitudinal diffusivity. Periodic boundary conditions are used. The simulation runs until the exciton encounters a trap. Running many such simulations produces a distribution of trapping times, and hence an average trapping time, $\langle \tau_{tr} \rangle$.

For given values of λ and D_r, 20,000 trajectories were run. The system size was set to $n = 30$ and $l = 20/\lambda$, which was found to be large enough so that the results converged. Figure 3.8 shows the value of $\langle \tau_{tr} \rangle$ as a function of λ on a log-log plot for several values of D_r. In all cases, the data lie on a line with a slope of -1. This implies that $\langle \tau_{tr} \rangle \propto 1/\lambda$, although the proportionality constant depends on D_r. We estimate D_r using the transverse

diffusion measurement shown in Figure 3.6. Those data, when fit to Gaussians, indicate a transverse diffusivity of $D_\mathrm{t} = 0.22 \pm 0.13$ cm^2/s. The longitudinal intrinsic diffusivity for that same bundle was $D_\mathrm{l} = 0.76 \pm 0.09$ cm^2/s, hence $D_r = \frac{D_\mathrm{t}}{D_\mathrm{l}} = 0.29 \pm 0.17$. using this value, we can convert the trapping rate to a linear trap density.

There are several simplifications in this model. First, although excitons are the dominant excited species, charge carriers are likely present as well, since the bulk exciton binding energy is only about 40 meV [143]. Also, the exciton decay is more complicated than a single rate constant, as seen in Figure 3.2c, and we expect that trapping modifies the decay rate. Further study of the trapped exciton dynamics might provide insight into the traps' localization energy and allow for a more sophisticated model. Finally, trapping is not spatially uniform, although given that the distance between traps is likely too small to be spatially resolved, this is a good approximation. More importantly trapping is not temporally uniform–as traps fill, we might expect the rate to decrease. Nevertheless, we find that the model in Equations 3.2 and 3.3 fits the data well and provides a rough way to estimate the trap density, whereas adding more free parameters would result in overfitting.

3.3.2 Results from trapping model

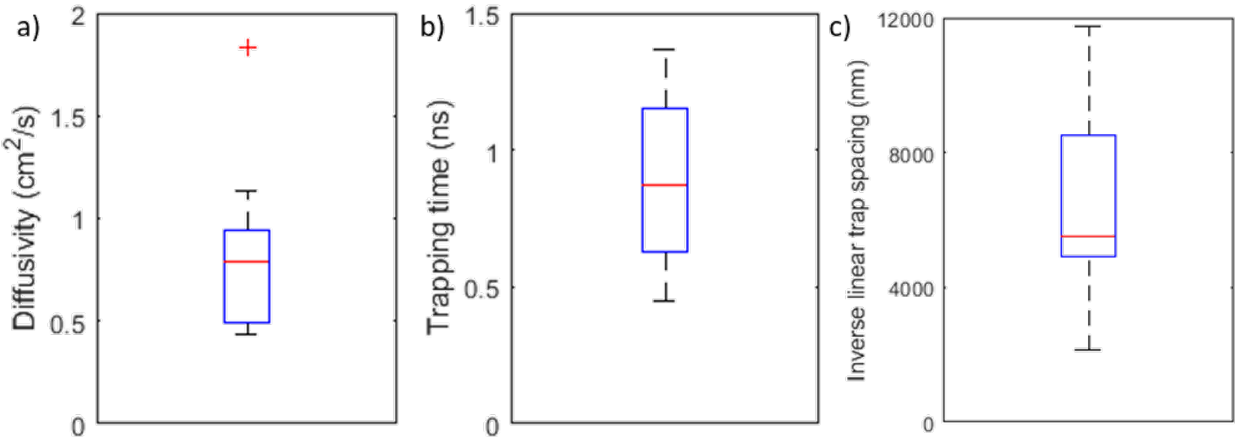

Figure 3.9: Box plots of several values measured for each of 11 nanowire bundles. Box plots of (a) intrinsic longitudinal diffusivity D_0, (b) trapping time $1/k_\mathrm{tr}$, and (c) inverse linear trap spacing $1/\lambda$ measured for each of 11 nanowire bundles.

We studied 11 nanowire bundles using the technique described above and found a range of values shown in box plots (Figure 3.9). The mean value of the intrinsic diffusivity was found to be 0.8 cm^2/s. This is very similar to the value of 1.0 cm^2/s for bulk $CsPbBr_3$, [72] and indicates that weak confinement does not affect the excitons' ability to diffuse. This is

similar to the findings of Tian *et al.* [147], who measured carrier diffusion in large, hundred-nm scale nanowires and nanoplatelets of methylammonium lead halide perovskites. They found heterogeneity between samples but also that there is no clear correlation between diffusivity and shape [147]. Our work extends these findings into the quantum confined regime. We also measure a transverse diffusivity of 0.2 cm^2/s (Figure 3.4), which indicates weak but nonzero internanowire coupling. As the Böhr diameter is about 7 nm, the excitons are confined to individual nanowires, and hence, transverse diffusivity should depend on internanowire separation, and may be tunable by adjusting the ligands. Finally, we extract linear trap densities that range from one trap every 1 μm to one trap every 10 μm (10^{15}– 10^{16} cm^{-3}). Though we cannot determine a precise distribution of individual nanowire lengths, TEM images indicate that they are on the order of one micron long (the bundle itself, which comprises many nanowires, is much longer), suggesting that the number of traps per nanowire is close to 1 and that the spacing between traps on any given wire is likely to be several times larger than a typical diffusion length. Traps could also be localized at the ends of the nanowires. Our measured trap densities are slightly higher than those found via electrical transport measurements [137]. This could indicate pump-induced damage, though we do not observe degradation throughout the course of the experiment and the trap density is still notably low. The identity and spatial distribution of traps are worthy of further study.

3.4 Optical absorption spectroscopy of nanowire bundles

Nanowire bundles were studied with a set of 3 complementary absorption-based techniques: polarized linear absorption spectroscopy to reveal a polarization-dependent shift in absorption onset, transient absorption spectroscopy to uncover the excited state ultrafast dynamics, and polarization-resolved transient absorption microscopy to reveal polarization-dependent splitting of the exciton spectrum near the band edge.

3.4.1 Polarized linear absorption spectroscopy of nanowire bundles

The $CsPbBr_3$ nanowires were also found to display anisotropic optical properties. This was observed by measuring both the linear absorption and transient absorption of individual bundles with polarized light. Figure 3.10a shows the absorption spectrum of an individual bundle of 10 nm nanowires at several different optical polarizations collected in the transient absorption microscope using lamp light from a monochromator. Light was sent through a polarizer and half-wave plate, then first focused along the longitudinal (long) axis of the nanowires (0°). We observed that the spectrum is shifted toward lower energies. As the polarization is rotated toward the transverse (short) axis of the nanowires, the spectrum shifts higher in energy. To quantify this shift in absorption onset, we record the half-maximum

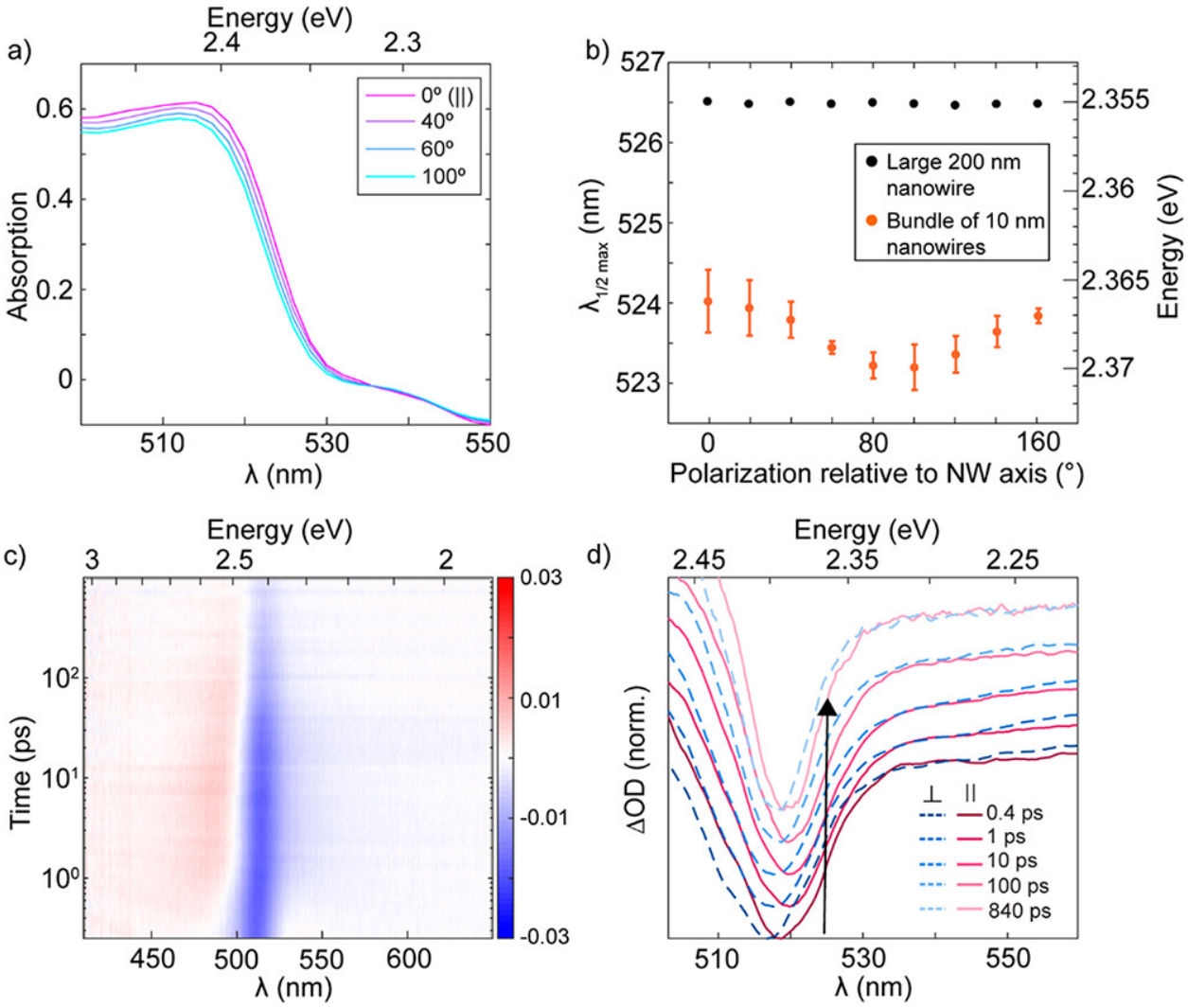

Figure 3.10: Polarization-resolved optical measurements of 10 nm diameter $CsPbBr_3$ nanowire bundles. (a) Local linear absorption spectra of a single bundle for several polarizations. (b) Absorption onset vs polarization (orange) showing oscillatory dependence. The polarization-resolved absorption onset for a large, 200 nm nanowire (black) shows no oscillation and is red-shifted. (c) Transient absorption (TA) map for 10 nm nanowire bundles in solution and (d) normalized TAM spectra at selected times for a single bundle with probe polarized along the longitudinal (pink) and transverse (blue) direction, showing a persistent shift of about 5–10 meV. The spectra are offset by delay time, for clarity, and the arrow is meant to guide the eye from the early time spectra, on the bottom, to the later-time spectra, on the top.

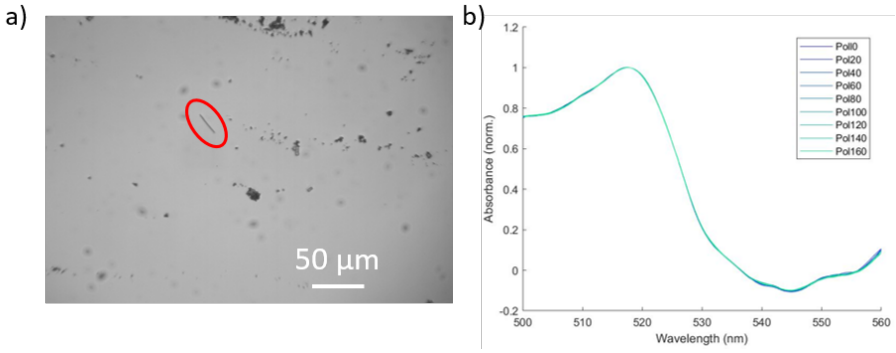

Figure 3.11: Polarization-resolved absorption measurement for a single nanowire. (a) A single large nanowire (circled in red), hundreds of nanometers in width and about 20 μm long. (b) Polarization-resolved absorption spectrum of that nanowire. 0° is defined as parallel to the long axis of the nanowire.

position of the absorption spectrum and plot it as a function of optical polarization in Figure 3.10b (orange points). Rotating the optical polarization from being parallel to perpendicular to the bundle shifts the absorption onset by 5 meV. Several bundles were studied, and all showed similar results. In order to verify that this finding is not an artifact of the imaging system, we performed the same measurement on a single large nanowire, about 200 nm in width and 20 μm long (Figure 3.11a). This object has roughly the same dimensions as a bundle, but it is not in the quantum confined regime. We find that the absorption onset, plotted in Figure 3.10b (black points) and Figure 3.11b, is lower in energy (matching bulk $CsPbBr_3$) and is isotropic. We conclude that in $CsPbBr_3$ nanowires, longitudinally polarized light excites states that are lower in energy than those excited by transverse polarized light. As detailed through the transient absorption (TA) measurements below, we attribute this effect to splitting of the band-edge exciton due to the long-range exchange interaction.

3.4.2 Transient absorption spectroscopy of nanowire bundles

Before describing polarization-resolved transient absorption microscopy (TAM) on nanowire bundles, we first establish that the ultrafast dynamics of $CsPbBr_3$ nanowire bundles are similar to those of other lead halide perovskites. For standard TA measurements, we use an 80 MHz mode-locked Ti:sapphire Coherent Vitara oscillator to create a seed pulse that is fed into a Coherent Legend-Elite regenerative amplifier to produce 800 nm pulses at 5 kHz. The output was split, with one line focused onto a CaF_2 plate to create the broadband probe. The other line was sent into a BBO crystal to produce 400 nm pump light, or into an optical parametric amplifier (Coherent OPerA Solo) to create 490 nm pump light. The pump and probe were focused onto the sample with curved mirrors, the pump was spatially filtered, and the probe was detected with an Ocean Optics USB4000 spectrometer. TA spectra of 10 nm nanowire bundles in solution are shown as a pseudocolor plot in Figure 3.11c. We also

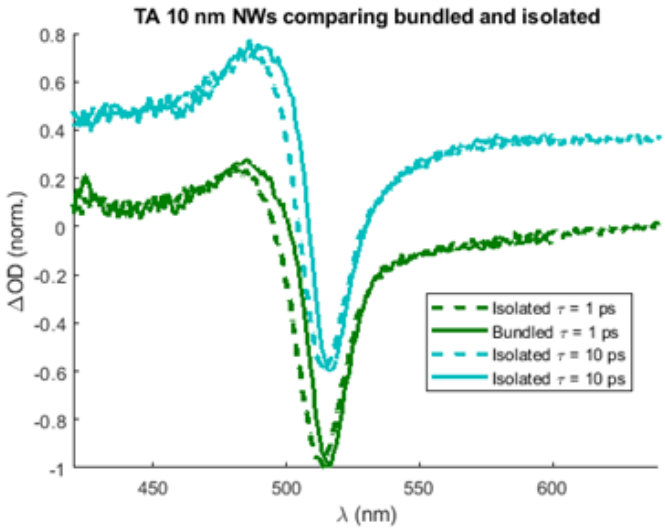

Figure 3.12: Normalized TA spectra of 10 nm $CsPbBr_3$ nanowires in solution, both bundled (solid curves) and isolated (dashed curves), at time delays 1 ps and 10 ps (offset for clarity). The timescales were found to be similar, and the spectra are identical up to a slight red-shift of the ground state bleach upon bundling. This is not surprising given the weak inter-nanowire coupling observed in stroboSCAT measurements.

studied isolated nanowires (Figure 3.12), and found nearly identical timescales and spectra, although bundling induces a slight red-shift (not unexpected, given the weak internanowire coupling deduced with stroboSCAT). We observe a prominent ground state bleach (GSB) with a low-energy tail and a photoinduced absorption (PIA) at higher energies. These features were introduced in Chapter 1.

To better visualize the spectra we used Glotaran [148] to fit the data to a four-stage sequential kinetic model: $A_1(\lambda) \xrightarrow{k_1} A_2(\lambda) \xrightarrow{k_2} A_3(\lambda) \xrightarrow{k_3} A_4(\lambda)$, where $A_i(\lambda)$ give the evolution associated spectra (EAS) as shown in Figure 3.13, and k_i is the rate constant for spectrum $A_i(\lambda)$ to evolve into $A_{j+1}(\lambda)$. The fourth EAS (blue curve in Figure 3.13a-b) has a lifetime much longer than the experimental time scale of 1 ns. We see that the initial spectrum (EAS 1 black curve in Figure 3.13a-b) has a high-energy tail and a sub-bandgap PIA feature. Both features are likely due to an initial hot carrier population, which bleaches above-gap transitions, and also causes bandgap renormalization, allowing for sub-bandgap absorption.[149] Both features disappear over the cooling time scale (from EAS 1-4 in Figure 3.13a-b), $1/k_1$ = 600 fs, which becomes slower for higher pump fluence (as expected for hot carrier cooling) [146, 150]. After the initial hot carrier cooling, the subsequent decay of the GSB can be fit to two exponentials, largely because of biexciton recombination, ascertained by plotting $1/\delta$OD vs delay time at the GSB wavelengths at multiple pump fluences (Figure 3.14). In the case of pure second order decay, this presents as a straight line,[151] which we observe initially, until linear decay channels become dominant and the line deviates. Figure 3.14 shows that

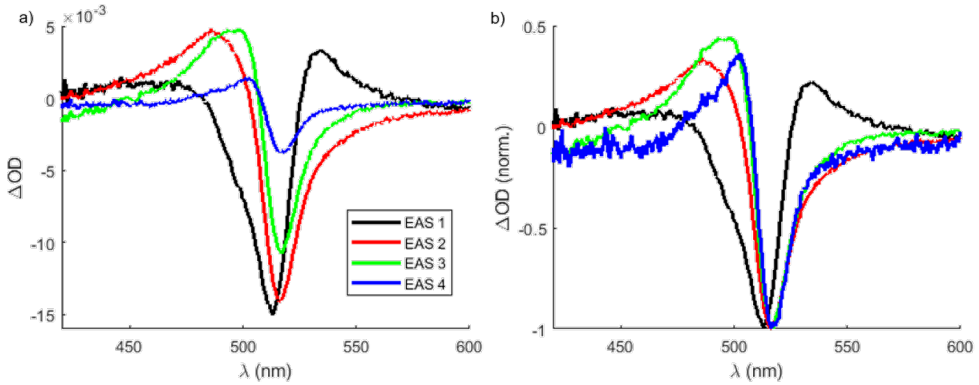

Figure 3.13: (a) Evolution association spectra (EAS) of TA measurements on 10 nm $CsPbBr_3$ nanowire bundles in solution. (b) Normalized EAS, in order to accentuate how the shape of the spectrum changes over time.

at 60 $\mu J/cm^2$, which is similar to the fluence used in the stroboSCAT experiments, biexciton recombination ceases after 100 ps, justifying our assertion that the diffusion measurements, which take place over a nanosecond time scale, are not significantly influenced by nonlinear recombination. The prominence of linear decay also indicates that the bulk of excited species are excitons, as charge carriers would decay bimolecularly.

There are two other notable features of the TA spectra. The first is the above-gap PIA, which is initially broad and sharpens with time. This has been observed before, [150] but as far as we know its spectral evolution has not been explained. The second is the broad subgap negative δOD signal. This has also been seen in methylammonium lead bromide, and was attributed to optical phonon-assisted subgap absorption [152]. We come to the same conclusion after ruling out two possible alternatives. One alternative possibility would be that there is decreased scattering in the excited state, but the negative contrast signal in our stroboSCAT measurements indicates that excitons in $CsPbBr_3$ make the material more polarizable, not less. Another possibility would be that the probe induces two-photon absorption, but we varied the probe fluence and found no change in the spectral shape.

3.4.3 Polarization-resolved transient absorption microscopy of nanowire bundles

Having concluded that $CsPbBr_3$ nanowires display dynamics similar to those of other lead halide perovskites, and that bundling does not impact the dynamics, we turn to polarization-resolved studies of individual bundles with TAM. The setup is similar to one described previously in our group, [153] except that broadband detection has also been implemented rather than employing a single-color probe. The pump and probe were combined with a beam splitter and focused on the sample through an objective lens with a numerical aperture of 0.70. After recollimating through a second objective lens after the sample, the

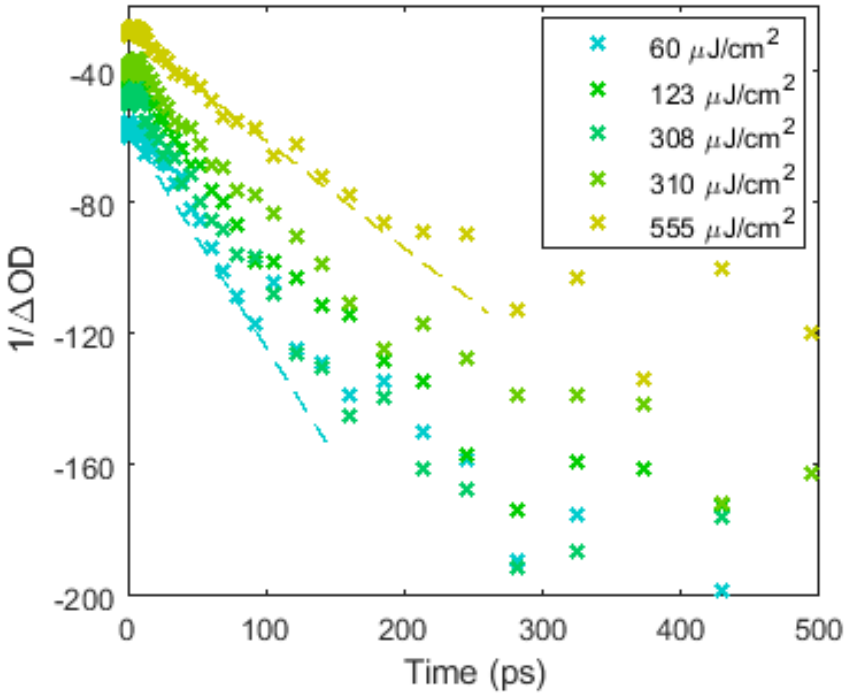

Figure 3.14: Inverse of the GSB signal as a function of time, for several pump fluences. Dashed lines guide the eye, and show that the data are roughly linear at early times, indicative of biexciton recombination.

pump was spectrally filtered and the probe was dispersed with a diffraction grating onto an Orion 2K Line Scan camera from Lightwise. In previous work, the ability to measure the probe polarization- and spatially dependent dynamics of anisotropic samples has revealed key details that are not visible in ensemble measurements.

Here we study ten different bundles and find that the TA dynamics are all similar, indicating that the bundles are homogeneous in structure and composition. Rotating the pump polarization is found to have no effect. However, we do find that rotating the probe polarization shifts the TA spectrum. Several normalized and offset TA spectra are shown in Figure 3.10d, for probe polarization parallel (pink) and perpendicular (blue) to the long axis of a nanowire bundle. They reveal a consistent shift of the GSB feature, which is higher in energy for perpendicular polarization than it is for parallel polarization. When the GSB peak is examined for the selected time delays shown in Figure 3.10d, the magnitude of the shift decreases from 10 meV at early delay times to 5 meV at later delay times, with an uncertainty of less than 1 meV. This is similar in magnitude to the shift seen in the linear absorption spectrum, which was 5 meV (Figure 3.10a,b), and this suggests that the entire exciton spectrum near the band edge experiences polarization-dependent splitting—those states with optical transition dipole moments (TDMs) along the short axis of the nanowire

are slightly higher in energy than those with TDMs along the long axis of the nanowire.

We attempted to repeat all optical experiments with bundles of 3 nm nanowires as well in order to investigate the effect of slightly stronger transverse confinement, but these species are much more fragile than 10 nm nanowires and degrade quickly under pulsed laser excitation. Although it is therefore not possible to quantify the size of any polarization-dependent shift in the spectral properties of nanowires with widths smaller than 10 nm at this time, we hypothesize that there would be a shift similar to or potentially even larger than what we observe for the 10 nm nanowires.

The observed polarization-dependent splitting might be expected if the crystal structure possessed uniaxial/tetragonal or approximately tetragonal symmetry. Indeed, our observation that the higher energy transition is polarized preferentially perpendicular to the nanowire axis is not inconsistent with previous measurements in tetragonal $CsPbBr_3$ nanocrystals, where a fine structure splitting of $\sim$1 meV was observed in between the exciton fine structure levels with angular momentum projection ±1 and 0 taken along the c-axis, with the ±1 levels, polarized perpendicular to the c-axis, being higher in energy, and the 0 level polarized parallel to it [141]. This could imply that nanowires adopt a lower symmetry unit cell with a symmetry axis oriented parallel to the nanowire, leading to anisotropic optical transitions associated with the different fine structure levels. Indeed, high resolution TEM measurements have shown that the 10 nm nanowires adopt a low-symmetry orthorhombic structure with growth along the nearly symmetric $\langle 110 \rangle$ axis [138]. However, as detailed below, we find that the magnitude of the splitting and relative ordering of the levels are best explained by long-range exchange acting in conjunction with two-dimensional confinement, and not by crystalline asymmetry. The optical polarization anisotropy is driven by shape anisotropy.

3.5 Polarized photoluminescence spectroscopy of nanowire bundles

We performed polarized PL measurements of the 10 nm nanowires in solution. As diagrammed in Figure 3.15a, the excitation laser at 465 nm was rotated to be polarized either vertically (V) or horizontally (H) in the lab frame. Emission was collected in a direction perpendicular to the excitation beam, with an emission polarizer rotated both vertically and horizontally, generating all possible combinations of the two orthogonal excitation and two orthogonal emission polarizations. Spectra collected in these four configurations are shown in Figure 3.15b, where the first letter of the legend indicates excitation polarization and the second letter indicates emission polarization. Anisotropy is evident, as the four curves are not identical, but this is not necessarily surprising.

In a nanowire geometry, classical electrodynamics dictates that both absorption and emission occur preferentially along the long axis, even if the TDM strength is isotropic [154, 155]. Specifically, the electric field for light polarized along the short axis of the nanowire

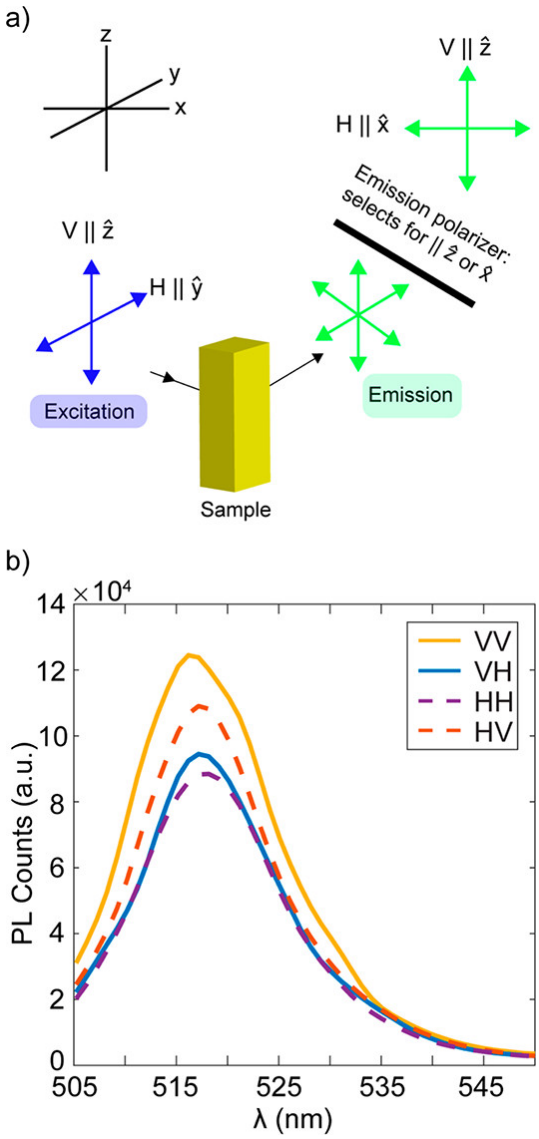

Figure 3.15: Polarization-dependent PL. (a) Schematic and (b) spectra of 10 nm diameter $CsPbBr_3$ nanowires in cyclohexane, excited at 465 nm. The first letter of the legend indicates the polarization of the excitation beam (vertical or horizontal) and the second letter indicates the polarization of the measured emission.

is reduced by $2\epsilon_{\mathrm{m}}/(\epsilon_{\mathrm{m}} + \epsilon_{\mathrm{nw}}(\omega_{\mathrm{ex}}))$, where ϵ_{m} is the surrounding medium dielectric constant and $\epsilon_{\mathrm{nw}}(\omega_{\mathrm{ex}})$ is the nanowire's dielectric constant as a function of light excitation at a given frequency. This reduction of the electric field is also true for light emitted at frequency ω_{em}. The nanowire excitation and emission can now be written in the following forms:

$$\begin{aligned} P(\omega_{\mathrm{ex}}) &= 1 + \kappa(\omega_{\mathrm{ex}})(\hat{c} \cdot \hat{e}_{\mathrm{ex}}) \\ P(\omega_{\mathrm{em}}) &= 1 + \kappa(\omega_{\mathrm{em}})(\hat{c} \cdot \hat{e}_{\mathrm{em}}) \\ \kappa(\omega) &= \frac{(\epsilon_{\mathrm{m}} + \epsilon_{\mathrm{nw}}(\omega))^2}{4\epsilon_{\mathrm{m}}^2} - 1 \end{aligned} \tag{3.11}$$

where $\hat{c}$ is the unit vector along the nanowire axis and $\hat{e}$ is the polarization of the exciting or emitted light. To calculate the intensity for a given configuration, such as I_{HV}, we fix the directions of $\hat{e}_{\mathrm{ex}}$ and $\hat{e}_{\mathrm{em}}$ and take the product of $P(\omega_{\mathrm{ex}})P(\omega_{\mathrm{em}})$. We also define the excitation propagation direction as $\hat{x}$, the emission propagation direction as $\hat{y}$, the vertical direction as $\hat{z}$, and the nanowire orientation is given by polar angle θ and azimuthal angle ϕ. The four intensities are:

$$\begin{aligned} I_{\mathrm{VV}} &= (1 + \kappa_{\mathrm{ex}} \cos^2\theta)(1 + \kappa_{\mathrm{em}} \cos^2\theta) \\ I_{\mathrm{VH}} &= (1 + \kappa_{\mathrm{ex}} \cos^2\theta)(1 + \kappa_{\mathrm{em}} \sin^2\theta \cos^2\phi) \\ I_{\mathrm{HV}} &= (1 + \kappa_{\mathrm{ex}} \sin^2\theta \sin^2\phi)(1 + \kappa_{\mathrm{em}} \cos^2\theta) \\ I_{\mathrm{HH}} &= (1 + \kappa_{\mathrm{ex}} \sin^2\theta sin^2\phi)(1 + \kappa_{\mathrm{em}} \sin^2\theta \cos^2\phi) \end{aligned} \tag{3.12}$$

For an isotropic distribution of nanowires we take the average over θ and ϕ and find that $I_{\mathrm{VV}} \geq I_{\mathrm{VH}} = I_{\mathrm{HV}} = I_{\mathrm{HH}}$ and we arrive at the following definition for anisotropy:

$$A = \frac{I_{\mathrm{VV}} - I_{\mathrm{VH}}}{I_{\mathrm{VV}} + I_{\mathrm{VH}}}, \tag{3.13}$$

which is also equivalent to

$$\frac{\kappa_{\mathrm{ex}}\kappa_{\mathrm{em}}}{15 + 5\kappa_{\mathrm{ex}} + 5\kappa_{\mathrm{em}} + 2\kappa_{\mathrm{ex}}\kappa_{\mathrm{em}}} \tag{3.14}$$

The magnitude of A depends on the dielectric constants of the nanowire [156] and the surroundings, where the optical frequency dielectric constant of cyclohexane, which is the solvent we use for unbundled 10 nm nanowires, is 2.02. The optical frequency dielectric constant of $CsPbBr_3$ is not well known, but computations indicate that it is about 5 [156]. Using this information we calculate that $A_{\mathrm{V}} = 0.09$, but we observe a value of 0.14, an increase of approximately 50%. Furthermore, if the optical transitions were isotropic we would expect the three intensities I_{VH}, I_{HV}, and I_{HH} to be identical, and that is not the case as seen in Figure 3.15b. We therefore consider that the absorption and emission TDMs are anisotropic, and the intensities will be modified in the following manner.

First, we let the TDM strength be $d_{||}$ for light polarized along the long-axis of the nanowire, and $d_{\perp}$ for light polarized along the short-axis of the nanowire, such that κ from Equation 3.14 is now written as:

$$\kappa(\omega) = \frac{d_{||}^2(\epsilon_{\mathrm{m}} + \epsilon_{\mathrm{nw}}(\omega))^2}{4d_{\perp}^2\epsilon_{\mathrm{m}}^2} - 1. \tag{3.15}$$

There is no further modification to κ since the TAM measurements indicate that the energy shift between states of different polarizations is only about 5 meV, which is small compared to the thermal energy at room temperature.

We also consider orientational anisotropy of the nanowires. Let the orientational distribution be isotropic in ϕ, but have some polar probability distribution function $f(\theta)$, where the normalization condition is $\int_0^{\pi/2} f(\theta)\sin(\theta)\,d\theta = 1$. We define the following moments of distribution as:

$$\begin{aligned} m_2 &\equiv \int_0^{\pi/2} f(\theta)\cos^2\theta\sin\theta d\theta \\ m_4 &\equiv \int_0^{\pi/2} f(\theta)\cos^4\theta\sin\theta d\theta, \end{aligned} \tag{3.16}$$

where for a uniform distribution $m_2 = 1/3$ and $m_4 = 1/5$. Now we can describe the emission intensities in the case of anisotropic TDMs as:

$$\begin{aligned} I_{\mathrm{VV}} &= 1 + \kappa_{\mathrm{ex}}m_2 + \kappa_{\mathrm{em}}m_2 + \kappa_{\mathrm{ex}}\kappa_{\mathrm{em}}m_4 \\ I_{\mathrm{VH}} &= 1 + \kappa_{\mathrm{ex}}m_2 + \kappa_{\mathrm{em}}\frac{1-m_2}{2} + \kappa_{\mathrm{ex}}\kappa_{\mathrm{em}}\frac{m_2-m_4}{2} \\ I_{\mathrm{HV}} &= 1 + \kappa_{\mathrm{ex}}\frac{1-m_2}{2} + \kappa_{\mathrm{em}}m_2 + \kappa_{\mathrm{ex}}\kappa_{\mathrm{em}}\frac{m_2-m_4}{2} \\ I_{\mathrm{HH}} &= 1 + \kappa_{\mathrm{ex}}\frac{1-m_2}{2} + \kappa_{\mathrm{em}}\frac{1-m_2}{2} + \kappa_{\mathrm{ex}}\kappa_{\mathrm{em}}\frac{1-2m_2+m_4}{8}. \end{aligned} \tag{3.17}$$

Now we can also consider the anisotropy between I_{VH} and I_{HV} as

$$A_{\mathrm{cross}} = \frac{I_{\mathrm{HV}} - I_{\mathrm{VH}}}{I_{\mathrm{HV}} + I_{\mathrm{VH}}} = \frac{3(\kappa_{\mathrm{em}} - \kappa_{\mathrm{ex}})(m_2 - 1/3)}{4 + (\kappa_{\mathrm{em}} + \kappa_{\mathrm{ex}})(1 + m_2) + 2\kappa_{\mathrm{ex}}\kappa_{\mathrm{em}}(m_2 - m_4)}. \tag{3.18}$$

Here, we note that the anisotropy is proportional to both $(\kappa_{\mathrm{em}} - \kappa_{\mathrm{ex}})$ and $(m_2 - 1/3)$, which implies that the fluorescence anisotropy between I_{VH} and I_{HV} that we observe in our measurements has orientational anisotropy and that there is a difference in κ for excitation and emission. Without further information about the orientation distribution of the nanowires, we cannot determine the magnitude of this difference but can consider the possible causes. It could be because ϵ_{nw} is a strong function of frequency, in which case the fact that excitation

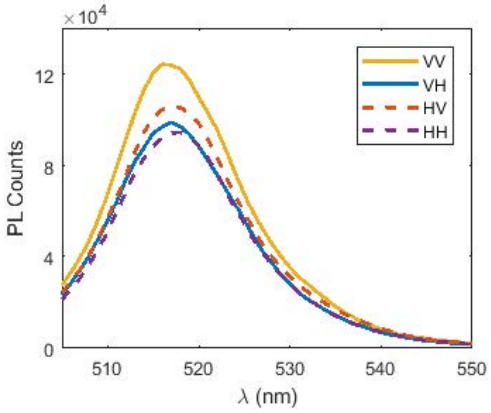

Figure 3.16: Polarized PL spectra of 10 nm diameter nanowires in cyclohexane at 408 nm excitation. The first letter of the legend indicates the polarization of the excitation beam (vertical or horizontal) and the second letter indicates the polarization of the measured emission. The anisotropy between VV and VH is 0.12, which is slightly less than what we measured when exciting at 465 nm, but still more than what we expect from purely electrodynamic effects.

and emission are at different frequencies would produce different values of κ. However, the amount of anisotropy is uniform in emission frequency, implying that anisotropic TDMs are the cause: $d_{||} \not\equiv d_{\perp}$. We cannot disentangle the effects of absorption and emission anisotropy, however repeating the measurement with 408 nm excitation light (Figure 3.16) results in a slightly different amount of anisotropy: $A_{\mathrm{V}} = 0.12$. This implies that anisotropy in the absorption TDM is at least partially responsible for our observations.

As a control measurement, we measure the time-resolved PL spectra of a small control molecule (a derivative of triphenylsulfonium) to account for variations in signal strength between the four polarization configurations. We found that rotating the emission polarizer did change the signal strength because the efficiency of light through the emission monochromator is wavelength and polarization dependent. The ratio of the control molecule's PL spectra for a vertically vs. horizontally aligned emission polarizer gives a correction factor, $G(\lambda)$, which we use to scale intensities for I_{HV} and I_{HH}.

We conclude that the absorption and emission TDMs are themselves anisotropic, possibly due to crystalline asymmetry, and also that the 10 nm nanowires are anisotropically oriented in solution although we cannot calculate the magnitude of the TDM anisotropy without knowing more about the orientational distribution of the nanowires.

We have found several examples of anisotropic behavior in $CsPbBr_3$ nanowires, all of which can be plausibly attributed to the shape of the nanowires or to an asymmetric crystal structure, as opposed to quantum confinement. Exciton transport appears to be driven by geometry, with the lack of internanowire coupling forcing excitons to diffuse primarily along the long axis of the nanowire bundles. The magnitude of the diffusivity, which is comparable to that seen in bulk $CsPbBr_3$, implies that transport is not intrinsically affected by weak confinement. We also observe polarization dependent splitting at the band edge, with

transverse polarized light coupling to a manifold of states about 5-10 meV higher in energy than those coupled to by longitudinally polarized light. This is qualitatively consistent with previous measurements in 8-10 nm sized nominally tetragonal $CsPbBr_3$ nanocrystals, where a fine structure splitting of $\sim$1 meV was observed between the exciton fine structure levels with angular momentum projection ±1 and 0 taken along the c-axis, with the ±1 levels being higher in energy [141, 142]. The interpretation originally given in refs [141] and [142] for the exciton fine structure level ordering in $CsPbBr_3$ nanocrystals was based on the assumption of cubic nanocrystal shape in conjunction with a negative intrinsic tetragonal crystal field splitting and the electron-hole exchange interaction [105, 141, 142]. However, calculations using density functional theory show that the crystal field in tetragonal $CsPbBr_3$ is positive, [105, 157] leading to a level order inconsistent with the experimentally observed fine structure. An alternative explanation for the observed fine structure, proposed in Reference [106], is connected with the effect of shape anisotropy via the long-range exchange interaction. In fact, $CsPbBr_3$ nanocrystals in the size range reported in References [141] and [142] have been shown to be elongated along the crystallographic c-axis by 20% [158]. Following Nestoklon *et al.*, [106] we find that long-range exchange acts in conjunction with the anisotropic shape to create a splitting between the exciton sublevels with the exciton whose TDM is parallel to the axis of elongation having lower energy than the exciton sublevels whose TDMs are parallel to the short axis [105, 106].

3.5.1 Modeling the effect of shape anisotropy on long-range exchange interaction

To explore this effect for nanowires, we modeled the nanowire as a rectangular prism with equal x and y (transverse) dimensions, L, but with an unequal z dimension, L_z. The long-range exchange energy of a given exciton state, X_i can be written in terms of the Coulomb energy of the polarization associated with the exciton state [159]:

$$H_{X_i} = \int\int_V \Big(-\vec{\nabla}_{\vec{r}_1} \cdot \vec{P}_{X_i}(\vec{r}_1)\Big)^* \frac{1}{\epsilon_\infty |\vec{r}_1 - \vec{r}_2|} \Big(-\vec{\nabla}_{\vec{r}_{21}} \cdot \vec{P}_{X_i}(\vec{r}_2)\Big). \tag{3.19}$$

Here, the exciton polarization is equal to the transition dipole density[105]:

$$\vec{P}_{X_i}(\vec{r}) = -i\frac{e\hbar}{m_o E_g} f(\vec{r_e}\vec{r_h}). \tag{3.20}$$

In this expression, $f(\vec{r}_e, \vec{r}_h)$ is the envelope function of the exciton, while $\vec{p}_{X_i}$ is its associated unit-cell-level transition dipole matrix element [105]. In the expressions above, E_g is the band gap, ϵ_∞ is the high frequency dielectric constant, and m_o is the free electron mass. Within the weak confinement regime, we calculate the long-range exchange energy of the exciton states whose transition dipole moment is polarized parallel to the axis of elongation (z) of the nanowire and do the same for the states whose TDMs are perpendicular to the axis of elongation. The envelope function for the ground exciton in the weak confinement regime is written, [105]

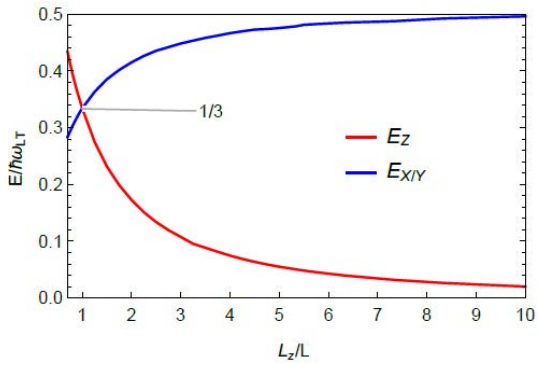

Figure 3.17: Long-range exchange energy for exciton sub-levels in a right rectangular prism of length L_z with transverse dimension L. For $L_z/L > 1$, the exciton sub level with transition dipole moment along z is lower in energy than the exciton sublevels with transversely polarized transition dipole moments. When $L_z/L = 1$, the energies of the three exciton sub-levels with transition dipole moments along x, y and z are degenerate and equal to $\hbar\omega_{LT}/3$.

$$f(\vec{r}_{\rm e}, \vec{r}_{\rm h}) = \phi_{\rm 1s}(0)\psi_{\rm g}(X, Y, Z). \tag{3.21}$$

Here $\phi_{\rm 1s}$ is the hydrogen ground state wavefunction in the electron-hole relative coordinate, while $\psi_{\rm g}$ is the ground center-of-mass envelope function for an exciton confined within a right rectangular prism with dimensions $L_x = L_y = L \neq L_z$. This is given in terms of the exciton's center-of-mass coordinates X, Y, Z as, [105]

$$\psi_g(X, Y, Z) = \left[\frac{8}{L^2 L_z}\right]^{(1/2)} \cos\left(\frac{\pi X}{L}\right) \cos\left(\frac{\pi Y}{L}\right) \cos\left(\frac{\pi Z}{L_z}\right). \tag{3.22}$$

We find that the exciton with transition dipole parallel to the axis of elongation (z) has lower energy than the exciton sublevels whose transition dipoles are parallel to the short axes. The resulting energies are plotted versus the ratio, L_z/L, over the range between the z-dimension of the nanowire, L_z, and the transverse dimension, L, of the nanowire in Figure 3.17.

The energy scale of the splitting is the longitudinal-transverse splitting of the bulk exciton, $\hbar\omega_{LT}$, where $\hbar\omega_{LT} = \frac{4}{3\epsilon_\infty a_x^3}\frac{E_p}{m_o}\left(\frac{\hbar e}{E_g}\right)^2$. In this expression, E_p is the Kane energy, E_g is the band gap, ϵ_∞ is the high frequency dielectric constant, m_o is the free electron mass, and a_x is the exciton Böhr radius. The value of the LT splitting in bulk $CsPbBr_3$ has recently been measured as $\hbar\omega_{LT} = 5.4$ meV [160]. Inspection of the plot shows that for large aspect ratios, $L_z/L \gg 1$, the splitting between the z exciton and the transverse excitons approaches $\hbar\omega_{LT}/2$, where $\hbar\omega_{LT}$ is the bulk longitudinal-transverse (LT) splitting, with the z-polarized exciton being lowest in energy, qualitatively consistent with the observed splitting obtained

from our nanowire measurements. However, our experimentally observed splitting values of ∼5 meV for nanowires seem unexpectedly close to the bulk value. How might this happen?

If we estimate the magnitude of the long-range exchange splitting in the weak confinement regime, we take into account the dielectric corrections to the long-range exchange that will drive the transverse exciton energy up by an amount proportional to $(\kappa - 1)/(\kappa + 1)$ owing to image charge effects, while the z exciton energy will not be impacted. Here, κ is the ratio of the dielectric constant inside the NW to that of the surrounding medium. Calculating the image charge effect for a cylindrical nanowire, [161] we estimate a 29% increase in the fine structure splitting for $\kappa = 2.5$, leading to a total splitting of ∼3.5 meV, which is larger than the limit of $\hbar\omega_{LT}/2$. In addition, it is expected that two-dimensional quantum confinement in the nanowire will enhance the exciton binding energy, which decreases the exciton Böhr radius, and as a result increases the value of $\hbar\omega_{LT}$ based on its definition. In this case, as the exciton binding energy increases and the exciton radius decreases, the exciton is pushed into the weak confinement regime where the splitting is essentially independent of the lateral size.

The Rashba model may also be considered for the weak confinement regime, where the level ordering is flipped since the Rashba contribution to the fine structure becomes larger than the exchange contribution [105, 119]. To describe the ∼5 meV splitting of the nanowires with this model, we would need to assume that the Rashba coefficient in nanowires is ∼2-3 times larger than that required to describe the ∼1 meV splitting in excitons in cube-shaped NCs; moreover, the direction of the inversion symmetry breaking would be required to be parallel to the nanowire axis.

The larger splitting, ∼5 meV, observed here is 40% larger than would be expected from the long-range exchange splitting in the weak confinement limit of ∼3.5 meV. This suggests that dielectric effects as well as possible enhancement of the exciton binding energy or enhanced quantum confinement effects in the nanowires may concomitantly increase the long-range exchange splitting energy relative to the bulk form or in nanocrystals. This combination of effects may also include an increase of the Rashba coefficient.

The anisotropic absorption or emission TDMs, which we infer from polarized fluorescence measurements in solution, could also be due to the shape asymmetry of the nanowires, or it could be due to crystalline asymmetry. Unfortunately, because a solution sample comprises many nanowires with different orientations, it is difficult to determine the strength or frequency-dependence of the TDM anisotropy. Studies of CdSe nanoplatelets find that band-edge emission is anisotropic while absorption high above the band edge is isotropic [162]. That could occur in $CsPbBr_3$ as well for high excitation frequency, but the fact that the strength of the anisotropy differs for 465 and 408 nm excitation (comparing Figure 3.15 to Figure 3.16) implies that neither of these wavelengths are in an isotropic absorption regime. In order to better understand the band-edge structure, polarization-resolved PL measurements of single bundles could be performed at low temperature, which would produce sharper emission peaks [163] and remove the confounding effect of nanowire bundle orientation [164]. Such measurements should be supplemented with electronic structure calculations [165] of $CsPbBr_3$ nanowires with various crystal structures and growth directions,

similar to calculations that have been done for near-cubic nanostructures [166].

3.6 Conclusion

We have used several techniques to investigate anisotropic behavior in $CsPbBr_3$ nanowires: stroboSCAT to track exciton diffusion, TA to measure the ultrafast dynamics, local absorption microscopy to measure the polarization-resolved optical coupling to the ground state, TA microscopy to measure the polarization-resolved optical coupling to excited states, and polarized fluorescence to interrogate TDM anisotropy. We observe rapid exciton diffusion along the nanowires' long axis, weak internanowire coupling, and what we take to be an extremely low trap density. Combined with the TA measurements, we see $CsPbBr_3$ nanowires as potential active materials for concentrated photovoltaic applications, in which large exciton densities must be sustained and rapidly transported to an interface for exciton dissociation. From TA we also learn that bundling does not impact nanowire dynamics. The ability to retain their unique character in a complex environment makes $CsPbBr_3$ nanowires a potential building block of tunable electronics that combine several nanostructures to produce novel behaviors [167].

We have also made several measurements pertinent to the band-edge electronic structure of $CsPbBr_3$ nanowires. Using local absorption and TAM, we found that the nanowires display anisotropic optical coupling; the band-edge transition is slightly lower for light polarized along the long nanowire axis than it is for light polarized along the short nanowire axes. Furthermore, polarized fluorescence indicates that the strength of the transition dipole moments is anisotropic as well. These results are qualitatively consistent with splitting of the band-edge exciton due to the long-range exchange interaction in conjunction with the shape anisotropy of the nanowire. The measured splitting is larger than would be expected using bulk exciton parameters, which suggests that enhancement of the exciton binding energy due the 1D effects and dielectric confinement play a role in the splitting. Polarization-resolved PL measurements of single nanowire bundles at low temperature could in the future resolve some of the questions raised herein.

Chapter 4

Conclusions

Multimodal characterization enables multiscale insight into the hierarchical nature of complex semiconducting materials. These techniques span the Å to nanometer to micron length scales to probe crystal structure arrangements and defects, grain size and boundaries, and device scales. Merging this information across modalities reveals significant relationships across the spatial and energetic landscapes and the impact of processing conditions for semiconductors.

Chapter 1 provided the background for organic semiconductor properties, device applications, thin film processing methods, and crystalline microstructures. We also discussed the advantages and limitations of a variety of characterization techniques along with the information they provide to assist in selecting an appropriate subset for multimodal studies.

Chapter 2 covered the multimodal imaging characterization of a hybrid crystalline microstructure in rubrene thin films. Atomic force microscopy images and X-ray scattering provided initial morphological and crystal structure characterization of the films. Scanning transmission X-ray microscopy revealed and quantified the disappearance of orientational discontinuities in the hybrid crystalline microstructure made possible with multiple scales for fields-of-view. The higher spatial resolution of 4D-scanning transmission electron microscopy corroborated this observation through orientation maps acquired from diffraction patterns at each spatial point. Dynamic polarized optical microscopy tracked rubrene crystallization on glass/ITO substrates, which led to two important findings: the existence of a finite substrate thermalization rate during annealing and Arrhenius behavior for rubrene crystallization. We used the Arrhenius behavior to extrapolate the crystallization dynamics on SiN substrates, and as a result, we mapped the approximate temperature of the sample during crystallization at which the orientational discontinuity disappears. This temperature was consistent with those used in our annealing protocols for crystallizing single crystalline domains to spherulite morphologies. We discussed future directions to extend this multimodal study of rubrene and generally organic semiconductor thin films. The ideas covered charge-transport studies and comparing the molecular arrangement of different organic semiconductors capable of forming crystalline and polycrystalline structures.

Chapter 3 described how optical pump-probe microscopies provided invaluable insight on

understanding the effects of shape anistoropy of inorganic lead halide perovskite ($CsPbBr_3$) nanowires and nanowire bundles on their dynamics. Stroboscopic interferometric scattering microscopy imaged exciton diffusion along the long-axis of nanowire bundles and suggested a low-trap density via modeling. Local polarized absorption microscopy, bulk transient absorption, and transient absorption microscopy showed that these nanowire bundles displayed anisotropic optical properties, where the band edge splits so that states with transition dipole moments parallel to the short-axis of the nanowires exhibit higher energies. Polarized fluorescence measurements also showed that the strengths of the transition dipole moments were also anisotropic. Modeling the optical anisotropic properties of the nanowires supported the hypothesis that shape anisotropy combined with long-range exchange led to the energy-state splittings. In the future, polarized fluoresence measurements at low temperatures could provide more insight into the band structure.

Together, these studies demonstrate the scope of multimodal characterization approaches for understanding semiconducting materials. We integrated complementary microscopies, spectroscopies, and X-ray scattering techniques to dissect the multiscale structure-function properties of organic and perovskite semiconductors in crystalline, polycrystalline, and confined morphologies. Multimodal studies will continue to offer invaluable insight on emerging semiconductors and other classes of materials, so that they can be reliably incorporated into existing and novel technologies.

Bibliography

(1) Callister Jr., W. D.; Rethwisch, D. G., *Materials Science and Engineering: An Introduction*, 9th; John Wiley & Sons, Inc.: 2014.

(2) Folie, B. D.; Tan, J. A.; Huang, J.; Sercel, P. C.; Delor, M.; Lai, M.; Lyons, J. L.; Bernstein, N.; Efros, A. L.; Yang, P.; Ginsberg, N. S. *J. Phys. Chem. A* **2020**, *124*, 1867–1876.

(3) Wang, C.; Dong, H.; Jiang, L.; Hu, W. *Chem. Soc. Rev.* **2018**, *47*, Publisher: The Royal Society of Chemistry, 422–500.

(4) Mas-Torrent, M.; Rovira, C. *Chem. Rev.* **2011**, *111*, Publisher: American Chemical Society, 4833–4856.

(5) Bao, Z.; Locklin, J., *Organic Field-Effect Transistors*; Taylor and Francis Group: 2007.

(6) Ginsberg, N. S.; Tisdale, W. A. *Annual Review of Physical Chemistry* **2020**, *71*, 1–30.

(7) Wang, S.-J.; Sawatzki, M.; Darbandy, G.; Talnack, F.; Vahland, J.; Malfois, M.; Kloes, A.; Mannsfeld, S.; Kleemann, H.; Leo, K. *Nature* **2022**, *606*, 700–705.

(8) Kippelen, B.; Brédas, J.-L. *Energy & Environmental Science* **2009**, *2*, Publisher: Royal Society of Chemistry, 251–261.

(9) Podzorov, V.; Pudalov, V. M.; Gershenson, M. E. *Appl. Phys. Lett.* **2003**, *82*, 1739–1741.

(10) Higgins, M. Chemical Vapor Deposition Benefits and Limitations `https://www.silcotek.com/blog/chemical-vapor-deposition-benefits-and-limitations` (accessed 07/28/2022).

(11) Costa, J. C. S.; Rocha, R. M.; Vaz, I. C. M.; Torres, M. C.; Mendes, A.; Santos, L. M. N. B. F. *J. Chem. Eng. Data* **2015**, *60*, Publisher: American Chemical Society, 3776–3791.

(12) Hiszpanski, A. M.; Baur, R. M.; Kim, B.; Tremblay, N. J.; Nuckolls, C.; Woll, A. R.; Loo, Y.-L. *J. Am. Chem. Soc.* **2014**, *136*, Publisher: American Chemical Society, 15749–15756.

(13) Dalal, S. S.; Walters, D. M.; Lyubimov, I.; de Pablo, J. J.; Ediger, M. D. *Proceedings of the National Academy of Sciences* **2015**, *112*, Publisher: Proceedings of the National Academy of Sciences, 4227–4232.

(14) M. Hiszpanski, A.; Loo, Y.-L. *Energy & Environmental Science* **2014**, *7*, Publisher: Royal Society of Chemistry, 592–608.

(15) Hiszpanski, A. M.; Lee, S. S.; Wang, H.; Woll, A. R.; Nuckolls, C.; Loo, Y.-L. *ACS Nano* **2013**, *7*, Publisher: American Chemical Society, 294–300.

(16) Diao, Y.; Shaw, L.; Bao, Z.; B. Mannsfeld, S. C. *Energy & Environmental Science* **2014**, *7*, Publisher: Royal Society of Chemistry, 2145–2159.

(17) Virkar, A. A.; Mannsfeld, S.; Bao, Z.; Stingelin, N. *Advanced Materials* **2010**, *22*, 3857–3875.

(18) Lee, S. S.; Kim, C. S.; Gomez, E. D.; Purushothaman, B.; Toney, M. F.; Wang, C.; Hexemer, A.; Anthony, J. E.; Loo, Y.-L. *Advanced Materials* **2009**, *21*, 3605–3609.

(19) Riera-Galindo, S.; Tamayo, A.; Mas-Torrent, M. *ACS Omega* **2018**, *3*, Publisher: American Chemical Society, 2329–2339.

(20) Walter, L. S.; Axt, A.; Borchert, J. W.; Kammerbauer, T.; Winterer, F.; Lenz, J.; Weber, S. A. L.; Weitz, R. T. *Small*, *n/a*, 2200605.

(21) Diao, Y.; Tee, B. C.-K.; Giri, G.; Xu, J.; Kim, D. H.; Becerril, H. A.; Stoltenberg, R. M.; Lee, T. H.; Xue, G.; Mannsfeld, S. C. B.; Bao, Z. *Nature Mater* **2013**, *12*, Number: 7 Publisher: Nature Publishing Group, 665–671.

(22) Fusella, M. A.; Yang, S.; Abbasi, K.; Choi, H. H.; Yao, Z.; Podzorov, V.; Avishai, A.; Rand, B. P. *Chem. Mater.* **2017**, *29*, Publisher: American Chemical Society, 6666–6673.

(23) Lee, S. S.; Mativetsky, J. M.; Loth, M. A.; Anthony, J. E.; Loo, Y.-L. *ACS Nano* **2012**, *6*, Publisher: American Chemical Society, 9879–9886.

(24) Lee, S. S.; Loth, M. A.; Anthony, J. E.; Loo, Y.-L. *J. Am. Chem. Soc.* **2012**, *134*, Publisher: American Chemical Society, 5436–5439.

(25) Shtukenberg, A. G.; Punin, Y. O.; Gunn, E.; Kahr, B. *Chem. Rev.* **2012**, *112*, Publisher: American Chemical Society, 1805–1838.

(26) Gránásy, L.; Pusztai, T.; Tegze, G.; Warren, J. A.; Douglas, J. F. *Phys. Rev. E* **2005**, *72*, Publisher: American Physical Society, 011605.

(27) Folie, B. Extremely Small and Incredibly Fast: Combining Spectroscopy and Microscopy to Reveal Local Excited State Dynamics in Disordered Semiconductors, Ph.D. Thesis, Berkeley, California: University of California, Berkeley, 2018, 277 pp.

(28) Belianinov, A.; Ievlev, A. V.; Lorenz, M.; Borodinov, N.; Doughty, B.; Kalinin, S. V.; Fernández, F. M.; Ovchinnikova, O. S. *ACS Nano* **2018**, *12*, Publisher: American Chemical Society, 11798–11818.

(29) Raja, P. M.; Barron, A. R. 8.2: Transmission Electron Microscopy, Chemistry LibreTexts `https://chem.libretexts.org/Bookshelves/Analytical_Chemistry/Physical_Methods_in_Chemistry_and_Nano_Science_(Barron)/08%3A_Structure_at_the_Nano_Scale/8.02%3A_Transmission_Electron_Microscopy` (accessed 07/24/2022).

(30) Spence, J. C. H. *Structural Dynamics* **2017**, *4*, Publisher: American Institute of Physics, 044027.

(31) Interaction between incident electrons and matters, Practical Electron Microscopy and Database `https://www.globalsino.com/EM/page3768.html` (accessed 07/24/2022).

(32) Comparison between X-ray and electron diffractions, Practical Electron Microscopy and Database `https://www.globalsino.com/EM/page3497.html` (accessed 07/24/2022).

(33) Henderson, R. *Quarterly Reviews of Biophysics* **1995**, *28*, Publisher: Cambridge University Press, 171–193.

(34) Rivnay, J.; Mannsfeld, S. C. B.; Miller, C. E.; Salleo, A.; Toney, M. F. *Chem. Rev.* **2012**, *112*, 5488–5519.

(35) Attwood, D., *Soft X-Rays and Extreme Ultraviolet Radiation: Principles and Applications*; Cambridge University Press: Cambridge, 1999.

(36) Critical angle - GISAXS, GISAXS Community Website `http://gisaxs.com/index.php/Critical_angle` (accessed 07/20/2022).

(37) Gullikson, E. Look up Elemental X-Ray Properties, The Center for X-ray Optics `https://henke.lbl.gov/optical_constants/pert_form.html` (accessed 07/20/2022).

(38) Liu, F.; Gu, Y.; Shen, X.; Ferdous, S.; Wang, H.-W.; Russell, T. P. *Progress in Polymer Science* **2013**, *38*, 1990–2052.

(39) Chabinyc, M. L. *Polymer Reviews* **2008**, *48*, 463–492.

(40) Sherman, J. B.; Chiu, C.-Y.; Fagenson, R.; Wu, G.; Hawker, C. J.; Chabinyc, M. L. *MRS Communications* **2015**, *5*, Publisher: Cambridge University Press, 447–452.

(41) S. Radchenko, E.; V. Anokhin, D.; L. Gerasimov, K.; I. Rodygin, A.; A. Rychkov, A.; D. Shabratova, E.; Grigorian, S.; A. Ivanov, D. *Soft Matter* **2018**, *14*, Publisher: Royal Society of Chemistry, 2560–2566.

(42) Tamura, N. ALS X-ray microdiffraction BL12.3.2 `https://sites.google.com/a/lbl.gov/bl12-3-2/home` (accessed 07/21/2022).

(43) Tamura, N.; Gilbert, P. U. P. A. In *Methods in Enzymology*, De Yoreo, J. J., Ed.; Research Methods in Biomineralization Science, Vol. 532; Academic Press: 2013, pp 501–531.

(44) Stöhr, J. NEXAFS Spectroscopy, NEXAFS Spectroscopy https://www-ssrl.slac.stanford.edu/stohr/nexafs.htm (accessed 07/22/2022).

(45) Hitchcock, A. P. *J Synchrotron Rad* **2001**, *8*, Number: 2 Publisher: International Union of Crystallography, 66–71.

(46) Li, X. Transmission Electron Microscope https://www.unl.edu/ncmn-cfem/xzli/em/temoptic.htm (accessed 07/22/2022).

(47) Bollmeyer, M.; Li, B. Transmission electron microscopy (TEM): TEM versus STEM and HAADF, Chemistry LibreTexts https://chem.libretexts.org/Courses/Franklin_and_Marshall_College/Introduction_to_Materials_Characterization__CHM_412_Collaborative_Text/Electron_and_Probe_Microscopy/Transmission_electron_microscopy_(TEM)%3A_TEM_versus_STEM_and_HAADF (accessed 07/22/2022).

(48) Bustillo, K. C.; Zeltmann, S. E.; Chen, M.; Donohue, J.; Ciston, J.; Ophus, C.; Minor, A. M. *Acc. Chem. Res.* **2021**, *54*, Publisher: American Chemical Society, 2543–2551.

(49) Ophus, C. *Microscopy and Microanalysis* **2019**, *25*, Publisher: Cambridge University Press, 563–582.

(50) Stroppa, D. 4D STEM: A Basic Overview and the Latest Developments, Dectris https://www.dectris.com/company/news/blog/electron-microscopy/4d-stem-and-hybrid-pixel-electron-detectors/ (accessed 08/05/2022).

(51) What is TEM/STEM Standard and Aberration Corrected ? — Core Facilities, Arizona State University https://cores.research.asu.edu/materials/what-temstem-standard-and-aberration-corrected (accessed 08/05/2022).

(52) 4D Scanning Transmission Electron Microscopy: Unraveling an Exciting Technique, AZoM.com Section: Materials Article, https://www.azom.com/article.aspx?ArticleID=21728 (accessed 08/05/2022).

(53) Savitzky, B. H. et al. *Microscopy and Microanalysis* **2021**, *27*, Publisher: Cambridge University Press, 712–743.

(54) Ophus, C.; Zeltmann, S. E.; Bruefach, A.; Rakowski, A.; Savitzky, B. H.; Minor, A. M.; Scott, M. C. *Microscopy and Microanalysis* **2022**, Publisher: Cambridge University Press, 1–14.

(55) Voigtländer, B., *Scanning Probe Microscopy*, 1st ed.; NanoScience and Technology 1434-4904; Springer Berlin, Heidelberg: 2015.

(56) Bang, J. J.; Russell, S. R.; Rupp, K. K.; Claridge, S. A. *Anal. Methods* **2015**, *7*, Publisher: The Royal Society of Chemistry, 7106–7127.

(57) Hunter, S.; Chen, J.; Anthopoulos, T. D. *Advanced Functional Materials* **2014**, *24*, 5969–5976.

(58) Mochizuki, S.; Uruma, T.; Satoh, N.; Saravanan, S.; Soga, T. *Jpn. J. Appl. Phys.* **2017**, *56*, Publisher: IOP Publishing, 08LB08.

(59) Jones, A. C.; Kearns, N. M.; Bohlmann Kunz, M.; Flach, J. T.; Zanni, M. T. *J. Phys. Chem. A* **2019**, *123*, Publisher: American Chemical Society, 10824–10836.

(60) Atkin, J. M.; Berweger, S.; Jones, A. C.; Raschke, M. B. *Advances in Physics* **2012**, *61*, 745–842.

(61) Centrone, A. *Annual Review of Analytical Chemistry* **2015**, *8*, 101–126.

(62) Rao, V. J.; Matthiesen, M.; Goetz, K. P.; Huck, C.; Yim, C.; Siris, R.; Han, J.; Hahn, S.; Bunz, U. H. F.; Dreuw, A.; Duesberg, G. S.; Pucci, A.; Zaumseil, J. *J. Phys. Chem. C* **2020**, *124*, Publisher: American Chemical Society, 5331–5344.

(63) Muller, E. A.; Pollard, B.; Raschke, M. B. *J. Phys. Chem. Lett.* **2015**, *6*, Publisher: American Chemical Society, 1275–1284.

(64) Polarized Light Microscopy, Nikon's MicroscopyU `https://www.microscopyu.com/techniques/polarized-light/polarized-light-microscopy` (accessed 07/14/2022).

(65) Fesenko, P.; Rolin, C.; Janneck, R.; Bommanaboyena, S. P.; Gaethje, H.; Heremans, P.; Genoe, J. *Organic Electronics* **2016**, *37*, 100–107.

(66) Hattori, Y.; Kitamura, M. *ACS Appl. Mater. Interfaces* **2020**, *12*, Publisher: American Chemical Society, 36428–36436.

(67) Irkhin, P.; Ryasnyanskiy, A.; Koehler, M.; Biaggio, I. *Phys. Rev. B* **2012**, *86*, Publisher: American Physical Society, 085143.

(68) Deng, S.; Blach, D. D.; Jin, L.; Huang, L. *Advanced Energy Materials* **2020**, *10*, _eprint: https://onlinelibrary.wiley.com/doi/pdf/10.1002/aenm.201903781, 1903781.

(69) Zhu, T.; Snaider, J. M.; Yuan, L.; Huang, L. *Annual Review of Physical Chemistry* **2019**, *70*, 219–244.

(70) Wong, C. Y.; Folie, B. D.; Cotts, B. L.; Ginsberg, N. S. *J. Phys. Chem. Lett.* **2015**, *6*, 3155–3162.

(71) Long, Y.; Chung, T.-F.; Kuc, A.; Wan, Y.; Xu, Y.; Chen, Y. P.; Heine, T.; Huang, L. *Science Advances* **2018**, *4*, e1700324.

(72) Delor, M.; Weaver, H. L.; Yu, Q.; Ginsberg, N. S. *Nat. Mater.* **2020**, *19*, Number: 1 Publisher: Nature Publishing Group, 56–62.

(73) Foggiatto, A. L.; Takeichi, Y.; Ono, K.; Suga, H.; Takahashi, Y.; Fusella, M. A.; Dull, J. T.; Rand, B. P.; Kutsukake, K.; Sakurai, T. *Organic Electronics* **2019**, *74*, 315–320.

(74) Hailey, A. K.; Wang, S.-Y.; Chen, Y.; Payne, M. M.; Anthony, J. E.; Podzorov, V.; Loo, Y.-L. *Advanced Functional Materials* **2015**, *25*, 5662–5668.

(75) Hiszpanski, A. M.; Khlyabich, P. P.; Loo, Y.-L. *MRS Communications* **2015**, *5*, 407–421.

(76) Podzorov, V.; Menard, E.; Borissov, A.; Kiryukhin, V.; Rogers, J. A.; Gershenson, M. E. *Phys. Rev. Lett.* **2004**, *93*, 086602.

(77) Anthony, J. E. *Chem. Rev.* **2006**, *106*, Publisher: American Chemical Society, 5028–5048.

(78) Salleo, A.; Kline, R. J.; DeLongchamp, D. M.; Chabinyc, M. L. *Advanced Materials* **2010**, *22*, 3812–3838.

(79) Groves, C.; Reid, O. G.; Ginger, D. S. *Acc. Chem. Res.* **2010**, *43*, Publisher: American Chemical Society, 612–620.

(80) Eichhorn, J.; Reyes-Lillo, S. E.; Roychoudhury, S.; Sallis, S.; Weis, J.; Larson, D. M.; Cooper, J. K.; Sharp, I. D.; Prendergast, D.; Toma, F. M. *Small* **2020**, *16*, 2001600.

(81) Collins, B. A.; Ade, H. *Journal of Electron Spectroscopy and Related Phenomena* **2012**, *185*, 119–128.

(82) McNeill, C. R.; Watts, B.; Thomsen, L.; Ade, H.; Greenham, N. C.; Dastoor, P. C. *Macromolecules* **2007**, *40*, Publisher: American Chemical Society, 3263–3270.

(83) Wen, Y.; Liu, Y.; Guo, Y.; Yu, G.; Hu, W. *Chem. Rev.* **2011**, *111*, Publisher: American Chemical Society, 3358–3406.

(84) Panova, O.; Ophus, C.; Takacs, C. J.; Bustillo, K. C.; Balhorn, L.; Salleo, A.; Balsara, N.; Minor, A. M. *Nat. Mater.* **2019**, *18*, 860–865.

(85) Fielitz, T. R.; Holmes, R. J. *Crystal Growth & Design* **2016**, *16*, Publisher: American Chemical Society, 4720–4726.

(86) Jo, P. S.; Duong, D. T.; Park, J.; Sinclair, R.; Salleo, A. *Chem. Mater.* **2015**, *27*, 3979–3987.

(87) Sun, Y.; Kearns, K. L.; Ediger, M. D.; Yu, L. *PNAS* **2011**, *108*, 5990–5995.

(88) Dönges, S. A.; Cline, R. P.; Zeltmann, S. E.; Nishida, J.; Metzger, B.; Minor, A. M.; Eaves, J. D.; Raschke, M. B. *Nano Lett.* **2021**, *21*, Publisher: American Chemical Society, 6463–6470.

(89) Khatib, O.; Bechtel, H. A.; Martin, M. C.; Raschke, M. B.; Carr, G. L. *ACS Photonics* **2018**, *5*, Publisher: American Chemical Society, 2773–2779.

(90) Schindelin, J. et al. *Nat Methods* **2012**, *9*, Number: 7 Publisher: Nature Publishing Group, 676–682.

(91) Park, S.-W.; Choi, J.-M.; Lee, K. H.; Yeom, H. W.; Im, S.; Lee, Y. K. *J. Phys. Chem. B* **2010**, *114*, Publisher: American Chemical Society, 5661–5665.

(92) Belfiore, L. A. In *Physical properties of macromolecules*, 1st; John Wiley & Sons, Inc.: 2010.

(93) Young, R. J.; Lovell, P. A., *Introduction to Polymers*, Third; CRC Press: 2011.

(94) Jukes, P. C.; Das, A.; Durell, M.; Trolley, D.; Higgins, A. M.; Geoghegan, M.; Macdonald, J. E.; Jones, R. A. L.; Brown, S.; Thompson, P. *Macromolecules* **2005**, *38*, Publisher: American Chemical Society, 2315–2320.

(95) Kim, J. H.; Jang, J.; Zin, W.-C. *Macromolecular Rapid Communications* **2001**, *22*, 386–389.

(96) Park, C.-J.; Park, H. J.; Lee, J. Y.; Kim, J.; Lee, C.-H.; Joo, J. *ACS Appl. Mater. Interfaces* **2018**, *10*, Publisher: American Chemical Society, 29848–29856.

(97) Liu, F.; Chow, W. L.; He, X.; Hu, P.; Zheng, S.; Wang, X.; Zhou, J.; Fu, Q.; Fu, W.; Yu, P.; Zeng, Q.; Fan, H. J.; Tay, B. K.; Kloc, C.; Liu, Z. *Advanced Functional Materials* **2015**, *25*, 5865–5871.

(98) Jariwala, D.; Marks, T. J.; Hersam, M. C. *Nature Mater* **2017**, *16*, Number: 2 Publisher: Nature Publishing Group, 170–181.

(99) Russ, B.; Glaudell, A.; Urban, J. J.; Chabinyc, M. L.; Segalman, R. A. *Nat Rev Mater* **2016**, *1*, Number: 10 Publisher: Nature Publishing Group, 1–14.

(100) Guo, Z.; Wan, Y.; Yang, M.; Snaider, J.; Zhu, K.; Huang, L. *Science* **2017**, *356*, 59–62.

(101) Ma, L.; Zhang, K.; Kloc, C.; Sun, H.; Michel-Beyerle, M. E.; Gurzadyan, G. G. *Phys. Chem. Chem. Phys.* **2012**, *14*, Publisher: The Royal Society of Chemistry, 8307–8312.

(102) Wu, T.; Ni, W.; G. Gurzadyan, G.; Sun, L. *RSC Advances* **2021**, *11*, Publisher: Royal Society of Chemistry, 4639–4645.

(103) Breen, I.; Tempelaar, R.; Bizimana, L. A.; Kloss, B.; Reichman, D. R.; Turner, D. B. *J. Am. Chem. Soc.* **2017**, *139*, Publisher: American Chemical Society, 11745–11751.

(104) Dull, J. T.; Wang, Y.; Johnson, H.; Shayegan, K.; Shapiro, E.; Priestley, R. D.; Geerts, Y. H.; Rand, B. P. *J. Phys. Chem. C* **2020**, *124*, Publisher: American Chemical Society, 27213–27221.

(105) Sercel, P. C.; Lyons, J. L.; Wickramaratne, D.; Vaxenburg, R.; Bernstein, N.; Efros, A. L. *Nano Letters* **2019**, acs.nanolett.9b01467.

(106) Nestoklon, M. O.; Goupalov, S. V.; Dzhioev, R. I.; Ken, O. S.; Korenev, V. L.; Kusrayev, Y. G.; Sapega, V. F.; De Weerd, C.; Gomez, L.; Gregorkiewicz, T.; Lin, J.; Suenaga, K.; Fujiwara, Y.; Matyushkin, L. B.; Yassievich, I. N. *Physical Review B* **2018**, *97*, 1–10.

(107) Shabaev, A.; Efros, A. L. *Nano Letters* **2004**, *4*, 1821–1825.

(108) Polavarapu, L.; Nickel, B.; Feldmann, J.; Urban, A. S. *Advanced Energy Materials* **2017**, *7*, 1700267.

(109) Chen, H.; Xiang, S.; Li, W.; Liu, H.; Zhu, L.; Yang, S. *Solar RRL* **2018**, *6*, 1700188.

(110) Fu, Y.; Zhu, H.; Stoumpos, C. C.; Ding, Q.; Wang, J.; Kanatzidis, M. G.; Zhu, X.; Jin, S. *ACS Nano* **2016**, *10*, 7963–7972.

(111) Wang, Y.; Li, X.; Song, J.; Xiao, L.; Zeng, H.; Sun, H. *Advanced Materials* **2015**, *27*, 7101–7108.

(112) Raja, S. N.; Bekenstein, Y.; Koc, M. A.; Fischer, S.; Zhang, D.; Lin, L.; Ritchie, R. O.; Yang, P.; Alivisatos, P. *ACS Applied Materials & Interfaces* **2016**, *8*, acsami.6b09443.

(113) Li, X.; Cao, F.; Yu, D.; Chen, J.; Sun, Z.; Shen, Y.; Zhu, Y.; Wang, L.; Wei, Y.; Wu, Y.; Zeng, H. *Small* **2017**, *13*, 1603996.

(114) Zhang, J.; Bai, D.; Jin, Z.; Bian, H.; Wang, K.; Sun, J.; Wang, Q.; Liu, S. F. *Advanced Energy Materials* **2018**, *1703246*, 1703246.

(115) Eaton, S. W.; Lai, M.; Gibson, N. A.; Wong, A. B.; Dou, L.; Ma, J.; Wang, L.-W.; Leone, S. R.; Yang, P. *Proceedings of the National Academy of Sciences* **2016**, *113*, 1993.

(116) Zhang, D.; Yang, Y.; Bekenstein, Y.; Yu, Y.; Gibson, N. A.; Wong, A. B.; Eaton, S. W.; Kornienko, N.; Kong, Q.; Lai, M.; Alivisatos, A. P.; Leone, S. R.; Yang, P. *Journal of the American Chemical Society* **2016**, *138*, 7236–7239.

(117) Zhou, Y.; Luo, J.; Zhao, Y.; Ge, C.; Wang, C.; Gao, L.; Zhang, C.; Hu, M.; Niu, G.; Tang, J. *Advanced Optical Materials* **2018**, *1800679*, 1800679.

(118) Chen, Q. et al. *Nature* **2018**, *561*, Publisher: Springer US, 88–93.

(119) Becker, M. A. et al. *Nature* **2018**, *553*, 189–193.

(120) Zhang, D.; Yu, Y.; Bekenstein, Y.; Wong, A. B.; Alivisatos, A. P.; Yang, P. *Journal of the American Chemical Society* **2016**, *138*, 13155–13158.

(121) Bekenstein, Y.; Koscher, B. A.; Eaton, S. W.; Yang, P.; Alivisatos, A. P. *Journal of the American Chemical Society* **2015**, *137*, 16008–16011.

(122) Ravi, V. K.; Swarnkar, A.; Chakraborty, R.; Nag, A. *Nanotechnology* **2016**, *27*, DOI: 10.1088/0957-4484/27/32/325708.

(123) Shamsi, J.; Urban, A. S.; Imran, M.; De Trizio, L.; Manna, L. *Chem. Rev.* **2019**, *119*, Publisher: American Chemical Society, 3296–3348.

(124) Yarita, N.; Tahara, H.; Ihara, T.; Kawawaki, T.; Sato, R.; Saruyama, M.; Teranishi, T.; Kanemitsu, Y. *Journal of Physical Chemistry Letters* **2017**, *8*, 1413–1418.

(125) Castaneda, J. A.; Nagamine, G.; Yassitepe, E.; Bonato, L. G.; Voznyy, O.; Hoogland, S.; Nogueira, A. F.; Sargent, E. H.; Cruz, C. H. B.; Padilha, L. A. *ACS Nano* **2016**, *10*, 8603–8609.

(126) Gibson, N. A.; Koscher, B. A.; Alivisatos, A. P.; Leone, S. R. *Journal of Physical Chemistry C* **2018**, *122*, 12106–12113.

(127) Di Stasio, F.; Imran, M.; Akkerman, Q. A.; Prato, M.; Manna, L.; Krahne, R. *Journal of Physical Chemistry Letters* **2017**, *8*, 2725–2729.

(128) Zhu, Q.; Karlsson, K. F.; Pelucchi, E.; Kapon, E. *Nano Letters* **2007**, *7*, 2227–2233.

(129) Htoon, H.; Hollingsworth, J. A.; Dickerson, R.; Klimov, V. I. *Physical Review Letters* **2003**, *91*, 1–4.

(130) Blancon, J. C. et al. *Science* **2017**, *355*, 1288–1292.

(131) Sercel, P.; Vahala, K. *Physical Review B* **1991**, *44*, 5681–5691.

(132) Guo, Z.; Manser, J. S.; Wan, Y.; Kamat, P. V.; Huang, L. *Nat Commun* **2015**, *6*, Number: 1 Publisher: Nature Publishing Group, 7471.

(133) Delport, G.; Macpherson, S.; Stranks, S. D. *Advanced Energy Materials* **2020**, *10*, 1903814.

(134) Dey, A. et al. *ACS Nano* **2021**, *15*, Publisher: American Chemical Society, 10775–10981.

(135) Grumstrup, E. M.; Gabriel, M. M.; Cating, E. E. M.; Van Goethem, E. M.; Papanikolas, J. M. *Chemical Physics* **2015**, *458*, 30–40.

(136) Fang, Q.; Shang, Q.; Zhao, L.; Wang, R.; Zhang, Z.; Yang, P.; Sui, X.; Qiu, X.; Liu, X.; Zhang, Q.; Zhang, Y. *Journal of Physical Chemistry Letters* **2018**, *9*, 1655–1662.

(137) Zhang, Y.; Liu, J.; Wang, Z.; Xue, Y.; Ou, Q.; Polavarapu, L.; Zheng, J.; Qi, X.; Bao, Q. *Chemical Communications* **2016**, *52*, 13637–13655.

(138) Zhang, D.; Eaton, S. W.; Yu, Y.; Dou, L.; Yang, P. *Journal of the American Chemical Society* **2015**, *137*, 9230–9233.

(139) Imran, M.; Di Stasio, F.; Dang, Z.; Canale, C.; Khan, A. H.; Shamsi, J.; Brescia, R.; Prato, M.; Manna, L. *Chemistry of Materials* **2016**, *28*, 6450–6454.

(140) Ten Brinck, S.; Infante, I. *ACS Energy Letters* **2016**, *1*, 1266–1272.

(141) Fu, M.; Tamarat, P.; Huang, H.; Even, J.; Rogach, A. L.; Lounis, B. *Nano Letters* **2017**, *17*, 2895–2901.

(142) Ramade, J.; Andriambariarijaona, L. M.; Steinmetz, V.; Goubet, N.; Legrand, L.; Barisien, T.; Bernardot, F.; Testelin, C.; Lhuillier, E.; Bramati, A.; Chamarro, M. *Nanoscale* **2018**, *10*, Publisher: Royal Society of Chemistry, 6393–6401.

(143) Protesescu, L.; Yakunin, S.; Bodnarchuk, M. I.; Krieg, F.; Caputo, R.; Hendon, C. H.; Yang, R. X.; Walsh, A.; Kovalenko, M. V. *Nano Letters* **2015**, *15*, 3692–3696.

(144) Ekimov, A. I.; Onushchenko, A. A.; Plyukhin, A. G. **1985**, 7.

(145) Penwell, S. B.; Ginsberg, L. D.; Noriega, R.; Ginsberg, N. S. *Nature Materials* **2017**, *16*, 1136–1141.

(146) Fu, J.; Xu, Q.; Han, G.; Wu, B.; Huan, C. H. A.; Leek, M. L.; Sum, T. C. *Nature Communications* **2017**, *8*, DOI: 10.1038/s41467-017-01360-3.

(147) Tian, W.; Zhao, C.; Leng, J.; Cui, R.; Jin, S. *Journal of the American Chemical Society* **2015**, *137*, 12458–12461.

(148) Snellenburg, J. J.; Laptenok, S. P.; Seger, R.; Mullen, K. M.; van Stokkum, I. H. M. *Journal of Statistical Software* **2012**, *49*, 1–22.

(149) Price, M. B.; Butkus, J.; Jellicoe, T. C.; Sadhanala, A.; Briane, A.; Halpert, J. E.; Broch, K.; Hodgkiss, J. M.; Friend, R. H.; Deschler, F. *Nature Communications* **2015**, *6*, 1–8.

(150) Mondal, N.; Samanta, A. *Nanoscale* **2017**, *9*, Publisher: Royal Society of Chemistry, 1878–1885.

(151) Manser, J. S.; Kamat, P. V. *Nat. Photonics* **2014**, *8*, 737–743.

(152) Telfah, H.; Jamhawi, A.; Teunis, M. B.; Sardar, R.; Liu, J. *Journal of Physical Chemistry C* **2017**, *121*, 28556–28565.

(153) Folie, B. D.; Haber, J. B.; Refaely-Abramson, S.; Neaton, J. B.; Ginsberg, N. S. *Journal of the American Chemical Society* **2018**, *140*, 2326–2335.

(154) Ruda, H. E.; Shik, A. *Physical Review B* **2005**, *72*, 115308.

(155) Efros, A. L.; Rosen, M.; Averboukh, B.; Kovalev, D.; Ben-Chorin, M.; Koch, F. *Physical Review B - Condensed Matter and Materials Physics* **1997**, *56*, 3875–3884.

(156) Maqbool, M.; Rehman, G.; Ali, L.; Shafiq, M.; Iqbal, R.; Ahmad, R.; Khan, T.; Jalali-Asadabadi, S.; Maqbool, M.; Ahmad, I. *Journal of Alloys and Compounds* **2017**, *705*, 828–839.

(157) Sercel, P. C.; Lyons, J. L.; Bernstein, N.; Efros, A. L. *Journal of Chemical Physics* **2019**, *151*, 234106.

(158) Bertolotti, F.; Protesescu, L.; Kovalenko, M. V.; Yakunin, S.; Cervellino, A.; Billinge, S. J.; Terban, M. W.; Pedersen, J. S.; Masciocchi, N.; Guagliardi, A. *ACS Nano* **2017**, *11*, 3819–3831.

(159) Cho, K. *J. Phys. Soc. Jpn.* **1999**, *68*, Publisher: The Physical Society of Japan, 683–691.

(160) Belykh, V. V.; Yakovlev, D. R.; Glazov, M. M.; Grigoryev, P. S.; Hussain, M.; Rautert, J.; Dirin, D. N.; Kovalenko, M. V.; Bayer, M. *Nat Commun* **2019**, *10*, Number: 1 Publisher: Nature Publishing Group, 673.

(161) Cui, S. T. *Molecular Physics* **2006**, *104*, 2993–3001.

(162) Ma, X.; Diroll, B. T.; Cho, W.; Fedin, I.; Schaller, R. D.; Talapin, D. V.; Wiederrecht, G. P. *Nano Letters* **2018**, *18*, Publisher: American Chemical Society, 4647–4652.

(163) Diroll, B.; Zhou, H.; Schaller, R. *Advanced Functional Materials* **2018**, *3*, 1–7.

(164) Täuber, D.; Dobrovolsky, A.; Camacho, R.; Scheblykin, I. G. *Nano Letters* **2016**, *16*, 5087–5094.

(165) Berger, R. F. *Chemistry - A European Journal* **2018**, *24*, 8708–8716.

(166) Ben Aich, R.; Saïdi, I.; Ben Radhia, S.; Boujdaria, K.; Barisien, T.; Legrand, L.; Bernardot, F.; Chamarro, M.; Testelin, C. *Physical Review Applied* **2019**, *11*, Publisher: American Physical Society, 034042.

(167) Chen, J.-S.; Doane, T. L.; Li, M.; Zang, H.; Maye, M. M.; Cotlet, M. *Particle & Particle Systems Characterization* **2017**, *1700310*, 1700310.

Appendix A

Code for analyzing STXM images

To generate radial intensity profiles in STXM images, the following two scripts were used in Matlab. The first script houses input parameters for the radial_intensity function and loops through the output of the radial_intensity function to generate intensity radial profiles that can also be converted to orientation.

```
radial_distance = 1:5:50;
radial_distance = radial_distance';
stdmean_intensity2 = [];
n = length(radial_distance);
image = vhnorm;
image_center = [121,126];
bin_width = 25;
angle = 153;
% Imin = r115_fit.b;
% Imax = r115_fit.a;

mean_intensity = zeros(n,1);
stdmean_intensity1 = zeros(n,1);
theta_avg_output = zeros(n,1);
theta_avg_stderror = zeros(n,1);
pix_bin = zeros(n,1);

for i = 1:n
    radius = radial_distance(i);
    [mean_intensity(i),stdmean_intensity1(i)] = radial_intensity(image,
   image_center,radius,bin_width,angle);%,Imin,Imax);
end
figure; errorbar(radial_distance,mean_intensity,stdmean_intensity1,'.','
   markersize',15,'Capsize',3,'Linewidth',0.1)
xlabel('radial distance \mum'); ylabel('mean pixel count');

num_angles = length(angle);
if num_angles == 1
    title(sprintf('mean pixel count at %d degrees; width = %d pixel,
   stdev1',angle,bin_width));
```

```
28 elseif num_angles > 1
29     title(sprintf('mean pixel count at %d - %d degrees; width = %d pixel,
       stdev1',angle(1),angle(num_angles),bin_width));
30 end
31
32 N = length(mean_intensity);
33 colorMap = [zeros(N, 1), zeros(N, 1), ones(N,1)];
34
35 % % If y > 0.5, make the markers red.
36 % for k = 1 : length(mean_intensity)
37 %   if mean_intensity(k) > r115_fit.a || mean_intensity(k) <r115_fit.b
38 %     colorMap(k, :) = [1,0,0]; % Red
39 %   else
40 %     colorMap(k, :) = [0,0,1]; % Blue
41 %   end
42 % end
43 % figure; scatter(radial_distance,theta_avg_output,[],colorMap);
44 % figure; errorbar(radial_distance,theta_avg_output,theta_avg_stderror);
45 % xlabel('radial distance \mum'); ylabel('\theta crystal');
46 %
47 % figure; plot(radial_distance,pix_bin,'o');
48
49
50 %% convert intensity into orientation
51 inner_expression = (mean_intensity - Imin)./(Imax-Imin);
52 inner_expr_sqrt = sqrt(inner_expression);
53 %theta_complex = asind(inner_expr_sqrt)-0;
54 theta_degrees = abs(asind(inner_expr_sqrt)-90);
55 theta_real = real(theta_degrees);
56 if angle >=1 && angle <= 90
57     theta_real = theta_real;
58 elseif angle >= 91 && angle <=180
59     theta_real = -theta_real+180;
60 elseif angle >= 181 && angle <= 270
61     theta_real = theta_real+ 180;
62 else angle >= 271 && angle <= 359
63     theta_real = -theta_real + 360;
64 end
65 theta_real;
66
67 N = length(mean_intensity);
68 colorMap = [zeros(N, 1), zeros(N, 1), ones(N,1)];
69
70 % If y > 0.5, make the markers red.
71 for k = 1 : length(mean_intensity)
72   if mean_intensity(k) > Imax || mean_intensity(k) <Imin
73     colorMap(k, :) = [1,0,0]; % Red
74   else
75     colorMap(k, :) = [0,0,1]; % Blue
76   end
```

```
77 end
78 figure; scatter(radial_distance,theta_real,[],colorMap);
79
80 % error conversion
81
82 rss_60 = sum((theta_degrees-60).^2);%figure; plot(radial_distance,
   theta_degrees,'o');
```

The radial_intensity function essentially yields an average intensity at a single radii and radial vector. The input parameters include: the STXM image, defining the image center (using ImageJ to find the pixel coordinates), identifying the radius of interest, defining the radial width for pixel averaging, and identifying the angle of interest. Briefly, the function generates arrays of corresponding distances and angles for the image. Then, the pixels that fall under the radius of interest and the radial width are binned under corresponding radial vector angles. The average pixel intensity for each bin is calculated, and the intensity of the desired angle is given as the output. This function also contains the general concepts for generating annular linecuts for a given radii.

```
1  function [intensity_angle,intensity_std_error,accumarray_linecut,
     theta_array] = radial_intensity(image,image_center,radius,bin_width,
     angle)%,Imin,Imax)
2            [x_array,y_array] = meshgrid(1:size(image,2),1:size(image,1));
3            x_shift = x_array - image_center(1);
4            y_shift = y_array - image_center(2);
5            radius_array = sqrt((x_shift).^2 + (y_shift).^2); % values in
     pixels
6            theta_array = -atan2d(y_shift,x_shift) + 360*(-y_shift<0);%
     Converts into degrees
7            theta_array = abs(theta_array); % 180 degrees is negative
8            % because y_shift is 0, but I can't just add 360 because then
     I
9            % won't have 0 degrees in theta_array
10           shot_noise_array = sqrt(image);
11           radius_pixel = radius/0.5; % REMEMBER TO CHANGE PIXEL-TO-
     LENGTH (um) CONVERSION FOR DIFFERENT IMAGES
12
13           min_value = radius_pixel - (bin_width/2);
14           max_value = radius_pixel + (bin_width/2);
15           angle_low = angle - 1e-2;
16           angle_high = angle + 1e-2;
17
18           raw_radial_slice = theta_array(radius_array > min_value  &
     radius_array < max_value);
19           gray_counts = image(radius_array > min_value & radius_array <
     max_value);
20           shot_noise = shot_noise_array(radius_array > min_value &
     radius_array < max_value);
21
22           % Calculate the average pixel intensity at a given angle
23           % Bin pixels by angle
```

```
24              degrees_spacing = linspace(1,360,360)'; % whole degree = 360;
    half degree increments = 719; 1/4 degree increments = 1437
25              length(degrees_spacing);
26              raw_radial_slice(raw_radial_slice == 0) = 360;
27              raw_radial_slice(raw_radial_slice < 1) = 1;
28              [pix_bin,~,idx] = histcounts(raw_radial_slice,degrees_spacing)
    ;
29              pix_bin_angle = pix_bin(angle);
30
31              % Calculate the average pixel intensity and std error of the
32              % mean
33              accumarray_linecut = accumarray(idx(:),gray_counts,[],@mean);
34              accumarray_stdev = accumarray(idx(:),gray_counts,[],@std);
35              accumarray_std_error = accumarray_stdev./sqrt(pix_bin)';
36
37              num_angles = length(angle);
38              intensity_angle = [];
39              intensity_std_error = [];
40              theta_avg_output = [];
41              theta_avg_stderror = [];
42
43              if num_angles == 1
44                  intensity_angle = accumarray_linecut(angle);
45                  % mean_radial_intensity = mean(radial_intensity,'all')
46                  intensity_std_error = accumarray_std_error(angle);
47                  %intensity_std_error = round(intensity_std_error,1);
48  %                 theta_avg_output = theta_degrees_avg(angle);
49  %                 theta_avg_stderror = theta_degrees_stderror(angle);
50  %                 theta_avg_stderror = round(theta_avg_stderror,1);
51              elseif num_angles > 1
52                  for i = 1:num_angles
53                      intensity_angle = intensity_angle + accumarray_linecut
    (angle(i));
54                      intensity_std_error = (intensity_std_error +
    accumarray_stdev(angle(i)));
55  %                       theta_avg_output = theta_avg_output +
    theta_degrees_avg(angle(i));
56  %                       theta_avg_stderror = theta_avg_stderror +
    theta_degrees_stderror(angle(i));
57                  end
58                  intensity_angle = intensity_angle/num_angles;
59                  intensity_std_error = intensity_std_error/num_angles;
60                  intensity_std_error = round(intensity_std_error,1);
61  %                 theta_avg_output = theta_avg_output/num_angles;
62  %                 theta_avg_stderror = theta_avg_stderror/num_angles;
63  %                 theta_avg_stderror = round(theta_avg_stderror,1);
64              end
65
66
67          end
```

Appendix B

Code for tracking spherulite growth in dynamic polarized optical measurements

Jakhangirkhodja Tulyagankhodjaev developed the following code to analyze movies collected from dynamic polarized optical microscopy measurements as a summer student in our research group. The complete procedure is outlined in the guide: BoundaryTracking_RadialAnalysis.pdf. The first part of the script focuses on converting colored images of a growing structure of interest into binary images that generate outlines of the growing structure and generating a log of the centroid of each structure in a given frame. The second part of the script uses the outlines and the centroid log to measure the radius of each frame for a stack of images (i.e., over time).

B.1 Part 1: Code for background subtraction and binarization with ImageJ

The following scripts were generated by using the macro recorder in ImageJ, so it can be adapted, or one can record one's own steps. The following script (Dynamic_BackgroundSubtract.ijm) is for a frame stack (e.g., multiple images) from a video.

B.1.1 Multiple images binarization

The below script is originally from an ImageJ Macro, which is the reason for the specific color coding. Active code begins on line 10.

```
1 //Manual background subtract for image stacks
2 //This code is nearly identical to the manual background subtract for
     static images but modified to work for image stacks
```

```
3  //REQUIRED INPUTS: Have an image stack with interpolated ROI's in the ROI
       manager.
4
5  //The final output is a bunch of boundary images saved into a folder named
       with the timestamp in the MetaData as well as a .txt file of
       measurements on every image
6  //While all of the images will be saved, the output is an image stack
       showing you the movie of boundary moving, which is NOT saved, but also
       not necessary to save it is just a check.
7
8
9  //This part requests the user to pick the save point
10 filename = File.name;
11
12 roilist = roiManager("count");
13 finalsave = getDirectory("File Destination?");
14
15 for (i = 0; i<roilist; i++){
16   //This "clicks" on a window to make it the active one
17   //MANDATORY USER INPUT: You're gonna need to manually change the
       windowname to whatever is the open .avi file.
18   windowname = "name.avi";
19   selectWindow(windowname);
20   setSlice(i+1);
21
22   //This part requests time information
23   time = getMetadata("Info");
24
25   //Runs measurements
26   //USER INPUT: If you want or don't want these measurements, feel free to
       add or take away from them
27   roiManager("select", i);
28   List.setMeasurements;
29   x = List.getValue("X");
30   y = List.getValue("Y");
31   circ = List.getValue("Circ.");
32   area = List.getValue("Area");
33   roundness = List.getValue("Round");
34   feret = List.getValue("Feret");
35   FeretX = List.getValue("FeretX");
36   FeretY = List.getValue("FeretY");
37   FeretAngle = List.getValue("FeretAngle");
38   minFeret = List.getValue("MinFeret");
39
40   //White Pixel Boost
41   //USER INPUT: Adjust the value (0-255) if there is failure in
       thresholding
42   run("Add...", "value=130 slice");
43
44   // This calculates the average value of the background
```

```
45    run("Make Inverse");
46    getStatistics(area, mean, min, max, std, histogram);
47
48    //This prepares the background
49    heig = getHeight();
50    wid = getWidth();
51    setForegroundColor(mean, mean, mean);
52    newImage("Background", "8-bit white", wid, heig, 1);
53    floodFill(0,0);
54
55    //This subtracts the two images off from one another
56    imageCalculator("Subtract", windowname, "Background");
57    close("Background");
58
59    //Apply a threshold
60    //USER INPUT: Adjust the threhold bound if there is a failure in
       threholding
61    setThreshold(0, 47);
62    run("Convert to Mask", "method=Default background=Dark only");
63
64    //Analyze Particles
65    //USER INPUT: Adjust the "size" value to change the minimum area of
       space that is considered a "particle"
66    run("Analyze Particles...", "size=400-Infinity show=[Bare Outlines]
       clear");
67    rename(time);
68
69
70    //This inverts colors and saves the file
71    selectWindow(time);
72    run("Invert LUT");
73    saveAs("Tiff", finalsave+time);
74
75    print(time);
76    print("Center: ("+x+", "+y+")\nCircularity: "+circ+ "\nArea: "+area+"\
       nRoundness: "
77       +roundness+"\nFeret: "+feret+"\nFeret X: "+FeretX+"\nFeret Y: "+FeretY
       +"\nFeret Angle :"+FeretAngle+"\nMin. Feret: "+ minFeret);
78
79
80  }
81
82  selectWindow("Log");
83    saveAs("text", finalsave+"MeasurementLog");
84    close("Log");
85
86  run("Images to Stack");
```

B.1.2 Single images binarization

One can use the following two scripts to test the binarization method on a single image. They were also generated from an ImageJ Macro.

```
//Autocrop and AutoSave System for Static Images

//You need to have selections with the ROI manager before running this short script


//This part requests the user to provide the save file path. I don't believe it requires direct modification of the code.
filepath = getDirectory("image");
filename = File.name;


for (i = 0; i<roiManager("count"); i++){
  open(filepath+filename);
  roiManager("select", i);
  roiManager("Rename", "crop_"+i);
  run("Crop");
  saveAs("Tiff", filepath+"crop_"+i);
}

selectWindow("ImageJ");
```

```
//This code applys the manual background subtract to static images
//It is intended for use with the autocrop function, hence the bounds on the for loop are adjusted for it.
//REQUIRED INPUTS: Have autocropped images and draw selections around your objects, having inputted each one into the ROI manager.

//The final output of this macro is a boundary image and a .txt file recording the list of measurements regarding the selection itself.

//This requests your input when the macro runs
roilist = getNumber("How many selections are there?: ", roilist);
finalsave = getDirectory("File Destination?");

for (i = roilist; i<2*roilist; i++){
  // This "clicks" on a window to make it the active one
  windowname = "crop_" + (i-roilist)+".tif";
  selectWindow(windowname);

  //Runs measurements
  //USER INPUT: If you want or don't want these measurements, feel free to add or take away from them
  roiManager("select", i);
  List.setMeasurements;
  x = List.getValue("X");
```

```
21  y = List.getValue("Y");
22  circ = List.getValue("Circ.");
23  area = List.getValue("Area");
24  roundness = List.getValue("Round");
25  feret = List.getValue("Feret");
26  FeretX = List.getValue("FeretX");
27  FeretY = List.getValue("FeretY");
28  FeretAngle = List.getValue("FeretAngle");
29  minFeret = List.getValue("MinFeret");
30
31  //White Pixel Boost
32  //USER INPUT: Adjust the value (0-255) if there is failure in
     thresholding
33  run("Add...", "value=130");
34
35  //This calculates the average value of the background
36  run("Make Inverse");
37  getStatistics(area, mean, min, max, std, histogram);
38
39  //This prepares the background
40  heig = getHeight();
41  wid = getWidth();
42  setForegroundColor(mean, mean, mean);
43  newImage("Background", "8-bit white", wid, heig, 1);
44  floodFill(0,0);
45
46  //This subtracts the two images off from one another
47  imageCalculator("Subtract create", windowname, "Background");
48  midstepoutputname = windowname+"_midstep";
49  rename(midstepoutputname);
50  close("Background");
51
52  //Apply a threshold
53  //USER INPUT: Adjust the threhold bound if there is a failure in
     threholding
54  setThreshold(11, 255);
55  setOption("BlackBackground", false);
56  run("Convert to Mask");
57
58
59  //Analyze Particles
60  //USER INPUT: Adjust the "size" value to change the minimum area of
     space that is considered a "particle"
61  run("Analyze Particles...", "size=400-Infinity show=[Bare Outlines]
     clear");
62  drawoutputname = windowname+"_outline";
63  rename(drawoutputname);
64
65  //This creates an output that asks if the fit looks any good
66  selectWindow(windowname);
```

```
  run("Revert");
  run("Select None");
  run("Add Image...", "image="+drawoutputname+" x=0 y=0 opacity=25");

  prompt = getBoolean("Does the fit look good?");

    if (prompt == 1){
      //Invert LUT and Saves Outline
      selectWindow(drawoutputname);
      run("Invert LUT");
      saveAs("Tiff", finalsave+"draw_"+(i-roilist)+"_"+x+"_"+y);

      //Creating Output File
      print(windowname + "\nGood Fit? YES " + "\nAverage value of
   background is: " + mean);
      print("Center: ("+x+", "+y+")\nCircularity: "+circ+ "\nArea: "+area
   +"\nRoundness: "
        +roundness+"\nFeret: "+feret+"\nFeret X: "+FeretX+"\nFeret Y: "+
   FeretY+"\nFeret Angle :"+FeretAngle+"\nMin. Feret: "+ minFeret);
      selectWindow("Log");
      saveAs("text", finalsave+"draw_"+(i-roilist));
      close("Log");

      //Revert original image and keep it open
      selectWindow(windowname);
      run("Revert");
      selectWindow("draw_"+(i-roilist)+"_"+x+"_"+y+".tif");
    } else{
      //Revert original image, keep it open, but close the image outline
   for examination
      selectWindow(windowname);
      run("Revert");
      close("draw_"+(i-roilist)+".tif");
    }


    //Close intermediate files
    close(midstepoutputname);
    close(drawoutputname);

}
```

B.2 Part 2: Radial tracking with Python

B.2.1 Multiple images radial tracking

Below is the python notebook (in script form) that uses the inputs of the stack of binarized outlines and corresponding centroids to generate the radius size per frame.

```
# Average "radius" vs. time function for image stacks.
#This code requires primarily one input from the user and that
# is the "centerpoint" variable currently set up as (y,x).

#Depending on the files sitting in the folder, multiple centers may
# be needed. This is important for moments in a video in which one is
# travelling around. To do this, you have to turn the center into an
# array and modify the for loop to take the [ith] instant of the for loop.

#The idea is to bin the data weighted by pixel values. From that,
# the remainder of the function simply prepares data arrays.

#Make sure the timestamps have the same number of digits in the
# values i.e. 01, 02, ..., 09, 10, 11. etc.
import os
import sys
import glob
import numpy as np
import matplotlib.pyplot as plt

#This is the primary function
def radial_profile(data, center):
    x = np.indices((data.shape))[0]
    y = np.indices((data.shape))[1]
    r = np.sqrt((x - center[0])**2 + (y - center[1])**2)
    r = r.astype(np.int)

    radialprofile = np.bincount(r.ravel(), data.ravel())

    return radialprofile


#USER INPUT: Input values as (y,x)
centerpoint = (1090, 832);


filelist = glob.glob("*.tif");
numimages = len(filelist);


#Prepares the time array by reading timestamps
box = []
timearray=np.array(box, dtype = np.float32)

for i in range(0, len(filelist)):

    timestamp = float(filelist[i][0:5])
    timearray = np.append(timearray, timestamp)


```

```
#Prepares the average radius array.
distancearray = np.array(box)

for i in range(0, numimages):

    #Normalize Image so every white pixel is 1 instead of 255.
    img = plt.imread(filelist[i])[...,0]*(1/255)
    rad = radial_profile(img, centerpoint);

    #Prepares the distance array
    distance = np.indices(np.shape(rad))[0]*1.6095;

    #Average Radius Function
    avgradius = round(np.dot(distance, rad)/np.sum(rad),2)

    #Add calculated value to the growing distance array
    distancearray = np.append(distancearray, avgradius)


print("Done!")

#This part is a simple plot of the data. It's pretty bare bones
# and not too flashy, feel free to modify this part to make matplotlib
# do what you want!

#Plot and Data
distancetime = plt.plot(timearray, distancearray)
plt.title("AM1_1")
plt.xlabel("Time (s)")
plt.ylabel("Average Radius (microns)")

plt.show()

#The derivative calculator does not work well for the first and
# last points so you can ignore this bottom section.
# There are different ways to calculate this in a more accurate way
# so it's safe to ignore this. To get a rough sense, it is easier to
# export the distance array into an Excel sheet using "pandas" and then
# set up a simple formula in Excel.

finaldistance = distancearray
finaltime = timearray
#Derivative FOR loop
derivativearray = np.array(box)
for i in range(0, len(finaldistance)):
    modindex = len(finaldistance)-2
    if i == 0:
        lowerbound = (finaldistance[i]-0)/(finaltime[i+1]-0)
        derivativearray = np.append(derivativearray, lowerbound)
    elif i+1==len(finaldistance):
```

```
        upperbound = finaldistance[modindex+1]-finaldistance[modindex]/(finaltime[modindex+1]-finaltime[modindex])
        derivativearray = np.append(derivativearray, upperbound)
    else:
        derivative = (finaldistance[i+1]-finaldistance[i])/(finaltime[i+1]-finaltime[i])
        derivativearray=np.append(derivativearray, derivative)
```

B.2.2 Single image radial tracking

Below is the python notebook that calculates the radius of a spherulite for a single image. It is useful for understanding how the notebook works for radial tracking of an image stack as shown in Subsection B.2.1.

```
# Average "radius" vs. time function for image stacks.

#This is exactly the same thing as the dynamic code, except I
# removed some components peculiar to working with large file stacks.
# This will be a nicer interface to play with to understand what this
# does for 1 image by itself!

import os
import sys
import glob
import numpy as np
import matplotlib.pyplot as plt

#This is the primary function
def radial_profile(data, center):
    x = np.indices((data.shape))[0]
    y = np.indices((data.shape))[1]
    r = np.sqrt((x - center[0])**2 + (y - center[1])**2)
    r = r.astype(np.int)

    radialprofile = np.bincount(r.ravel(), data.ravel())

    return radialprofile

#USER INPUT: Input values as (y,x)
centerpoint = (1090, 832);

filelist = glob.glob("*.tif");
numimages = len(filelist);

for i in range(0, numimages):

    #Normalize Image so every white pixel is 1 instead of 255.
    img = plt.imread(filelist[i])[...,0]*(1/255)
    rad = radial_profile(img, centerpoint);
```

```
36
37      #Prepares the distance array
38      distance = np.indices(np.shape(rad))[0]*1.6095;
39
40      #Average Radius Function
41      avgradius = round(np.dot(distance, rad)/np.sum(rad),2)
42
43      print(avgradius)
44
45  print("Done!")
46
47  img = plt.imread(filelist[0])
48  plt.imshow(img)
49  plt.show()
```

Appendix C

Microdiffraction comparative measurements summary

This appendix provides an overview of the diffraction patterns and relevant energy peaks found for each of the platelet and spherulite samples of 4CzIPN, rubrene, and BDP described in Section 2.6.1. The XMAS software is valuable for dynamic viewing of diffraction patterns and some preliminary analysis (e.g., peak indexing, linecuts). Instructions to download and use the software can be found on the ALS 12.3.2 beamline website, and some snapshots of the program are shown in Figure C.1.

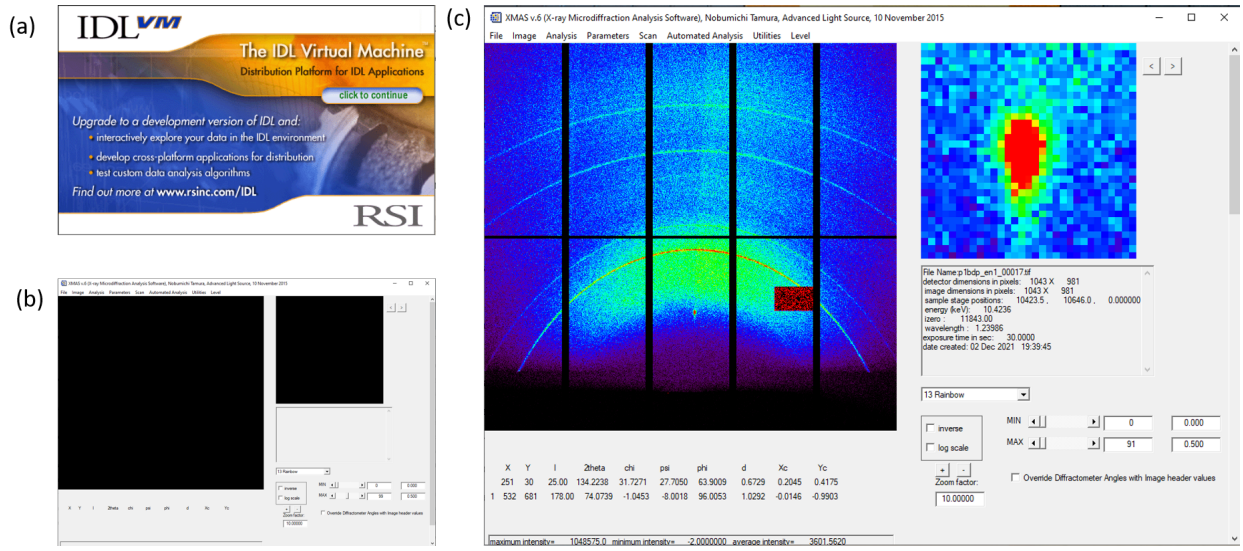

Figure C.1: XMAS software overview for microdiffraction analysis. (a) Opening window for XMAS program platform. (b) Viewing window before opening an image file. (c) Once proper calibration parameters have been selected, one can open an image file and see the diffraction pattern in the program and zoom in on peaks.

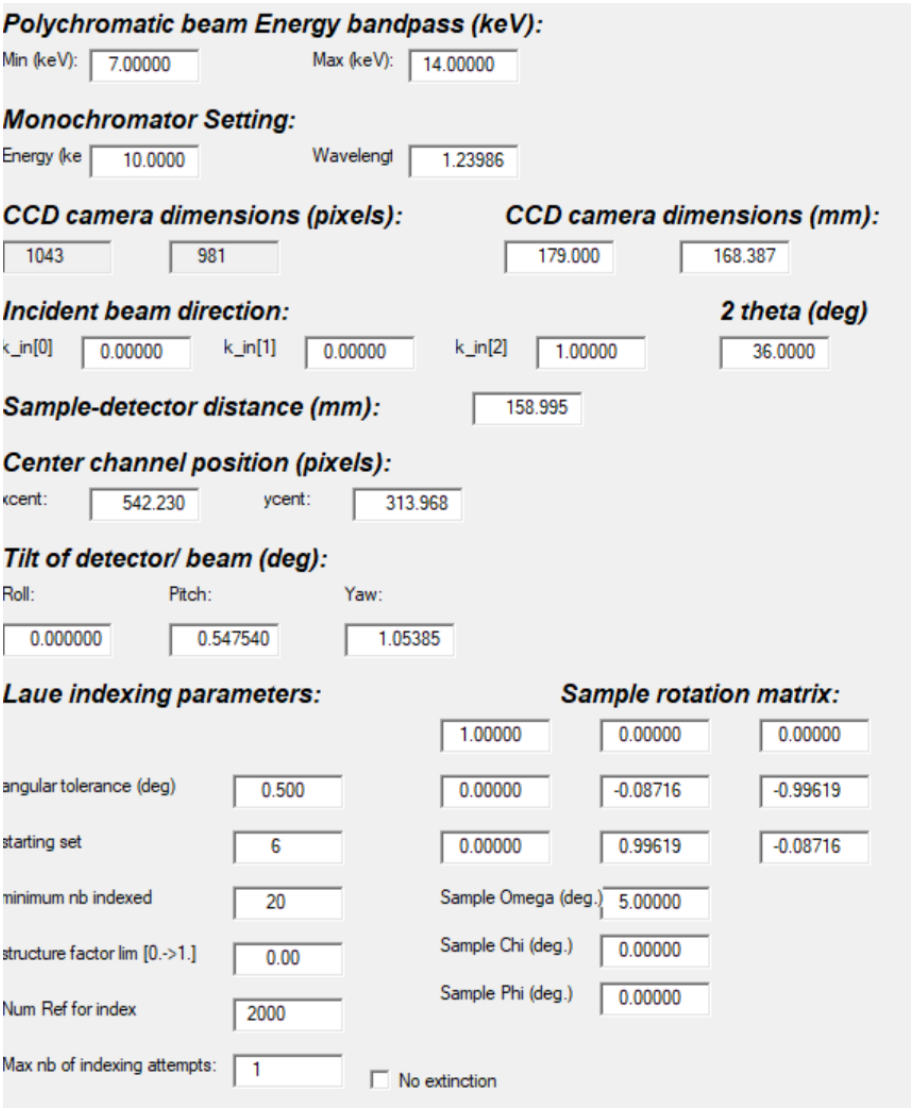

Figure C.2: Calibration parameters for microdiffraction experiment. The incidence angle is identified as 'sample omega' under the sample rotation matrix section. The label 2 theta (deg) refers to the 2θ of the detector.

We scanned through energies ranging from 7 - 14 keV. The incidence angle was 5°, and the beam probe dimensions were $\sim 5 \times 25$ μm. The calibration parameters to properly analyze images are shown in Figure C.2, and specific details such as exposure times for a given scan were logged. Most scans were measured with 30 s or 45 s exposure times.

When peaks were identified in the energy scans, we found the maximum intensity ($I_{\max}$) of the peaks through either manual Gaussian fitting, XMAS fitting, or the XMAS peak finding routine. Since the films were very thin, some peaks appeared over multiple energies (e.g., broad in energy) and had slight shifts. When peaks were not symmetrical or had smearing,

we suspect these effects could be attributed to a slight misorientation in the out-of-plane crystal axis.

To accomplish peak indexing with XMAS, Nobumichi Tamura (beamline scientist) mentioned that XMAS was typically used to index Laue patterns. We conducted monochromatic diffraction patterns to minimize sample damage, so we created a pseudo-Laue pattern by summing all the energy scan patterns in XMAS. Indexing requires a minimum of three reflections, and multiple reflections, generally, are needed to calculate properties like strain. XMAS can calculate strain under its method, strain refinement, if at least six indexed reflections are available. Since we did not have that many reflections successfully indexed with sufficient strength or consistency across samples and regions of interest (ROIs), it was recommended that we use a manual approach to calculate strain. The manual approach calculates the differences in d-spacings between the observed reflections, which can be calculated from the energy and position of the reflections at peak intensity and the calculated values of a known diffraction pattern with zero strain. This is a possible course of work for the future.

C.1 4CzIPN platelet diffraction patterns

A polarized optical image of the 4CzIPN platelet film sample is shown in Figure C.3a, where locations that were probed with the microdiffraction beam are identified by the ROI labels. Two platelets were studied; a first that contains ROI2 and ROI3, and a second platelet containing ROI4. An energy scan for a platelet control not shown in the figure yielded up to 7 peaks in the diffraction pattern, which are listed in the table in Figure C.3. Figure C.3c-e show examples of diffraction patterns from the platelet sample. The main observation was that we did not consistently see all 7 peaks in different platelets, even after scanning the z-position of the sample stage to ensure we did not miss any peaks. 4CzIPN has a triclinic structure.

We did not observe any diffraction peaks in 4CzIPN spherulite films, possibly due to the increased polycrystallinity, and we show the polarized optical image for qualitative comparison (Figure C.4).

C.2 Rubrene platelet and spherulite diffraction patterns

The polarized optical image for the rubrene platelet thin film sample is shown in Figure C.5(a), where we probed three platelet domains. The full table of peaks observed at various energies is shown in Figure C.5, where the 311L and 311R peaks appeared to correspond to the same 311 position but appeared on opposite sides of the 2D diffraction pattern at times. Unlike the 4CzIPN platelet sample, we observed all four peaks consistently in the different rubrene platelet domains. The main change observed was in the strength of peak intensities across the domains, where the 311 peak tended to be the weakest.

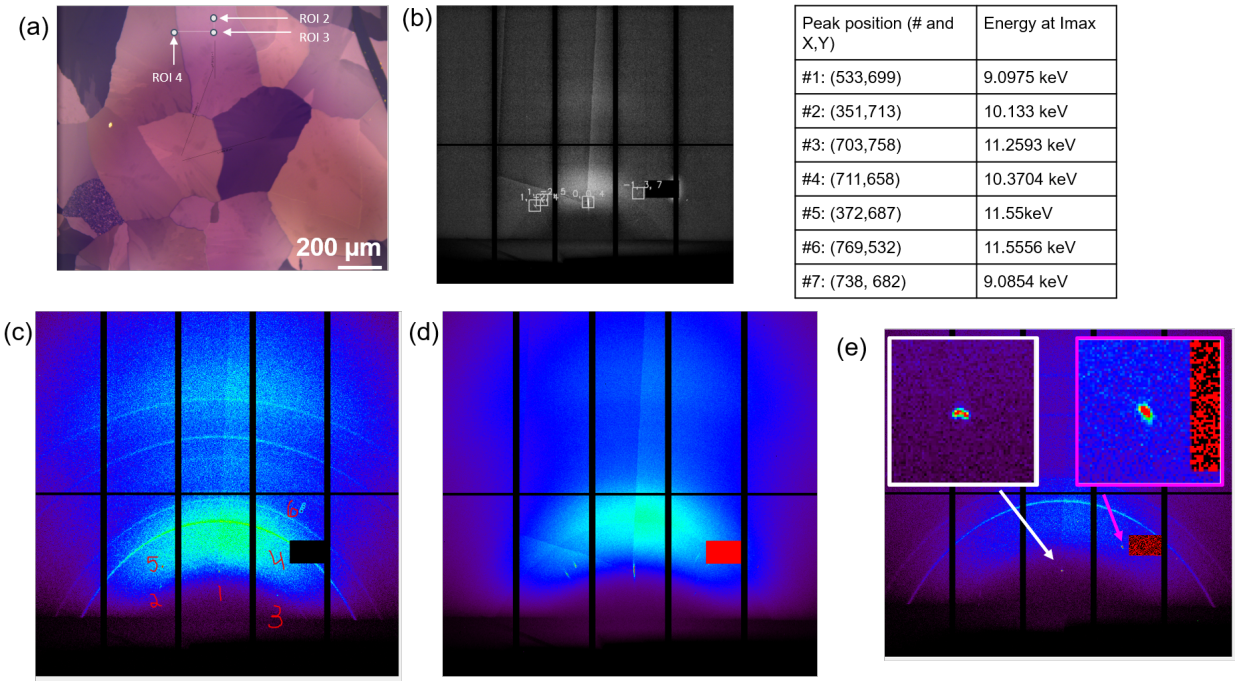

Peak position (# and X,Y)	Energy at Imax
#1: (533,699)	9.0975 keV
#2: (351,713)	10.133 keV
#3: (703,758)	11.2593 keV
#4: (711,658)	10.3704 keV
#5: (372,687)	11.55keV
#6: (769,532)	11.5556 keV
#7: (738, 682)	9.0854 keV

Figure C.3: Platelet diffraction patterns for the 4CzIPN sample. (a) Polarized optical image of sampling region with regions of sampling (ROIs) identified. (b) Example of XMAS software indexing peaks. (c) and (d) 2D-diffraction patterns of 4CzIPN platelet with peaks identified in (c) and energy scan lapse to enhance peak signal shown in (d). (e) Examples of close-ups of peaks. A table of all peaks observed and their corresponding energies is also included.

The polarized optical image for the rubrene spherulite thin film sample is shown in Figure C.6(a), where we probed a total of 14 regions as shown by the white rectangles. We probed close to the nucleus and at varying radii away from the nucleus within a single spherulite structure. For all of the sampling regions, we only observed the (006) and (512) peaks (Figure C.6b). For the 5 regions further away from the nucleus (i.e., not part of the 3×3 sampling grid), the (512) peak was much weaker and was not always observed. This may suggest that molecular ordering close to the nucleus is different than at larger radii and may warrant further investigation to determine if this corresponds to the hybrid crystalline microstructure observed with STXM and 4D-STEM.

In a previous group microdiffraction beamtime conducted by Brendan Folie and Alex Liebman-Peláez, they used a beam probe size of 5×3 μm with a monochromatic energy of 6 keV at an angle of 5°. For their rubrene spherulite and platelet samples, they only observed the (002) peak. We tried repeating their measurements with the same experimental parameters but did not see the (002) peak. Conducting energy scans helped to identify diffraction peaks in our samples, but we do not know why we did not see diffraction patterns comparable to the previous experiment. The benefit of having more diffraction peaks, however, may help with quantitative analysis such as strain.

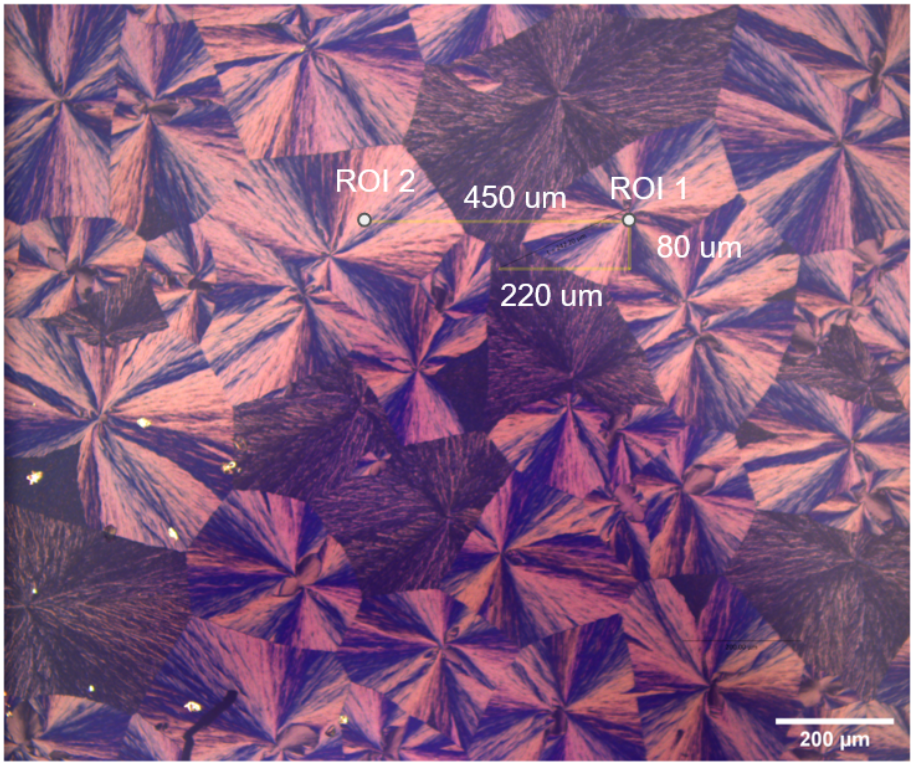

Figure C.4: Polarized optical image for 4CzIPN spherulite sample. ROIs probed by the microdiffraction beam are indicated, and the values of 220 μm, 80 μm, and 450 μm are references for moving the sample stage to the ROI1 and ROI2 positions.

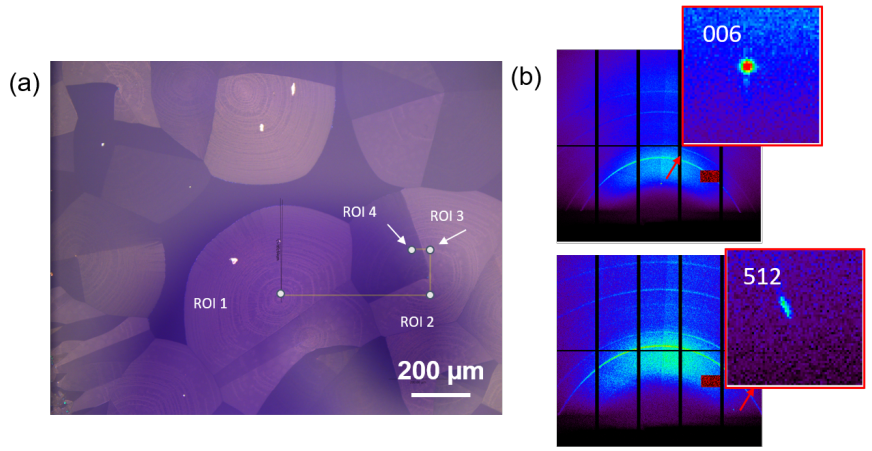

Peaks	Energies
006(peak 1)	11.2 keV
512 (peak 2)	9.136 keV
311? L	8.1 kEv
311 R	8.37 keV

Figure C.5: Platelet diffraction patterns for rubrene sample. (a) Polarized optical image of sampling region with regions of sampling (ROIs) identified. (b) Examples of close-ups of peaks in 2D-diffraction patterns. A table of all peaks observed and their corresponding energies is also included.

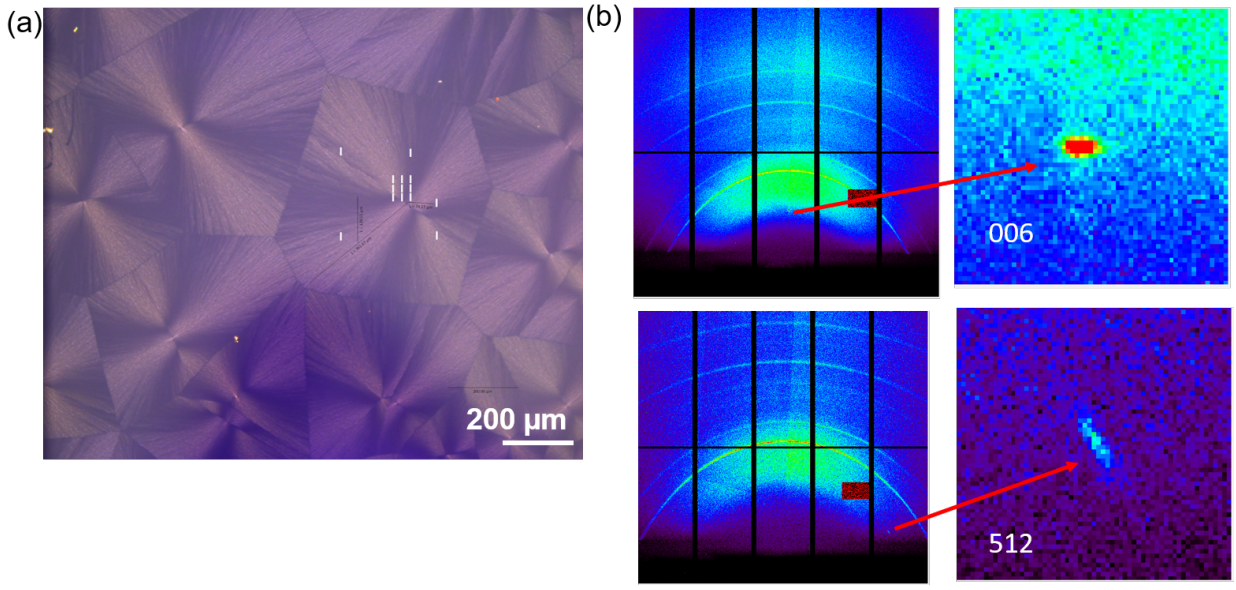

Figure C.6: Spherulite diffraction patterns for rubrene sample. (a) Polarized optical image of sampling region with regions of sampling identified by white rectangles representing the probe size dimensions. (b) Close-up of peaks observed in the different sampling regions in 2D-diffraction patterns.

C.3 BDP platelet and spherulite diffraction patterns

Two different platelets were probed in BDP platelet thin films (Figure C.7), where ROI2 is close to the grain boundary between two platelets. We observed seven reflections in ROI1, which are listed in the table in Figure C.7. When we moved to ROI2, however, we only observed up to two reflections (#1 and #7) in the diffraction patterns when we monochromatically scanned at each of the seven different energies Figure C.8. It is possible that probing close to a grain boundary decreases the ordering in the region so that there is less clear diffraction.

We measured different areas across two spherulites as indicated by the white rectangles; although one of the spherulites appears to have platelet domains as indicated by the sharp intensity contrast (Figure C.9). For all of the ROIs measured across the seven different monochromatic energies, only the #7 peak was observed (Figures C.9-C.10). Due to the increased disorder of the spherulite relative to the platelet, it was not surprising that we observed fewer reflections. With more quantitative analysis between the peaks across different regions, we may learn about whether there are spatial variations in the diffraction pattern and consequently molecular packing.

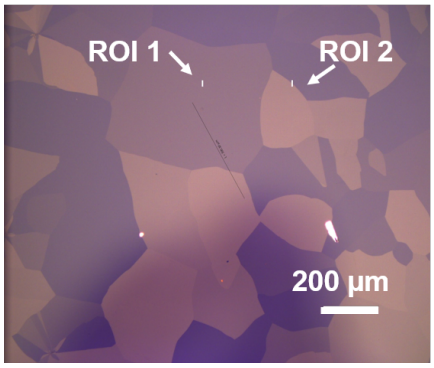

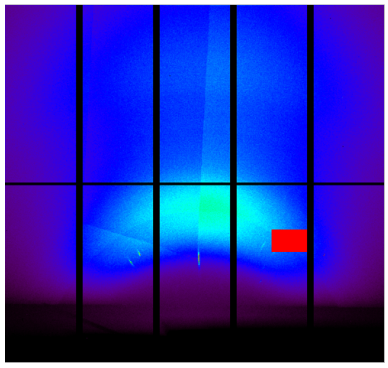

Peak position (# and X,Y)	Energy at Imax
#1: (829,788)	8.45446 keV
#2: (874,759)	8.60595 keV
#3: (900,728)	8.60595 keV
#4 (318,773)	9.21182 keV
#5: (341,630)	9.66622 keV
#6: (663,610)	11.0295 keV
#7: (529, 705)	11.4761 keV

Figure C.7: Platelet diffraction patterns for BDP sample. Polarized optical image of sampling regions accompanied by 2D diffraction pattern of peaks integrated over energy scan, and table of identified diffraction peaks.

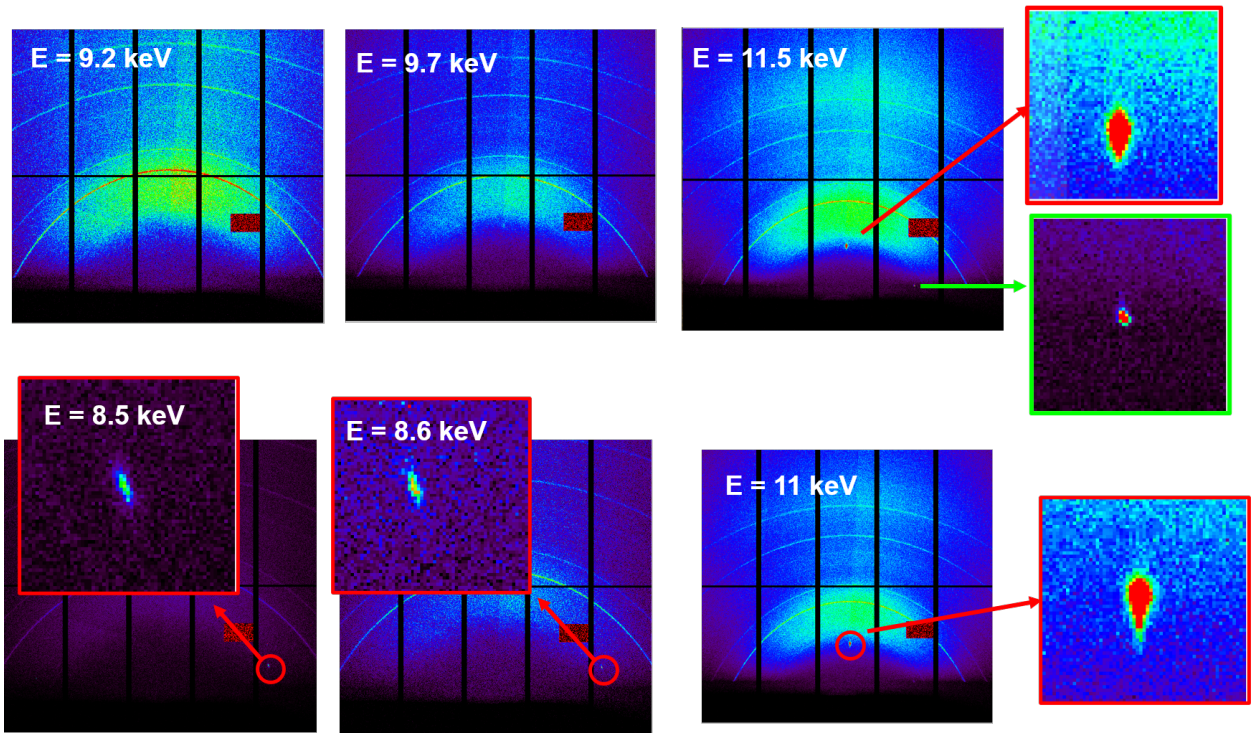

Figure C.8: Platelet diffraction patterns for BDP sample ROI 2. Diffraction patterns at the energies associated with the seven peaks identified from ROI1. Here at ROI2, we only observe one to two reflections.

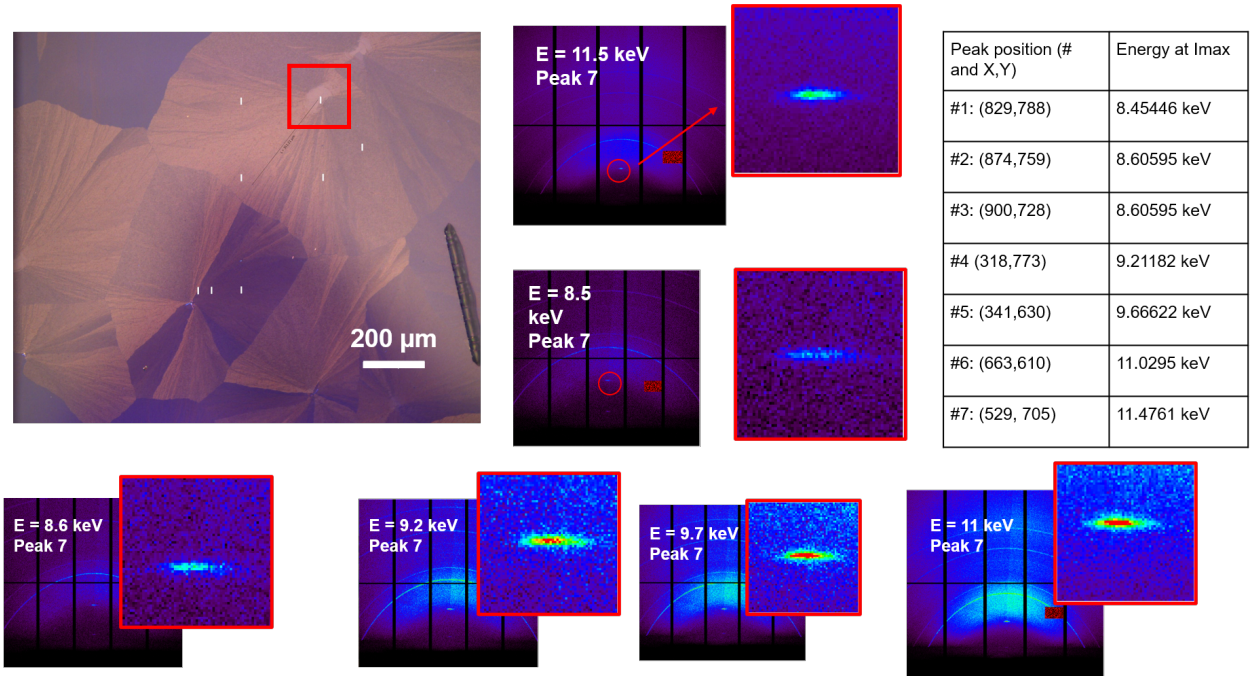

Peak position (# and X,Y)	Energy at Imax
#1: (829,788)	8.45446 keV
#2: (874,759)	8.60595 keV
#3: (900,728)	8.60595 keV
#4 (318,773)	9.21182 keV
#5: (341,630)	9.66622 keV
#6: (663,610)	11.0295 keV
#7: (529, 705)	11.4761 keV

Figure C.9: Spherulite diffraction patterns for BDP sample ROI1. Polarized optical image of BDP spherulite sample where white rectangles represent regions that were probed. For all regions, only one reflection (#7) was observed across the seven different monochromatic energies. The diffraction patterns for the different energies are shown with close-ups of peak #7.

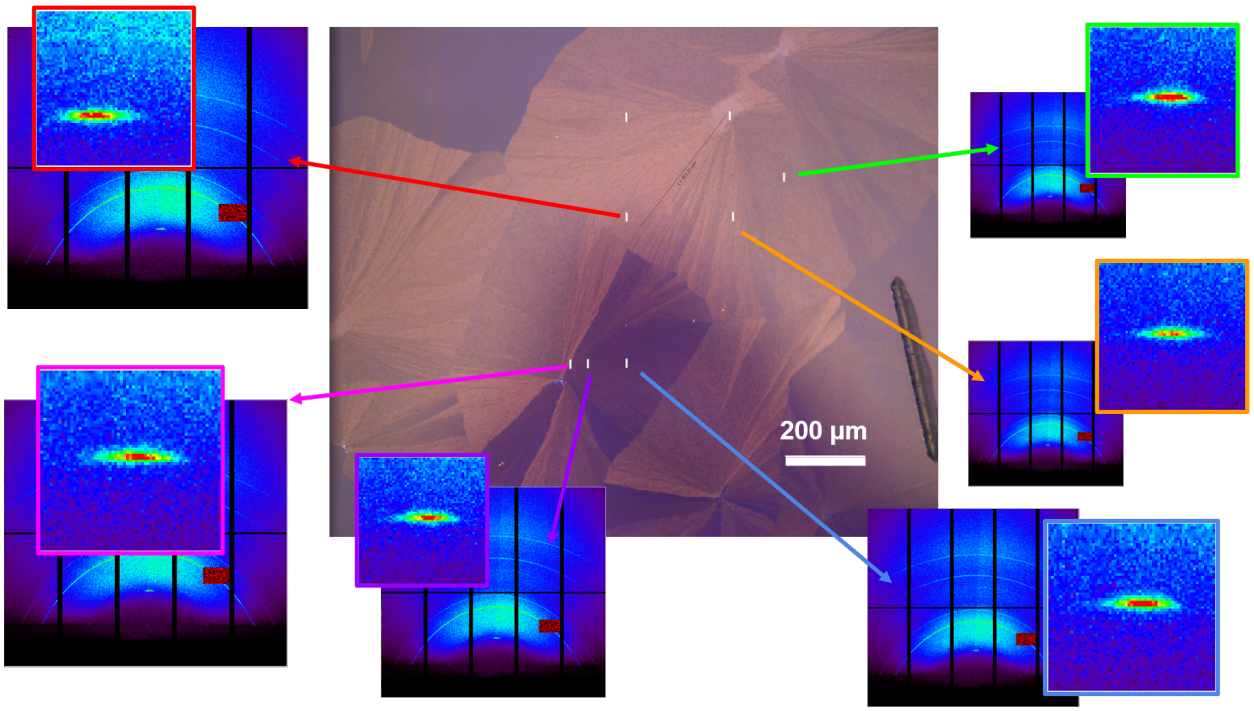

Figure C.10: Spherulite diffraction patterns for remaining ROIs in BDP sample. Polarized optical image of BDP spherulite sample with the remaining six ROIs highlighted with corresponding close-ups of diffraction peak #7.